Experimental Study on the Carbon Conversion Efficiency and Emission Indices of a Lab-Scale Air-Assisted Flare

by

Hamza Ahsan

A thesis submitted in partial fulfillment of the requirements for the degree of

Master of Science

Department of Mechanical Engineering
University of Alberta

Abstract

A lab-scale coflow burner was used to investigate the effect of air assist on the carbon conversion efficiency (CCE) and emission indices (EIs) of industrial flare operations in the upstream and downstream energy sectors of the oil and gas industry. A 25.4 mm diameter burner was constructed of two concentric tubes to facilitate parallel flows of fuel gas and air assist. The standard experiment consisted of an outer coflow of methane at 20 standard liters per minute and air injected through a 12.7 mm diameter inner tube. Additional experiments were performed to explore changes in the inner tube size, fuel type and flow rate, and assist configuration and composition. The combustion products were captured and analyzed using a gas chromatograph to measure the concentrations of CH_4, C_2H_6, C_3H_8, CO, and CO_2. A photoacoustic extinctiometer and a NO_x analyzer were used to measure black carbon and NO_x concentrations, respectively. For each experiment, the flow rate of air was incrementally increased from no flow until the CCE dropped to less than 10%. It was generally observed that at no or low air flow rate the CCE was > 99%, while the black carbon and NO_x EIs were at a maximum. As the flow rate of air was increased the CCE remained the same, but the black carbon and NO_x EIs could drop by two orders of magnitude. Further increasing in the flow of air triggered a sudden and catastrophic collapse in CCE. A simultaneous drop in CO_2 emissions and a rise in unburned hydrocarbons were observed as a result of fuel stripping. CO was also detected during the collapse in CCE due to an excessively turbulent air stream inhibiting complete combustion. From an industrial flare operating standpoint, however, there was a range of air flow rates that resulted in high CCE and low pollutant EIs.

Preface

The present study involved the development of a lab-scale flare facility and procurement of diagnostic instruments, which was accomplished in collaboration with Abbas Ahsan. Parts of Chapter 2 of this thesis have been published as

A. Ahsan, H. Ahsan, J.S. Olfert, L.W. Kostiuk, Quantifying the carbon conversion efficiency and emission indices of a lab-scale natural gas flare with internal coflows of air or steam, Experimental Thermal and Fluid Science. 103 (2019) 133–142. doi:10.1016/j.expthermflusci.2019.01.013.

For this publication, I shared equal responsibility with Abbas Ahsan in conducting the experiments, data collection and processing, analysis, and composing the manuscript. Dr. Larry Kostiuk and Dr. Jason Olfert provided manuscript edits.

Acknowledgments

I would like to express my sincere gratitude to Dr. Larry Kostiuk for providing me with the opportunity to engage in the flare research project. This was a topic that I had no prior exposure to and Larry did a wonderful job motivating me to learn more about it. His passion for research and dedication to his students is inspiring. Our discussions have always been insightful and helped in overcoming many challenges over the course of the project. Although, I often wondered whether he could really tell us apart. I would also like to thank Dr. Jason Olfert for facilitating this research project by offering his lab space and expertise. His enthusiasm and technical advice were invaluable, and his jokes were sometimes funny.

I must also acknowledge my collaboration with the FlareNet community. It was truly a pleasure getting to know and work with some of you. Thank you for letting me be part of such a great team. I hope the best for all of you as you move forward.

Finally, I would like to thank my family, especially my parents. It wouldn't have been possible without their continued support and encouragement throughout my graduate studies. This acknowledgement wouldn't be complete without mentioning my brother Abbas. We had a good time and even got some work done.

Table of Contents

1. Introduction 1

1.1 Flaring and its Environmental Implications 1

1.2 Air-Assisted Flares 5

1.3 Pilot and Industrial Air-Assisted Flare Studies 10

1.4 Research Objectives 19

2. Experimental Setup 20

2.1 Burner Design 20

2.2 Lab-Scale Flare Facility 22

2.3 Methodology for Measuring Carbon Conversion Efficiency and Emission Indices of a Lab-Scale Air-Assisted Flare 29

3. Results and Discussion 34

3.1 Test Matrix 34

3.2 Characterization of Steady State Burner and Exit Conditions 35

3.3 Experimental Set 1: Combustion of 20 SLPM CH_4 Annular Flow with 100% Air Coflow through 12.7 mm OD Inner Tube 40

3.4 Experimental Set 2: Combustion of 40 SLPM CH_4 Annular Flow with 100% Air Coflow through 12.7 mm OD Inner Tube 44

3.5 Experimental Set 3: Combustion of 20 SLPM CH_4 Annular Flow with 100% Air Coflow through 6.35 mm OD Inner Tube 46

3.6 Experimental Set 4: Combustion of 20 SLPM CH_4 Annular Flow with 92% N_2/8% Ar Coflow through 12.7 mm OD Inner Tube 48

3.7 Experimental Set 5: Combustion of 20 SLPM CH_4 Annual Flow with 85% N_2/10.5% O_2/4.5% Ar Coflow through 12.7 mm OD Inner Tube 50

3.8 Experimental Set 6: Combustion of 20 SLPM CH_4 Annular Flow with 55% N_2/42% O_2/3% He Coflow through 12.7 mm OD Inner Tube 52

3.9 Experimental Set 7: Combustion of 20 SLPM C_3H_8 Annular Flow with 100% Air Coflow through 12.7 mm OD Inner Tube 57

3.10 Experimental Set 8: Combustion of 20 SLPM CH_4 Inner Flow through 12.7 mm OD Tube with 100% Air Annular Coflow 59

3.11 Analysis of Results with Respect to Exit Hydrodynamics 62

3.12 Comparison with Industrial-Scale Flare Studies 64

4. Conclusions and Recommendations 68

4.1 Conclusions 68

4.2 Recommendations 72

Bibliography 73

Appendix A Uncertainty Analysis Methodology 77

Appendix B Mass Flow Controller Calibration 79

Appendix C Gas Chromatograph Calibration Standards and Uncertainties 81

Appendix D Uncertainty Analysis of CCE and EI 83

Appendix E Adiabatic Flame Temperature 87

List of Tables

Table 1.1: Maximum emission indices of THC, CO_2, CO, and NO_x for a pilot-scale air-assisted flare operating at a combustion efficiency ≥ 96.5% based on a study by McDaniel [29]. 12

Table 3.1: Test matrix of experimental sets performed on a lab-scale air-assisted flare. 34

Table 3.2: Temperature range of fuel and assist streams assessed at various axial (*i.e.*, *z*-axis) positions along the burner. 35

Table 3.3: Exit condition parameters for the corresponding air-to-fuel gas MFR defined for each experimental set. Calculated parameters for the no assist case were not included in the table. 39

Table 3.4: 100 year GWP of various pollutant emissions and associated uncertainties according to the IPCC. 42

Table 3.5: Maximum EIs of various pollutant emissions generated by a lab-scale air-assisted flare evaluated at a CCE ≥ 96.5%. The air-to-fuel gas MFRs were interpolated at a CCE = 96.5%. 65

Table C.1: GC calibration standards. 81

Table C.2: Uncertainties associated with each carbon based species. 82

List of Figures

Figure 1.1: The top 30 flaring countries by volume in 2017 [2]..... 2
Figure 1.2: (a) A schematic of a typical industrial air-assisted flare, and (b) a photo of an air-assisted flare reproduced from Smith and Seefeldt [24] with permission from Zeeco, Inc..... 7
Figure 1.3: Common designs for air-assisted flare tips are (a) the drilled spider, (b) triangular slots, and (c) internal tube bundle. The photos are reproduced from Smith and Seefeldt [24] with permission from Zeeco, Inc..... 8
Figure 1.4: External air ring flare tip design reproduced from Smith and Seefeldt [24] with permission from Zeeco, Inc. 9
Figure 1.5: Combustion efficiency of an air-assisted flare burning 44% C_3H_8 diluted in N_2 with an overall LHV of 38.9 MJ/m^3, based on a study by Pohl and Soelberg [32]..... 13
Figure 1.6: Combustion efficiency of an air-assisted flare burning gas mixtures consisting of natural gas, C_3H_6 or C_3H_8, and N_2 based on a study by Allen and Torres [36]..... 16
Figure 1.7: Emission indices for (a) THC and (b) NO_x from an air-assisted flare burning gas mixtures consisting of natural gas, C_3H_6 or C_3H_8, and N_2 based on a study by Allen and Torres [36,37]..... 18
Figure 2.1: An overall and cross-sectional view of the burner is depicted. Air enters the bottom port of the tee and travels the entire length of the inner tube before exiting from the burner tip. Coflowing fuel enters the side port and travels through the annular space between the inner and outer tubes before exiting from the burner tip. 21
Figure 2.2: Thermocouple arrangement for measuring the inner flow temperature at the inner tube exit and outer coflow temperature at various positions along the annular gap..... 22
Figure 2.3: Flare facility equipped with a lab-scale air-assisted flare (burner), an array of compressed gas cylinders and gas metering equipment, a sampling system, and diagnostic equipment. 23

Figure 2.4: A gas mixture consisting of 92% N_2 and 8% Ar by volume to simulate air are mixed at a 3-way tee before entering the inner tube of the burner. 25
Figure 2.5: A control volume encloses the burner and exhaust hood and the relevant carbon streams are identified. Mole fractions of carbon-containing species are represented as X_k. 30
Figure 3.1: Temperature measurements within the annular flow stream from $z = -40$ mm to $z = 0$ mm with respect to the burner exit plane at increasing air-to-fuel gas MFRs for experimental sets (a) 1 and (b) 8. Each plot also has an inset figure showing the temperature of the internal coflow at the burner exit. 37
Figure 3.2: Adiabatic flame temperature trends for each experimental set based on STANJAN calculations. 40
Figure 3.3: Results of experimental set 1 - CCE (bottom), EI (top). 43
Figure 3.4: Photos of the flame taken during experimental set 1 at increasing air-to-fuel gas MFRs. 44
Figure 3.5: Results of experimental set 2 - CCE (bottom), EI (top). 46
Figure 3.6: Results of experimental set 3 - CCE (bottom), EI (top). 48
Figure 3.7: Results of experimental set 4 - CCE (bottom), EI (top). 50
Figure 3.8: Results of experimental set 5 - CCE (bottom), EI (top). 52
Figure 3.9: Results of experimental set 6 - CCE (bottom), EI (center), $EI_{CO2,eq}$ (top). 55
Figure 3.10: Photos of the flame taken during experimental set 6 at increasing equivalent air-to-fuel gas MFRs. 56
Figure 3.11: O_2 content in the assist stream for experimental sets 1, 4, 5, and 6 plotted as a function of the equivalent air-to-fuel gas MFR marking the onset of CCE collapse. The MFRs were interpolated at a CCE = 96.5%. 56
Figure 3.12: Results of experimental set 7 - CCE (bottom), EI (top). 58
Figure 3.13: Photos of the flame taken during experimental set 7 at increasing air-to-fuel gas MFRs. 59
Figure 3.14: Results of experimental set 8 - CCE (bottom), EI (top). 61
Figure 3.15: Photos of the flame taken during experimental set 8 at increasing air-to-fuel gas MFRs. 62

Figure 3.16: CCE plotted as a function of the air-to-fuel gas MFR. 63
Figure 3.17: CCE plotted as a function of the air-to-fuel gas VR. 63
Figure 3.18: CCE plotted as a function of the air-to-fuel gas MR. 64
Figure B.1: MFC calibration setup. 79
Figure B.2: 50 SLPM MFC calibration curve for methane. 80
Figure C.1: GC calibration curve for CH_4. 82
Figure E.1: Combustion system for analyzing adiabatic flame temperature. 87

List of Abbreviations

API	American Petroleum Institute
BC	Black Carbon
CCE	Carbon Conversion Efficiency
EI	Emission Index
EPA	Environmental Protection Agency
GHG	Greenhouse Gas
GWP	Global Warming Potential
ID	Inner Diameter
IPCC	Intergovernmental Panel on Climate Change
LHV	Lower Heating Value
MFR	Mass Flow Ratio
OD	Outer Diameter
RF	Radiative Forcing
RTD	Resistance Temperature Detector
TCEQ	Texas Commission on Environmental Quality
THC	Total Unburned Hydrocarbons
VFD	Variable Frequency Drive

Chapter 1

1. Introduction

1.1 Flaring and its Environmental Implications

The upstream and downstream energy sectors dispose of waste hydrocarbon gases through a practice known as flaring. The goal of flaring is to reduce the net environmental and health impacts of releasing flammable gases into the atmosphere by first combusting them at the tip of a flare stack. In 2015, satellite data identified a total of 13 605 flaring sites worldwide [1]. Of these, 12 227 were located in upstream sites based on oil and gas exploration and production facilities, accounting for 90.6% of total flaring worldwide; 861 in downstream sites, namely refineries and gas processing facilities where 8.4% of flaring occurred; and 517 in industrial sites such as coal mines and landfills, which constituted the remaining 1% of flared volumes [1]. A global survey of total flared gas volumes from 2013 to 2017 revealed approximately 140 billion cubic meters of natural gas flared annually, amounting to nearly 300 Mt of carbon dioxide (CO_2) released into the atmosphere [2]. Figure 1.1 shows the top 30 countries ranked in terms of flared volumes in 2017. CO_2 is a dominant greenhouse gas (GHG) and its global concentration has increased as of 2017, reaching a new record high according to the American Meteorological Society [3]. The global average CO_2 concentration measured at Earth's surface was 405.0 ± 0.1 ppm in 2017 which is 2.2 ppm greater than the amount recorded in 2016 [3]. The presence of a GHG in the atmosphere gives rise to the so-called greenhouse effect by trapping infrared radiation, thereby contributing to global warming [4]. As a result, global surface temperatures have risen steadily over the years. The surface temperature referred to here is a

combination of the air temperature taken about 1.5 m above the ground and the temperature of water measured anywhere from 1 m to 15 m below the ocean surface [5]. In 2017, temperatures were 0.38 °C to 0.48 °C above the average taken from 1981 to 2010, which brings it to the second or third warmest annual global temperature ever recorded since the 1800s [3].

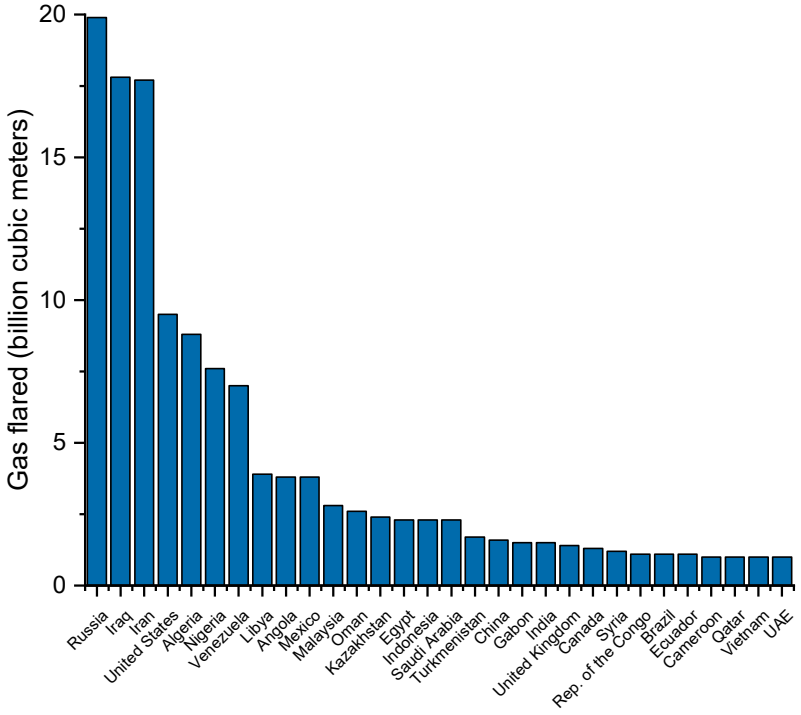

Figure 1.1: The top 30 flaring countries by volume in 2017 [2].

Converting the fuel in the flare gas to CO_2 is considered more desirable compared to the alternative practice of venting directly to the atmosphere due to the implications of GHG emissions, particularly in the form of methane (CH_4). According to the Fifth Assessment Report of the Intergovernmental Panel on Climate Change (IPCC), CH_4 has a Global Warming Potential (GWP) of 28 relative to CO_2 on a mass basis over a time period of 100 years [6]. The significance of this statistic can be appreciated by the fact that the oil and gas industry is the largest source of CH_4 emissions in Alberta [7]. In 2014, CH_4 emissions from Alberta's oil and gas sector amounted to 31.4 Mt of CO_2 equivalent emissions. Of these emissions, 48% came from direct venting, 46% from fugitive emissions or leaks, and 6% from flaring or

other sources [7]. Therefore, from an emissions standpoint flaring is a mitigating measure towards minimizing the impact of GHG emissions on the environment.

A characteristic of flare performance commonly evaluated by flare operators is combustion efficiency (also referred to as carbon conversion efficiency). The combustion efficiency of a flare quantifies the extent to which the carbon in the fuel of the flare gas is fully oxidized to CO_2. Flare operators aim to achieve a combustion efficiency of 100% since anything less than this indicates the releasing of unburned components of the flare gas or partially oxidized products into the atmosphere, which are considered pollutant emissions. A particularly harmful product of incomplete combustion from flaring is particulate matter in the form of soot. Soot is formed when hot particles of carbon that give a flame its characteristic luminosity are cooled to a non-reactive state without fully oxidizing, resulting in the appearance of smoke [8]. A subset of soot, black carbon (BC) is a light-absorbing carbonaceous aerosol and plays an important role in climate change [9]. The effect that a substance has on climate change can be characterized by its radiative forcing (RF), which the IPCC defines as the net change in the energy balance of the Earth-atmosphere system due to some imposed perturbation. RF is expressed in W/m^2 evaluated at the tropopause which is the upper bound of the troposphere, the lowest layer of Earth's atmosphere [6]. A positive RF corresponds to an increase in the energy of the Earth-atmosphere system, ultimately leading to a warming effect, whereas a negative RF denotes a decrease in energy and leads to a cooling effect on the climate. A recent study estimates the RF of atmospheric BC based on changes over the industrial-era (1750 to 2005) to be +1.1 W/m^2 with 90% uncertainty bounds of +0.17 W/m^2 to +2.1 W/m^2 [10]. This suggests that BC has the second largest influence as an anthropogenic emission on climate forcing, the largest being CO_2 with an RF of $+1.82 \pm 0.19$ W/m^2 [6]. It is also of interest that CH_4 ranks third with an RF of $+0.48 \pm 0.05$ W/m^2 [6]. Further evidence of the negative environmental repercussions of BC emissions from gas flaring is the occurrence of Arctic warming. Stohl *et al*. suggest that flaring is a dominant source of BC emissions in the Arctic and is responsible for 42% of the annual mean BC surface concentrations [11]. It was estimated that flaring accounts for 52% of all Arctic BC near the surface during the month of March [11]. Sand *et al*.

studied the Arctic climate response to the presence of BC and showed that BC exerts a positive forcing [12]. Since BC absorbs solar radiation, when deposited on snow it compromises its albedo, or ability to reflect sunlight, thus resulting in accelerated melting. The impact of BC in the Arctic during spring was found to be significantly higher due to the abundance of sunlight and when most of the surfaces are covered with snow and sea ice [12].

Other harmful emissions from flaring may include nitrogen oxides (NO_x), sulfur dioxide (SO_2), and by-products of incomplete combustion, such as polycyclic aromatic hydrocarbons (PAHs), volatile organic compounds (VOCs), carbon monoxide (CO), and unburned hydrocarbons, primarily CH_4. Increased emissions of CO, CH_4, VOCs, and NO_x since pre-industrial times and over the past several decades have been attributed to an increase in ozone (O_3) in the troposphere (*i.e.*, the lowest layer of Earth's atmosphere) [6]. This comes as no surprise since the rate of VOC emissions from the oil and gas sector in the period of 2002 to 2011 has increased by 400% and NO_x emissions have increased by 94% [13]. Tropospheric O_3 is a by-product of photochemical oxidation of CO, CH_4, and non-methane VOCs in the presence of NO_x (NO + NO_2) [14]. The contribution of tropospheric O_3 to climate change is significant. An RF value for O_3 for the period of 1750 to 2010 was calculated to be +0.41 W/m^2 with an uncertainty of ±17% based on a single standard deviation [14]. PAHs are common environmental contaminants and are associated with adverse health effects. A study by Strosher from the Alberta Research Council investigated flare emissions at an oilfield battery site in Alberta and identified a number of PAHs in samples taken from a sweet (low sulphur) gas flare [15]. For example, benzo[a]pyrene in the amount of 2.2 mg/m^3 and indeno[1,2,3-cd]pyrene in the amount of 0.6 mg/m^3 were measured from the plume of the flare [15]. Both of these compounds are labeled as probable human carcinogens by the US Environmental Protection Agency's (EPA) Integrated Risk Information System [16]. SO_2 emissions arise when hydrogen sulfide (H_2S) is present in the flare gas and can have substantial impacts on human health and the environment [17]. The Workplace Hazardous Materials Information System (WHMIS) classifies SO_2 as toxic and corrosive. Exposure to SO_2 is harmful to the human respiratory system and can cause long-term

conditions such as asthma [18]. When released into the atmosphere, SO_2 forms sulfuric acid (H_2SO_4) and contributes to acid rain. Ecosystems that are sensitive to acidification can suffer localized extinction of wildlife and diminished plant growth [18].

1.2 Air-Assisted Flares

Flares are meant to be safe and reliable devices for the disposal of flammable gases in the course of routine oil and gas production and processing operations so as not to pose a threat to surrounding areas. However, flares are often viewed as a nuisance by neighboring communities since they are typically accompanied by a combination of smoke, thermal radiation, visible light, noise, and pollutant emissions as detailed in the previous section [19]. To protect the environment and well-being of the general public from the undesirable by-products of flaring, certain regulations have been put in place by government bodies to hold flare operators accountable for violations. A prominent regulatory body is the US Environmental Protection Agency which states in Title 40 of the Code of Federal Regulations (40 CFR) §60.18, that flares shall be designed for and operated with no visible emissions (*i.e.*, soot), except for periods not to exceed a total of 5 minutes during any 2 consecutive hours [20]. In addition, flares shall be operated with a flame present at all times [20]. Thus, non-sooting, or smokeless, operation is the primary design feature that flare manufacturers aim to achieve.

Guidelines pertaining to the design, operation and maintenance of flares have been developed by the American Petroleum Institute (API) in the form of technical standards. API standard 521 and 537 provide recommendations for the proper utilization of flares based on government regulations and established industry practices. Various techniques have been proposed by the API to facilitate smokeless flaring, most of which are based on the notion that smoke is a consequence of fuel-rich combustion (*i.e.*, a condition where there is insufficient oxygen for complete combustion) [21]. From an emissions standpoint, it may seem reasonable to introduce an oxidant into the flare gas stream prior to combustion in order to achieve a premixed (or partially premixed) flame, which tend to burn hotter and generate less soot than

diffusion flames. However, this is generally avoided as it may lead to the risk of flashback, a condition where the flame propagates below the flare tip potentially leading to thermal degradation of the flare stack [21]. Therefore, flares operate with a diffusion flame and the reaction is driven towards completion by means of injecting either steam or air into the flare gas stream as it exits the flare tip, thereby generating turbulence and entraining air into the combustion zone [21]. Flares that utilize steam or air are termed either steam-assisted or air-assisted flares. These assisting fluids have been observed to have the benefit of improving the combustion efficiency of flares, reducing soot emissions, as well as reducing the luminosity and thermal radiation of the flame [22].

Steam-assisted flares account for the majority of flares, although the US has seen an increase in the number of air-assisted flare installations in recent times [23]. Many facilities have access to a boiler on-site and water is readily available to generate steam. Both steam-assisted and air-assisted flares employ a single burner attached to the top of a flare stack that ranges in height, typically from 8 m to over 91 m tall [23]. Flares are elevated as a safety precaution to minimize radiation at ground level. A pilot is installed at the flare tip to ignite the waste gas stream as it exits the flare stack. The operating principle of a steam-assisted flare is to inject steam into the combustion zone in order to generate turbulence and promote mixing of the flare gas with ambient air, thereby eliminating the fuel-rich conditions that result in smoke formation. It has also been proposed that steam injection gives rise to the water-gas shift reaction where CO and water vapor react to form CO_2 and hydrogen (H_2), further promoting complete combustion [21]. There are three common steam injection techniques used. Steam can be injected from nozzles on an external circumferential ring at the tip, from nozzles inside and level with the tip, and from a single nozzle recessed below and concentric to the flare tip. Some designs employ a combination of all three methods.

In some situations, the use of steam can pose a challenge. For instance, in colder climates steam can condense and freeze onto the nozzles and cause blockages. Also, in desert-like conditions such as in the Middle East, installation of steam-assisted flares may not be economically viable due to the scarcity of water [21].

Therefore, air-assisted flares become the optimal choice. To avoid flashback, the flare gas and assist air are kept separate until exiting from the tip of the flare stack, as shown in Figure 1.2. Flare gas is delivered through the gas riser (vertical pipe) that runs coaxially up the center of the flare stack. Low pressure air is delivered through the annular space between the flare stack and the flare gas riser by means of a centrifugal or axial blower mounted at the bottom or side of the flare stack. The air blowers usually operate on either a single or dual speed fan to control the volumetric flow rate of air supplied. Newer systems have implemented variable frequency drives (VFD) on the blowers to facilitate better control of air volume flow rates [24].

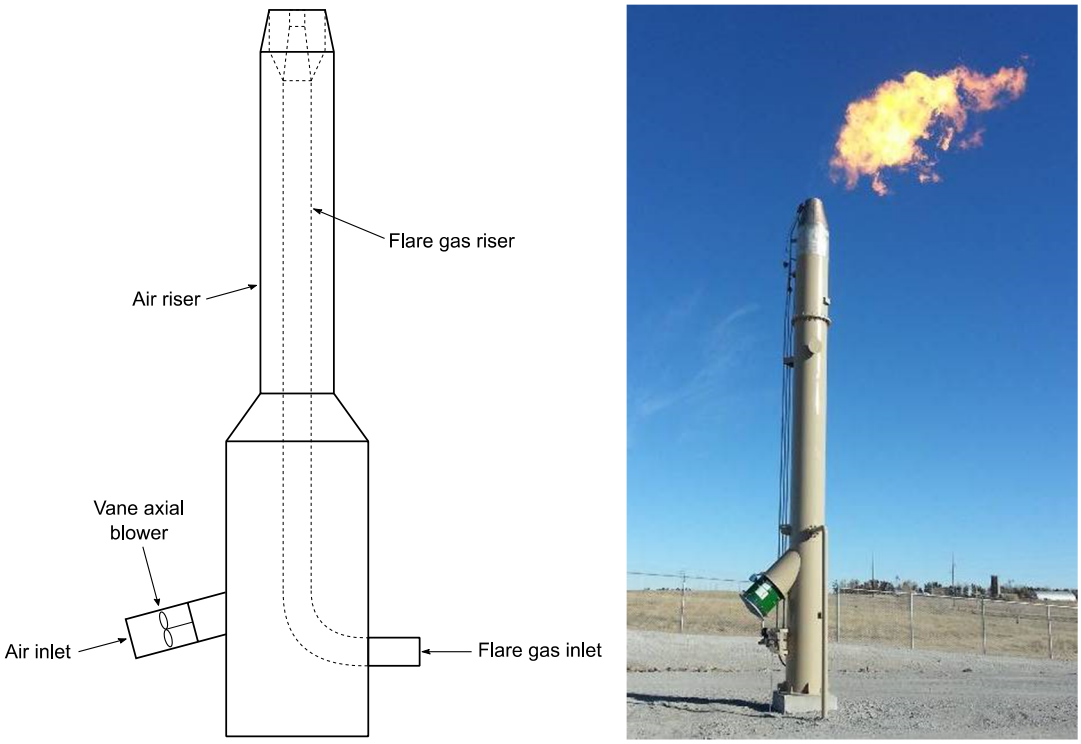

Figure 1.2: (a) A schematic of a typical industrial air-assisted flare, and (b) a photo of an air-assisted flare reproduced from Smith and Seefeldt [24] with permission from Zeeco, Inc.

The flare tip is designed to provide adequate mixing of the flare gas and combustion air to promote smokeless operation. Three of the most common tip designs are illustrated in Figure 1.3 [24]. The most common design is a spider-shaped plate attached at the end of the flare gas riser with many small orifices drilled into the

legs of the spider for the gas to exit. Another design uses triangular slots as the gas exit point. These are usually employed in flare systems with larger gas risers to accommodate higher gas flow rates. Some gas risers are too large for the triangular slot design to provide enough exit area. There is also the concern of black carbon depositing in the narrow section of the slots while flaring heavy hydrocarbon gases. In these cases, air is delivered through an internal bundle of tubes to the flare tip. Flare gas is sent though the spaces in between the tubes.

(a) (b) (c)

Figure 1.3: Common designs for air-assisted flare tips are (a) the drilled spider, (b) triangular slots, and (c) internal tube bundle. The photos are reproduced from Smith and Seefeldt [24] with permission from Zeeco, Inc.

High pressure air-assisted flares are also prevalent in industry. They utilize an external ring of nozzles along the circumference of the flare tip that inject air typically at a gauge pressure of 690 kPa into the combustion zone, as shown in Figure 1.4. This design normally uses a separate pipe outside the flare stack to deliver air to the flare tip. In general, high-pressure air assist is useful for retrofitting an existing flare stack that is experiencing smoke formation. API standards suggest that the mass of air assist required for smokeless combustion is approximately 1.2 times the steam mass [21].

Figure 1.4: External air ring flare tip design reproduced from Smith and Seefeldt [24] with permission from Zeeco, Inc.

In addition to smokeless operating requirements, the US EPA 40 CFR §60.18 proposed flaring regulations with regards to the minimum heat content of the flare gas and limits on exit velocities. It states that the net heating value (*i.e.*, lower heating value) of the gas being combusted must be 11.2 MJ/m^3 or greater if the flare is steam-assisted or air-assisted. Furthermore, air-assisted flares must be designed and operated with a flare gas exit velocity less than the velocity V_{max} (m/s) defined as

$$V_{max} = 8.706 + 0.7084 \times \mathrm{LHV}_{FG}, \tag{1.1}$$

where LHV_{FG} is the lower heating value of the flare gas in MJ/m^3. Flare operators are required to monitor their flares to ensure that they perform in accordance to design regulations. As previously mentioned, an important flare parameter regularly monitored by flare operators is combustion efficiency. In fact, US federal regulations further stipulated in 40 CFR §63.670 that flares must operate with a combustion efficiency of 96.5% or greater at all times [25]. This regulation makes fairly rigorous demands on flare owners or operators to ensure compliance. The main requirement is that the flare facility must establish a continuous monitoring system to measure various flare parameters. These parameters include flare gas flow rate and composition, steam or air assist flow rates, and emission measurements from which combustion efficiency can be calculated. Regulations do not specify measurement protocols to quantify emissions.

Industry has demonstrated that in addition to suppressing soot formation and pollutant emissions, the injection of air or steam into the flare has been shown to be effective in achieving a high combustion efficiency (*i.e.*, $\geq 98\%$) [21]. However, mismanagement of this practice has implicated a number of petrochemical companies in cases of regulatory noncompliance [26,27]. In August 2012, the US EPA sent out an enforcement alert targeting flaring violations in response to the overuse of assist media, namely over-steaming and over-aeration [28]. One consequence of over-assisting the flare is diluting the flare gas to the point where the heating value falls below the 11.2 MJ/m^3 required by statute. This could have the effect of reducing the combustion efficiency of the flare. A more serious consequence of using excessive amounts of steam or air is extinguishing the flame altogether. This extinguishment would result in the venting of flare gas to the atmosphere, which defeats the purpose of flaring. The EPA enforcement alert recommended that flare operators perform continuous measurement and control of the flare gas and assist media flow rates. For air-assist, an automatic damper actuator or VFD could be utilized to offer a greater measure of control over the air supply system.

1.3 Pilot and Industrial Air-Assisted Flare Studies

Achieving a high efficiency flare often proves to be challenging for flare operators. A number of factors impact a flare's ability to achieve complete combustion, such as the flare head design, crosswinds, the composition of the flare gas, and the flow rates of the flare gas and assist media. Several studies have been conducted in the past to observe and analyse industrial air-assisted flares in an open-atmosphere setting that captures the full scope of performance variations. One of the most influential studies was completed by McDaniel [29] in 1983 on behalf of the US EPA. In fact, the emissions results presented in McDaniel's study is reported in the EPA's latest AP-42 publication on industrial flares [30] and are used as a benchmark against which flare operators can compare their flare emissions. The study took place at the John Zink Company flare demonstration facility in Tulsa, Oklahoma. The primary objectives of the study were to determine the combustion efficiency of pilot-scale air-assisted and steam-assisted test flares and to measure the emissions of CO_2, CO, total unburned

hydrocarbons (THC), NO_x, and soot under a range of operating conditions. The test variables were the energy content (*i.e.*, LHV) of the flare gas, flare gas flow rate, and assist media flow rate. The flare gas composition was 80% propylene (C_3H_6) and 20% propane, and the LHV was varied by diluting it with nitrogen (N_2). Samples were collected using a probe suspended over the flare stack. The air-assisted flare had an overall height of 4.01 m. The air blower used for the tests was a 5.6 kW, two-speed vane axial fan located at the base of the 0.46 m inner diameter (ID) air riser. Flare gas was delivered to the flare tip by a 0.10 m outer diameter (OD) internal gas riser. The gas riser employed the "spider" tip design through which the flare gas was discharged. However, the flow rate and velocity of air assist were considered proprietary information and not disclosed in the study. Instead, qualitative descriptors were given to express air flow rate, such as "off", "high", and "low". Raw emissions data were provided in the report for a series of tests done on the air-assisted flare burning either high or low LHV gas mixtures. Emission indices (*i.e.*, the mass of a pollutant species released per unit mass or energy of flare gas) were calculated for each case that exceeded a combustion efficiency of 96.5% to obtain a representative measure of pollutant emissions from a properly operating flare. A maximum emission index for THC, CO_2, CO, and NO_x is shown in Table 1.1 for the high and low LHV gas mixtures. McDaniel also measured soot emitted from the flares corresponding to various degrees of visible smoke. For instance, soot concentrations were reported as 0 μg/L for non-smoking flares, 40 μg/L for lightly smoking flares, 177 μg/L for average smoking flares, and 274 μg/L for heavily smoking flares. It should be noted that these values represent the mass of soot per volume of exhaust products sampled and are not considered to be emission indices as defined above. The reason for this discrepancy was due to the unsuccessful implementation of a tracer method to determine the dilution of the gas sample extracted by the sample probe. McEwen and Johnson [31] showed that it is possible to estimate the soot emissions on a mass per volume of flare gas basis assuming that the soot samples were undiluted and simple stoichiometry is used. The soot emissions were calculated as 0, 0.9, 4.2, and 6.4 g/m^3 flare gas, respectively. A key finding by McDaniel was that flaring low LHV gas mixtures at high exit velocities resulted in lower combustion efficiencies in air-

assisted flares. However, since the study did not reveal the air flow rates associated with high combustion efficiencies, it was not possible to identify an optimal range of performance for an air-assisted flare, and so the results from the study have limited use for flare operators.

Table 1.1: Maximum emission indices of THC, CO_2, CO, and NO_x for a pilot-scale air-assisted flare operating at a combustion efficiency ≥ 96.5% based on a study by McDaniel [29].

Average Flare Gas LHV (MJ/m^3)	Species Emission Indices (g/kg flare gas)			
	THC	CO_2	CO	NO_x
81.3	2.48	3 103	12.18	4.11
7.74[a]	0.33	579	1.60	0.10

[a] Although 40 CFR §60.18 stipulated a minimum flare gas LHV of 11.2 MJ/m^3, McDaniel tested a lower LHV case.

Another EPA-sponsored study was conducted by Pohl and Soelberg [32] in 1985 at the Energy and Environmental Research Corporation's El Toro, California test site. The study investigated the effect of commercial flare head design and flare gas composition on combustion efficiency. The flare gas mixture consisted of propane diluted with nitrogen to vary the LHV of the gas. The experimental methods used in this study were similar to those used by McDaniel in that it was based on extractive sampling of the flare exhaust products. However, major differences in the latter study were the use of a capture hood to collect the entire flare plume and the successful application of a tracer method for accurate emissions measurement. The air-assisted flare head employed the "spider" tip design with a reported equivalent diameter of 3.81 cm. The tests performed for the air-assisted flare used a gas mixture consisting of an average of 44% propane in nitrogen with an LHV of 38.9 MJ/m^3. The combustion efficiency is plotted in Figure 1.5 as a function of the air-to-flare gas mass flow ratio (MFR), where it is implied that both mass flow rates are in the vertical direction. It is difficult to observe a clear trend due to the high degree of scatter. However, it is seen from the figure that the combustion efficiency originates at nearly 100% and drops below the 96.5% threshold at an air-to-flare gas MFR of 3.3.

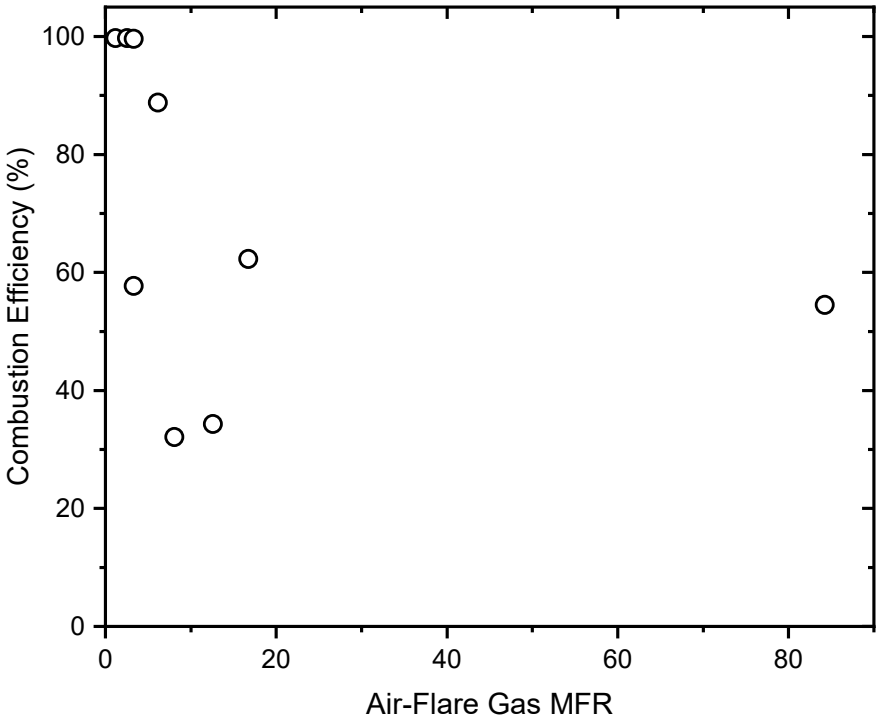

Figure 1.5: Combustion efficiency of an air-assisted flare burning 44% C_3H_8 diluted in N_2 with an overall LHV of 38.9 MJ/m^3, based on a study by Pohl and Soelberg [32].

A further objective of the Pohl and Soelberg [32] study was to assess the influence of air assist on flame stability. Flame stability describes a flame's ability to remain ignited [33] and is characterized by lift-off and blow-off [34]. Flame lift-off occurs when the mean jet velocity exceeds the so-called lift-off velocity, thereby causing the flame to lift above the burner exit. The lift-off height is the distance between the burner exit and the base of the newly stabilized lifted flame. Blow-off refers to the point when the combustion reaction can no longer be sustained due to an exceedingly high jet velocity, resulting in the flame extinguishing. Pohl and Soelberg studied the flame stability limit for a given propane-nitrogen gas mixture by evaluating the minimum LHV required to maintain a stable flame at several velocities. That is, for a certain flare gas velocity, the LHV of the gas mixture was lowered by diluting it with nitrogen until the flame extinguished. The air-assisted flare showed a poor correlation of flame stability with flare gas LHV and exit velocity. Results showed that the flame stability was influenced more strongly by the air-to-flare gas momentum ratio. The study found that the minimum flare gas LHV required to

produce a stable flame increased with increasing air assist flow rate. Emissions of soot, THC, CO, and NO_x were also measured in conjunction with combustion efficiency. However, with the exception of NO_x, emissions were expressed as a percent of unburned combustible products and not in absolute terms. The results showed that over the entire combustion efficiency range tested as the air-to-flare gas stoichiometric ratio (*i.e.*, the ratio of the amount of air assist to the amount of stoichiometric air required to fully combust the flare gas) was increased from 0 to 10, the THC represented 0.1% to 100% of the unburned combustible products, CO represented 0.1% to 10%, and soot 0.01% to 0.1%. Over the same combustion efficiency range, NO_x concentrations dropped from 100 ppm to 1 ppm. The maximum NO_x concentration was converted to an emission index of 1.28 g NO_x/kg flare gas and corresponded to a combustion efficiency ≥ 96.5%.

An important caveat mentioned in the study was that small-scale laboratory flares were not aerodynamically comparable to pilot-scale or industrial flares. The aerodynamic characteristics of a flare was defined in terms of the Reynolds number and the Richardson number evaluated at the flare exit. The Reynolds number is a measure of the relative strengths of inertial to viscous forces, and the Richardson number is a measure of the relative strengths of buoyant to inertial forces [35]. It was observed that as the flare size decreased, the Reynolds and Richardson numbers also decreased. For instance, the flare gas Reynolds number of commercial flare heads with a diameter of 61 cm ranged approximately from 10^3 to 10^7, and the Richardson number ranged from 10^{-5} to 10^4. The 2.54 cm and 3.81 cm air-assisted flare head in Pohl and Soelberg [32] had a flare gas Reynolds number ranging from 10^4 to 10^6 and a Richardson number ranging from 10^{-6} to 10^{-1}.

The most recent industrial air-assisted flare study was conducted in 2010 by Allen and Torres [36] for the Texas Commission on Environmental Quality (TCEQ) at the John Zink Company flare test facility in Tulsa, Oklahoma. The purpose of this project was to perform field tests in a semi-controlled environment (*i.e.*, controlled flare operations but uncontrolled ambient conditions) and assess the potential impact of flare design, operating conditions, and flare gas LHV and flow rate on pollutant emissions and combustion efficiency. A key feature that differentiated this study from

those done previously is that measurements were taken directly from full-scale industrial flares, rather than pilot-scale flares. A single air-assisted flare design was selected for the study as it was deemed to be representative of a large number of flares used in industry. The flare had a nominal diameter of 61 cm and the flare tip was 10.1 m above ground level. The air blower was equipped with a VFD motor to control the supply of air. The air assist flow rate ranged from a minimum, defined by the incipient smoke point (ISP), to a maximum which was marked by blow-off. The study defined ISP as an operating condition when no visible emissions were observed two flame lengths away from the flare tip. The flare head utilized triangular arms as the flare gas exit point. The flare gas composition used in this study was a mixture of natural gas, propylene or propane, and nitrogen. Natural gas was mixed with propylene or propane in a 1:4 ratio by volume (the air-fuel mass ratio for stoichiometric combustion of a 20% natural gas and 80% propylene blend is 15, and for a 20% natural gas and 80% propane blend it is 14). Nitrogen was used to dilute the flare gas mixture to an LHV of approximately 13 MJ/m^3 and 22 MJ/m^3. The air flare had a flare gas design capacity of about 65 000 kg/hr of propylene. Flow rates of 0.25% and 0.65% of design capacity were selected to represent the range of interest of the TCEQ, which amounted to 163 kg/hr and 425 kg/hr, respectively. Five tests were conducted to evaluate the combustion efficiency of the flare with varying operating parameters. The trends are plotted in Figure 1.6. Tests A3 to A6 used a flare gas mixture of natural gas, propylene, and nitrogen. Test A7 substituted propane for propylene. Generally, it was observed that the flare gas mixture with an LHV of 13 MJ/m^3 achieved a combustion efficiency $\geq$ 96.5% at an air-to-flare gas MFR less than 22, and the flare gas mixture with an LHV of 22 MJ/m^3 achieved a combustion efficiency $\geq$ 96.5% at an air-to-flare gas MFR less than 44.

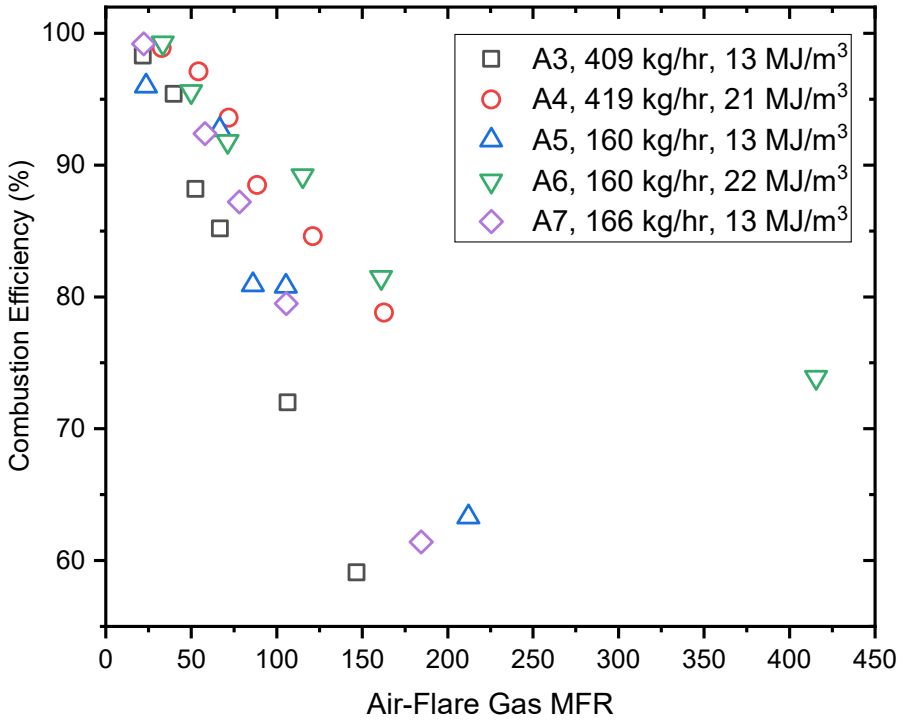

Figure 1.6: Combustion efficiency of an air-assisted flare burning gas mixtures consisting of natural gas, C_3H_6 or C_3H_8, and N_2 based on a study by Allen and Torres [36].

Allen and Torres also investigated various pollutant emissions emitted by flares. Figure 1.7a shows THC emission indices of select air-assist flare tests and their respective combustion efficiencies. Only a single test point exceeded 96.5% combustion efficiency corresponding to a THC emission index of 1.3 g THC/kg flare gas. The plot illustrates an inverse relation between combustion efficiency and THC emissions, in that with increasing air assist the combustion efficiency drops steadily and THC emissions increase. This is to be expected since a decrease in combustion efficiency indicates that less hydrocarbons are being converted to CO_2 due to incomplete combustion. NO_x emissions were also measured for test A7 (1:4 ratio by volume of natural gas to propane) and analyzed by Torres *et al*. [37]. Figure 1.7b presents the trends for NO_x emission indices and combustion efficiency. For a combustion efficiency $\geq$ 96.5%, the maximum NO_x emission index was 0.39 g NO_x/kg flare gas and decreased by a factor of two as combustion efficiency dropped to 90%. It was observed that flaring low LHV gases and operating at low combustion efficiency both contributed to lower flame temperatures, which

resulted in reduced NO_x formation. A separate study by Fortner *et al*. [38] focused on particulate emissions measured during the TCEQ study. However, the analysis by Fortner *et al*. was limited to a single air-assisted flare test and BC emission indices were not specified. The main conclusion derived from that study was that air assist significantly reduced BC concentrations, although not as effectively as steam.

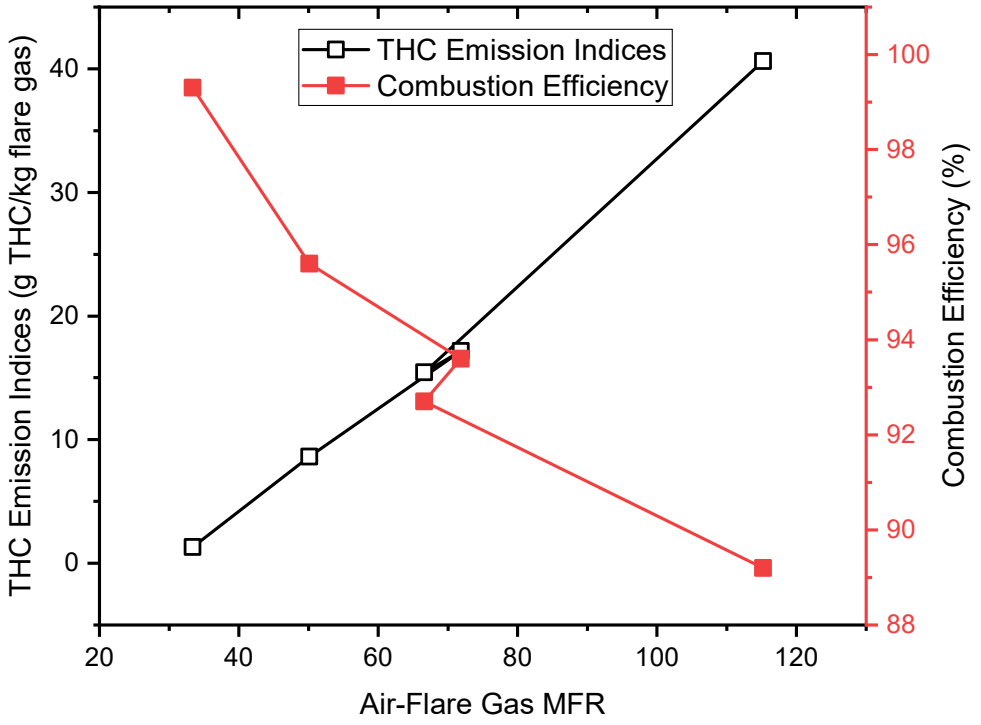

(a)

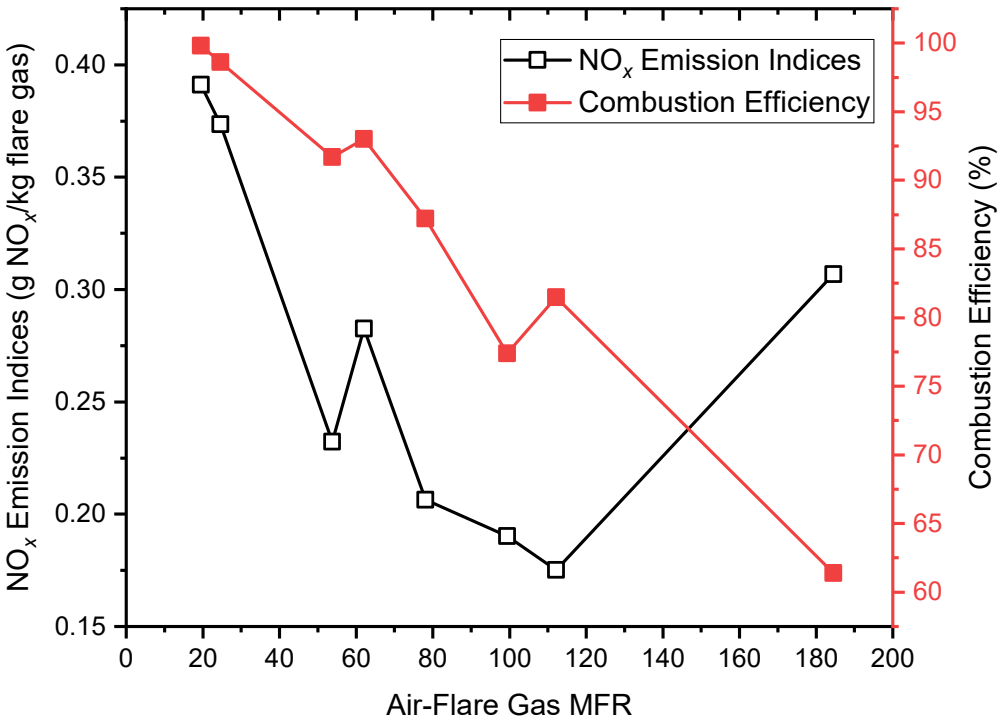

(b)

Figure 1.7: Emission indices for (a) THC and (b) NO_x from an air-assisted flare burning gas mixtures consisting of natural gas, C_3H_6 or C_3H_8, and N_2 based on a study by Allen and Torres [36,37].

1.4 Research Objectives

Despite efforts by the EPA to elucidate and enforce proper flare operation, flaring violations are an ongoing dilemma largely due to ineffective handling of air assist. This issue stems from a lack of clear understanding as to the impact of air assist on a combustion process, specifically regarding flare combustion efficiency and pollutant emissions. Admittedly, a key reason for the shortcomings in flare operating methodologies is the inherent challenge in quantifying emissions from an open atmosphere industrial-scale turbulent diffusion flame. Therefore, the goal of the present study was to investigate the nature of flaring violations in the form of over-aeration and to provide fundamental insights into air-assisted flare emissions at the lab scale. The research was conducted at the University of Alberta in collaboration with the Natural Sciences and Engineering Research Council of Canada (NSERC) FlareNet Strategic Network. The main research objectives were to:

1. Equip a lab-scale flare facility with the appropriate means to enable the safe undertaking of combustion experiments in a controlled environment, namely, the means to continuously collect and dispose of exhaust gases.
2. Design and construct a dual-stream burner to facilitate the injection of air into the fuel stream, which includes the system for handling, metering, and the controlled discharge of air and fuel.
3. Perform exploratory emissions measurements for the combustion of representative fuel gases and simulate over-aeration in industrial flares by incrementally increasing air injection to trigger flame blow-off.
4. Investigate the effectiveness of air-assist as a method for maintaining high combustion efficiency while reducing pollutant emissions.

The remainder of the thesis will proceed as follows: Chapter 2 will establish the experimental setup including a detailed description of the burner, sampling system, diagnostic equipment, and methodologies used to calculate combustion efficiency and emission indices. Chapter 3 will present the results obtained from the experiments and a discussion of observations, trends, and comparisons. Finally, Chapter 4 will summarise key findings, provide concluding remarks, and make suggestions for future work.

Chapter 2

2. Experimental Setup

2.1 Burner Design

A motivating factor for the present study was the need to develop a fundamental understanding of the characteristics of air-assisted flares through a systematic evaluation of a lab-scale air-assisted flare, also referred to as a burner. A key challenge in designing the burner was selecting an appropriate geometry to allow for parallel flow of the fuel stream and air assist stream, keeping in mind the flare head designs prevalent in industrial-scale flares. The industrial flare heads shown in Figure 1.3 all share the idea of discharging the flare gas and air assist from the same exit plane; however, they differ significantly with respect to the air injection method. Due to the exploratory nature of the present study, it was not deemed pertinent to test all the different flare head designs. Instead, a generic flow geometry was chosen to capture the critical elements of air-assisted flares, namely, a concentric coflow of a hydrocarbon fuel with air.

The burner design is illustrated in Figure 2.1, showing an external and cross-sectional view. The burner consists of two concentric stainless-steel tubes that are coincident at their exit planes. The tubes are fixed relative to one another by means of a 3-way tee which facilitates separate and parallel flow of the fuel and air. The outer tube has an OD of 25.4 mm, an ID of 22.9 mm, and an overall length of 305 mm. The inner tube has an outer diameter (OD) of 12.7 mm, an inner diameter (ID) of 11.3 mm, and an overall length of 457 mm. Three set screws were inserted through threaded holes spaced 120° apart and located half-way down the outer tube. The set screws

were used to align the inner tube and ensure concentricity. The burner was also tested with an inner tube of 6.35 mm OD and 5.54 mm ID. Flow through the burner was primarily configured such that the air was delivered through the inner tube with coflowing fuel through the annular space between the tubes. The inverse flow scheme (*i.e.*, the fuel delivered through the inner tube) was also carried out as a separate test.

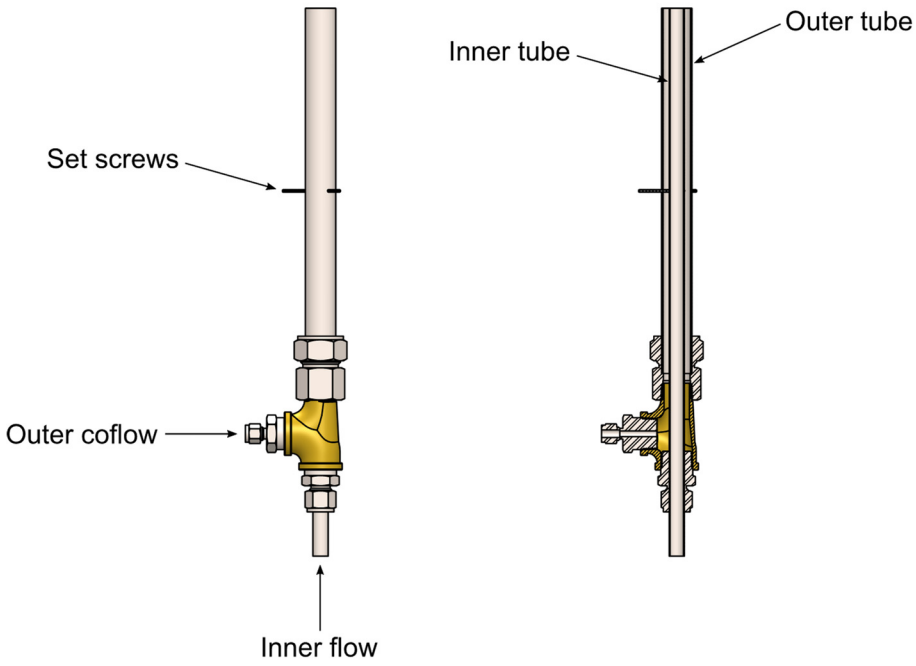

Figure 2.1: An overall and cross-sectional view of the burner is depicted. Air enters the bottom port of the tee and travels the entire length of the inner tube before exiting from the burner tip. Coflowing fuel enters the side port and travels through the annular space between the inner and outer tubes before exiting from the burner tip.

Another design aspect of the burner was the arrangement of thermocouples along the side of the outer tube and the center of the inner tube, as shown in Figure 2.2. The coordinate axes consist of a vertical z-axis and a horizontal r-axis that intersect a point coincident with the burner exit plane and the center of the inner tube. The temperature of the inner flow was measured at $(r, z) = (0, 0)$ using an exposed junction T-type thermocouple (Omega Engineering, TSS Series) with a wire diameter of 0.81 mm and a sheath OD of 1.59 mm. The thermocouple was inserted through the bottom inlet of the inner tube until the junction was made level with the exit plane. For measuring the outer coflow temperature, five holes 0.91 mm in diameter were

drilled at z = −2.5, −5, −10, −20, and −40 mm along the outer tube. An exposed junction T-type thermocouple (Omega Engineering, 5SRTC Series) with a wire diameter of 0.13 mm was inserted into each hole normal to the flow direction. The topmost thermocouple was bent at a 90° angle to position the junction at z = 0 mm for measuring the coflow temperature at the exit. The junctions of the outer coflow thermocouples were located at r = 8.9 mm, which is the midpoint of the annular space between the inner and outer tubes. Each thermocouple junction was wrapped in aluminum foil to lessen the effect of radiation from the flame on the temperature measurements. The wire leads on the end of the thermocouples were connected to a temperature data acquisition module (National Instruments, NI-9213) to record temperature, with an overall uncertainty of ±1 °C. Refer to Appendix A for a discussion on the methodology used for estimating uncertainty.

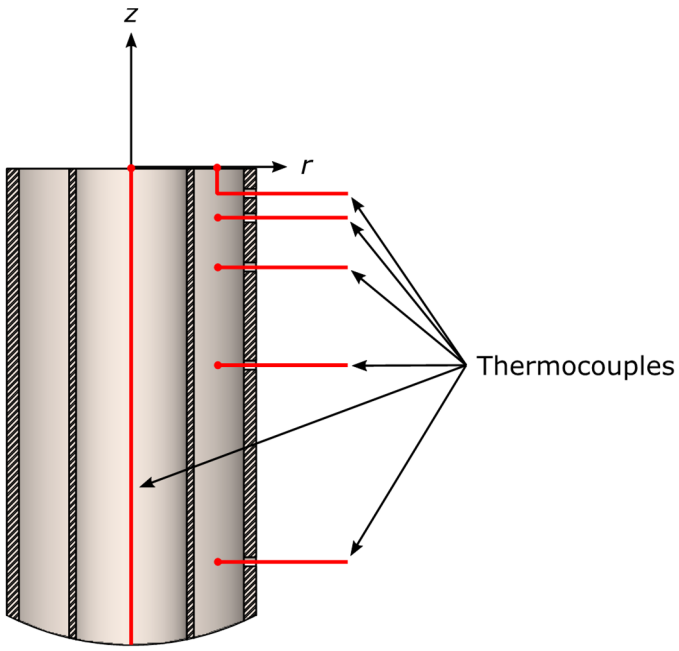

Figure 2.2: Thermocouple arrangement for measuring the inner flow temperature at the inner tube exit and outer coflow temperature at various positions along the annular gap.

2.2 Lab-Scale Flare Facility

A major research objective was to develop a flare testing facility to enable the safe and controlled performance of combustion experiments. Figure 2.3 shows the results

of this effort. The central feature of the facility was the burner and aluminum frame assembly. The burner was mounted on a pair of horizontal bars (one shown in the figure) which in turn were bolted to four vertical rails (two shown in the figure). The rails have bolt holes spaced 3.81 cm apart to allow for raising or lowering of the burner; however, for the most part the burner was elevated such that the exit plane was 84.9 cm above the floor. The burner is located directly beneath a square exhaust hood with sides measuring 91 cm and suspended 213 cm above the floor. Vinyl-coated polyester mesh screens were hung from each side of the exhaust hood and extended to the floor. The screens had 1.59 mm square openings (blockage ratio of 55%) to minimize flame instability due to air currents in the lab, while enabling sufficient entrainment of combustion air.

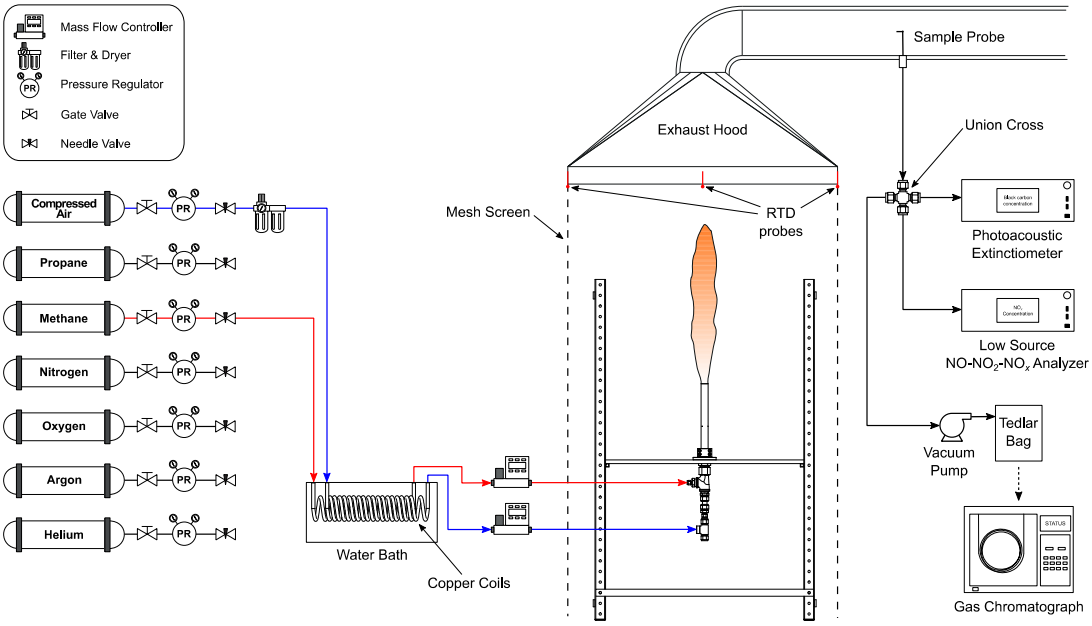

Figure 2.3: Flare facility equipped with a lab-scale air-assisted flare (burner), an array of compressed gas cylinders and gas metering equipment, a sampling system, and diagnostic equipment.

The hydrocarbon fuel gases tested in this study were methane and propane. High purity (99.97%) methane was stored in a T-type compressed gas cylinder (Praxair, ME 3.7UH-T) with an LHV of 32.8 MJ/m^3, and 99.5% pure propane (Praxair, PR 2.5IS) was stored in an FX-type compressed gas cylinder with an LHV of 84.9 MJ/m^3. The fuel gas was dispensed at 276 kPa from the pressure regulator to

a circulating water bath (Thermo Scientific, TSCIR35) using plastic tubing with 12.7 mm OD and 9.53 mm ID. The plastic tubing transitioned to a copper coil inside the water bath (represented by the red dashed line in Figure 2.3) with an uncoiled length of 3.81 m, a 12.7 mm OD and 11.1 mm ID. The water bath had a capacity to hold 35 L of water and was set to a temperature of 35 °C at all times to regulate the temperature of the gas passing through the copper coil to about room temperature (23 °C). Plastic tubing carried the fuel gas from the water bath to a 50 SLPM (standard liters per minute corrected to 25 °C and 101.3 kPa) mass flow controller (Alicat, MCR 50 slpm) with a measurement uncertainty of ± (0.8% of reading + 0.1 SLPM). For the fuel coflow experiments, the flow controller was connected to the outer coflow port indicated in Figure 2.1. Pressurized air supplied by the mechanical engineering building's air compressor was dispensed at 276 kPa and an average temperature of 23 °C, filtered (Parker, H-Series), and flowed through the water bath before entering either a 100 SLPM (Alicat, MCR 100 slpm) or 1 000 SLPM (Alicat, MCR 1000 slpm) mass flow controller, depending on the air flow rate requirement, with respective uncertainties of ± (0.8% of reading + 0.2 SLPM) and ± (0.8% of reading + 2 SLPM). The flow controller was then connected to the inner tube of the burner to facilitate air-assisted flaring. It is important to note that each mass flow controller was calibrated for various gases using a drum-type gas meter (Ritter, TG-50). Results of the calibration showed that the mass flow controllers were within the error specified by the manufacturer. Refer to Appendix B for more details on the calibration setup and results.

The remaining T-type compressed gas cylinders shown in Figure 2.3 were 99.998% nitrogen (Praxair, NI 4.8-T), 99.993% oxygen (Praxair, OX 4.3UH-T), 99.998% argon (Praxair, AR 4.8-T), and 99.995% helium (Praxair, HE 4.5-T). These gases were used for a subset of the experimental study, which attempted to substitute air assist with specified mixtures of oxygen (O_2) and inert gases, namely, nitrogen, argon (Ar), and helium (He), that had overall molecular weights equivalent to air (*i.e.*, 28.96 g/mol based on the four most common gases in dry tropospheric air at 101.3 kPa by volume: 78.084% N_2, 20.946% O_2, 0.934% Ar, and 0.0379% CO_2 [39]). From the ideal gas law (assuming constant pressure and temperature), by matching the

molecular weight of a gas mixture to air, the density is matched too. The goal of the so-called "equivalent air assist" experiment was to evaluate the effect of changing the oxidant level in the assist mixture on combustion efficiency and emission indices, while maintaining the initial hydrodynamic characteristics of air. Figure 2.4 demonstrates an equivalent air assist experiment with no oxidant present in the assist mixture (*i.e.*, 92% N_2 and 8% Ar by volume). The N_2 and Ar streams were pre-heated in the water bath and then joined at a 3-way tee downstream of their respective flow controllers, before being transmitted via a single length of plastic tubing to the inner tube of the burner. Two more equivalent air assist experiments were conducted and used a triple-gas mixture to manipulate the oxidant level in the assist stream. One of them consisted of half the volume of O_2 found in air (*i.e.*, 85% N_2, 10.5% O_2, 4.5% Ar), and the other consisted of twice the volume of O_2 found in air (*i.e.*, 55% N_2, 42% O_2, 3% He). These triple-gas air assist mixtures were likewise pre-heated and joined at a union cross (not shown in Figure 2.4) before being transmitted to the inner tube. The tee and union cross allowed for the gas streams to impinge on each other at 180° and 90°, respectively, to promote mixing. Furthermore, the plastic tube was sized sufficiently small in diameter (6.35 mm OD and 4.32 mm ID) to induce fully turbulent flow at a flow rate of 15 SLPM, corresponding to a Reynolds number > 4 500.

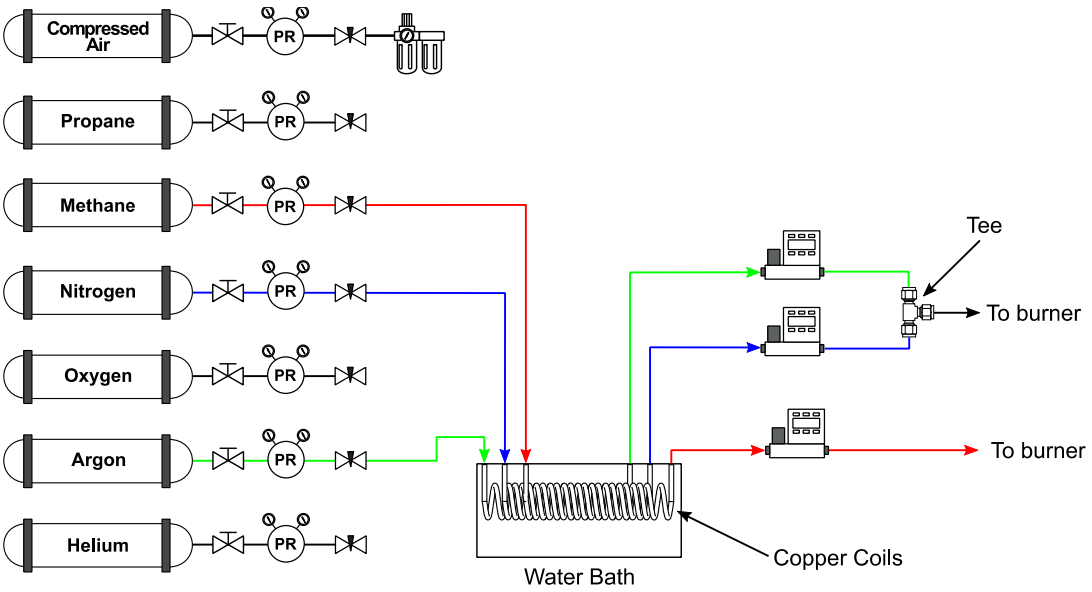

Figure 2.4: A gas mixture consisting of 92% N_2 and 8% Ar by volume to simulate air are mixed at a 3-way tee before entering the inner tube of the burner.

The combustion products generated by the burner were captured by the exhaust hood (as well as dilution air) and traveled through a circular duct with a diameter of 30 cm to a Venturi air control valve (Phoenix Controls). The valve was configured to limit the flow rate through the duct to 17 m^3/min with a corresponding Reynolds number of about 78 000 based on average room temperature and pressure measurements of 23 °C and 93.1 kPa, respectively. The valve houses a spring-loaded cone element that extends or retracts in response to changes in the duct pressure to maintain a constant flow rate. An air pressure proving switch is mounted on the duct and triggers an alarm if the building fan fails. A Resistance Temperature Detector (RTD) probe (McMaster-Carr, 1237N12) was attached to each side of the exhaust hood, as shown in Figure 2.3, with each tip extending about 1 cm below the edge. The RTD measurements were used to detect overflowing of hot product gases outside the exhaust hood which was indicated by an increase in temperature. Escaping of product gases into the lab space was considered a safety hazard and potentially compromised the experimental results. Extraction of combustion products was facilitated by a 6.35 mm OD, L-shaped stainless-steel probe inserted through a port in the duct 6 m downstream of the exhaust hood. Samples taken from this location were found to be homogeneous at various radial positions in the duct and so fully mixed. The open end of the probe was welded to a 1.59 cm OD copper tube 2 m in length which terminated in a union cross. Flexible tubing was used to carry the duct sample from the union cross to a suite of diagnostic equipment, which consisted of a photoacoustic extinctiometer (Droplet Measurement Technologies, PAX), a NO_x analyzer (Thermo Scientific, 42iQLS), and a diaphragm vacuum pump (GAST Manufacturing, DOA Series) for filling a 10 L Tedlar bag (Cole-Parmer, ESS Series) with a sample of the duct gas for offline GC measurements. Since the photoacoustic extinctiometer (PAX) quantified BC particle emissions, a 4.5 m length of static-dissipative silicone rubber tubing (McMaster-Carr, 1909T7) with 9.53 mm OD and 6.35 mm ID was used to transmit the duct sample to the PAX. The use of conductive tubing eliminated particle loss (*i.e.*, particle deposition onto the interior wall of the tube) due to electrostatic forces.

As for the operating principle, the PAX is an instrument used for measuring aerosol optical properties. The two key optical properties it measured were light absorption and scattering of aerosol particles, from which extinction (sum of absorption and scattering), single scattering albedo (ratio of scattering to extinction), and BC mass concentration are derived. The PAX employs a modulated diode laser to simultaneously measure light absorption and scattering. The laser operates at a wavelength of 870 nm which is particularly effective for BC particles, since absorption from gases and non-BC aerosols are comparatively small at this wavelength. The duct sample is drawn into the PAX at a flow rate of 1 L/min by an internal vacuum pump. The sample then flows to two separate chambers, a nephelometer for the measurement of light scattering and a photoacoustic resonator for measuring absorption. In the photoacoustic cell, particles absorb heat from the laser (infrared radiation) which is transferred to the surrounding air. The unsteady heat transfer generates pressure waves that are transmitted to a microphone and correlated to an absorption coefficient. The nephelometer integrates the light scattered by the particles over a wide angle and calculates a scattering coefficient. The formula used to calculate BC mass concentration in units of $\mu g/m^3$ is provided in the device manual [40] as

$$f_m = \frac{B_{\text{abs}}}{\text{MAC}}, \tag{2.1}$$

where B_{abs} is the absorption coefficient (1/Mm) and MAC is the BC mass absorption cross-section (m^2/g). For a laser wavelength of 870 nm, a default MAC value of 4.74 m^2/g is stated in the manual for fresh soot with an uncertainty of ±0.76 m^2/g. The uncertainty estimate for the measurement of B_{abs} is given by the B_{abs} noise, which was also used to calculate the uncertainty in f_m. The uncertainty in f_m was found to be about 1% of the measured values.

The NO_x analyzer operates on the principle of chemiluminescence (*i.e.*, the emission of light due to a chemical reaction) to measure the concentration of NO_x in the duct sample. The analyzer offers two measurement ranges: 0 to 100 ppm with an

uncertainty of ±1 ppm and an extended range of up to 500 ppm with an uncertainty of ±5 ppm. The underlying reaction occurs when nitric oxide (NO) interacts with O_3 to form excited nitrogen dioxide (NO_2) and O_2. The NO_2 molecules decay to a lower energy state and thereby generate infrared radiation with an intensity linearly proportional to the NO concentration. The duct sample is drawn into the NO_x analyzer by an internal vacuum pump at a flow rate of 0.1 L/min. It is important to note that the device only measures NO. It does not directly measure the NO_2 concentration present in the duct sample. The NO_2 must first be converted into NO by a NO_2-to-NO converter via thermal degradation at 625 °C. As such, two steps are required to measure both NO and NO_2. First, the sample flows to a solenoid valve which directs it to the reaction chamber to undergo chemiluminescence. A sample is also sent to the NO_2-to-NO converter to breakdown NO_2. The treated sample is redirected to the reaction chamber from which NO is measured, which is in fact the total NO_x concentration. NO_2 is calculated by subtracting the initial NO measurement from the subsequent NO_x measurement. An ozonator built into the NO_x analyzer generates the O_3 needed for the chemiluminescent reaction. A photomultiplier detects the luminescence generated by this reaction.

When a Tedlar bag was filled with a sample from the duct, it was taken to a gas chromatograph (Agilent, 7890B). The contents of the Tedlar bag were pumped into the gas chromatograph (GC) using a vacuum pump to measure the mole concentration of O_2, N_2, C1 to C3 hydrocarbons, CO and CO_2. The hydrocarbons in the sample are quantified by a Flame Ionization Detector (FID). The FID consists of a hydrogen-air diffusion flame into which the sample is injected [41]. The FID is often called a carbon counting device because combustion of a hydrocarbon sample in a hydrogen flame yields an electrical current linearly proportional to the amount of carbon contained in the sample [42]. Although the mechanism by which the detector ionizes the sample is still not completely understood [43], research on this phenomenon suggests that when an organic compound is drawn into a hydrogen flame, a positively charged ion, namely the formylium ion (CHO+) is formed [44]. Under the influence of an electric potential, the positive ions are drawn towards a collector electrode. The resulting current is integrated over time to obtain the total

charge, which is correlated to a hydrocarbon concentration. The O_2, N_2, CO and CO_2 are quantified by a Thermal Conductivity Detector (TCD). The sample is mixed with a carrier gas, typically helium or hydrogen [45], and enters the TCD, which employs an electrically heated filament kept at a constant temperature [46]. When a gas passes over the filament, the power required to keep the temperature of the filament constant changes by a certain degree due to the unique thermal conductivity of the gas stream. A solenoid valve switches the flow over the filament between the sample gas and pure carrier gas. A difference in power is measured proportional to the concentration of the sample. Once the sample analysis is complete, the GC generates chromatograms that show peaks corresponding to the gas-phase species detected in the sample, as well as a breakdown of the species mole concentrations. The GC was calibrated by injecting calibration standards (*i.e.*, gas samples with specified species concentrations representative of those found in the Tedlar bag samples) to generate calibration curves. Refer to Appendix C for a list of the calibration standards used and the uncertainty associated with the relevant gas species.

2.3 Methodology for Measuring Carbon Conversion Efficiency and Emission Indices of a Lab-Scale Air-Assisted Flare

The concept of carbon conversion efficiency (CCE) is accompanied with the notion of incomplete combustion. For a general hydrocarbon fuel, incomplete combustion is represented by the following equation:

$$C_xH_y + O_2 \longrightarrow bCO_2 + dH_2O + eCO + fCH_4 + \sum_{m,n} g_{m,n}\, C_mH_n + hC_{(s)}, \quad (2.2)$$

where N_2 is excluded from the equation for simplicity because it does not participate in carbon-based reactions. The products of incomplete combustion are CO, unburned CH_4, unburned and reformed non-CH_4 hydrocarbons (C_mH_n), and soot in the form of carbon.

The underlying method for quantifying the CCE of a flame at any given test condition was a carbon mass balance. This method was developed by Corbin and

Johnson [47] based on a control volume enclosing the combustion process. As shown in Figure 2.5, a control volume was drawn around the burner and exhaust hood. The various carbon-containing species were depicted either entering or exiting the control volume.

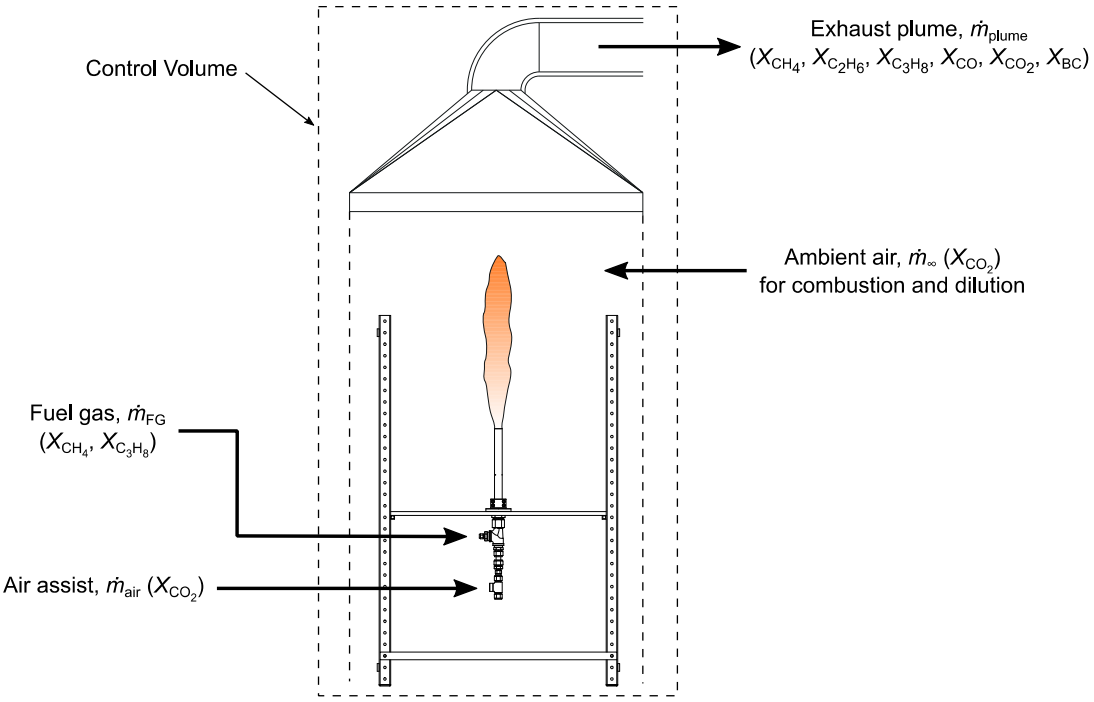

Figure 2.5: A control volume encloses the burner and exhaust hood and the relevant carbon streams are identified. Mole fractions of carbon-containing species are represented as X_k.

The CCE (η) is defined as the ratio of the mass of carbon in the form of CO_2 that was produced by combustion (not including the CO_2 already present in the incoming air or fuel streams), $\dot{m}_{C,CO_2,produced}$, to the mass of carbon derived from the hydrocarbon component of the fuel gas, $\dot{m}_{C,HC,FG}$,

$$\eta[\%] = \frac{\dot{m}_{C,CO_2,produced}}{\dot{m}_{C,HC,FG}} \times 100. \quad (2.3)$$

The numerator and denominator of Eq. 2.3 are in fact mass flow rates of atomic carbon. As such, the CCE can be expressed as a ratio of the molar flow rate of

CO_2 produced by combustion, $\dot{n}_{CO_2,\text{produced}}$, to the molar flow rate of carbon in the fuel gas, $x(X_{C_xH_y,FG})\dot{n}_{FG}$,

$$\eta[\%] = \frac{\dot{n}_{CO_2,\text{produced}}}{x(X_{C_xH_y,FG})\dot{n}_{FG}} \times 100, \tag{2.4}$$

where x represents the number of carbon atoms indicated in the molecular formula of the collective hydrocarbon in the fuel gas (*e.g.*, if the fuel gas consisted of a mixture of CH_4, C_2H_6, and C_3H_8, x would be calculated based on the mole fractions of the individual components, as in $x = 1 \times X_{CH_4} + 2 \times X_{C_2H_6} + 3 \times X_{C_3H_8}$), and $X_{C_xH_y,FG}$ is the mole fraction of the hydrocarbon component of the fuel gas (< 1 if the fuel gas consisted of non-hydrocarbon gases). The numerator of Eq. 2.4 is further expressed as

$$\dot{n}_{CO_2,\text{produced}} = X_{CO_2,\text{plume}}\dot{n}_{\text{plume}} - X_{CO_2,\infty}\dot{n}_{\infty} - X_{CO_2,FG}\dot{n}_{FG}, \tag{2.5}$$

where the terms on the right-hand side represent, in order of their appearance: the total molar flow rate of CO_2 in the exhaust plume, the molar flow rate of CO_2 present in the ambient air that is drawn into the duct (this also includes the CO_2 in the air assist injected into the flame and is based on an average ambient CO_2 reading of 460 ppm), and the molar flow rate of CO_2 present in the fuel gas, if any (typically in natural gas). The denominator of Eq. 2.4 is expanded as

$$\begin{aligned} x\left(X_{C_xH_y,FG}\right)\dot{n}_{FG} &= \textstyle\sum_k \#_{C,k}\left(X_{k,\text{plume}} - X_{k,\infty}\frac{M_{\text{plume}}}{M_{\infty}}\right)\dot{n}_{\text{plume}} + \\ &\textstyle\sum_k \#_{C,k}\left(X_{k,\infty}\frac{M_{FG}}{M_{\infty}}\dot{n}_{FG}\right) - X_{CO_2,FG}\dot{n}_{FG}, \end{aligned} \tag{2.6}$$

where $\#_{C,k}$ is the number of carbon atoms represented by the molecular formulas of the various gas species, k, found in the exhaust plume (*i.e.*, $\#_{C,CO_2} = 1$, $\#_{C,CH_4} = 1$, $\#_{C,C_3H_8} = 3$, or in general, $\#_{C,C_mH_n} = m$), M_{plume}, M_{∞}, and M_{FG} are the molecular weights of the plume, ambient air, and fuel gas, respectively. The terms on the right-

hand side of Eq. 2.6 reflect those in Eq. 2.5, in that they correspond to the molar flow rate of the plume, ambient air, and fuel gas, but instead in relation to the fuel. The equation for $\dot{n}_{\text{plume}}$ is expressed as follows:

$$\dot{n}_{\text{plume}} = \frac{\left[x\left(X_{\text{C}_x\text{H}_y,\text{FG}}\right)\dot{n}_{\text{FG}} + X_{\text{CO}_2,\text{FG}}\dot{n}_{\text{FG}} - \left(X_{\text{CO}_2,\infty} + X_{\text{CO},\infty} + X_{\text{CH}_4,\infty} + \sum_k \#_{C,\text{C}_m\text{H}_n} X_{\text{C}_m\text{H}_n,\infty}\right)\frac{M_{\text{FG}}}{M_\infty}\dot{n}_{\text{FG}}\right]}{\left[X_{\text{CO}_2,\text{plume}} - X_{\text{CO}_2,\infty} + \frac{f_{m,\text{plume}} R_u T_{\text{plume}}}{M_{\text{C(s)}} P_{\text{plume}}} + X_{\text{CO,plume}} - X_{\text{CO},\infty} + X_{\text{CH}_4,\text{plume}} - X_{\text{CH}_4,\infty} + \sum_{m,n} \#_{C,\text{C}_m\text{H}_n}\left(X_{\text{C}_m\text{H}_n,\text{plume}} - X_{\text{C}_m\text{H}_n,\infty}\right)\right]}, \tag{2.7}$$

where $f_{m,\text{plume}}$ is the measured soot mass fraction in the plume, R_u is the universal gas constant (8.314 J/mol·K), T_{plume} is the temperature of the plume gas measured using an RTD probe (Omega, PR-31 Series), and P_{plume} is the static pressure in the duct measured using a pressure transducer (Omega, PX409-100AI). It is important to note that BC mass concentration was measured with the PAX at cell conditions independent of plume conditions. Therefore, the measured soot mass fraction was corrected to obtain an actual soot mass fraction by taking the difference between the cell and plume temperatures into account, as in

$$f_{m,\text{plume}} = f_{m,\text{measured}} \frac{T_{\text{cell}}}{T_{\text{plume}}}. \tag{2.8}$$

The value calculated for $\dot{n}_{\text{plume}}$ is substituted back into Eq. 2.5 and 2.6, before finally solving for CCE defined by Eq. 2.4.

Another parameter of interest in this study is the emission index (EI) of pollutant species which have detrimental effects on the environment. For any given species, an emission index was calculated from the ratio of the species emission rate measured in the plume to the mass flow rate of the fuel gas, as

$$EI_j = \frac{\dot{m}_{j,\text{produced}}}{\dot{m}_{\text{FG}}}, \tag{2.9}$$

where j indicates either species or classes of species of interest, namely, CO, CO_2, THC, NO_x, and BC. When evaluating gas-phase emission indices, the numerator of Eq. 2.9 is expressed as

$$\dot{m}_{j,\text{produced}} = M_j \left(\left(X_{j,\text{plume}} - X_{j,\infty}\right)\dot{n}_{\text{plume}} - \left\{ X_{j,\text{FG}} \frac{\dot{m}_{\text{FG}}}{M_{\text{FG}}} \right\}_{\text{inert}} + X_{j,\infty} \frac{\dot{m}_{\text{FG}}}{M_\infty} \right), \tag{2.10}$$

whereas for BC emission indices the numerator is expressed as

$$\dot{m}_{\text{C(s)},\text{produced}} = f_{m,\text{measured}} \frac{R_u T_{\text{cell}}}{P_{\text{plume}}} \dot{n}_{\text{plume}}. \tag{2.11}$$

A detailed uncertainty analysis was performed for carbon conversion efficiency and emission indices by means of propagation of uncertainties associated with each independently measured quantity. The bias and precision errors generated by the various instruments used in the experiments were tracked and incorporated in the analysis. Refer to Appendix D for the uncertainty analysis.

Chapter 3

3. Results and Discussion

3.1 Test Matrix

A total of 8 unique sets of experiments were conducted in the present study and are summarized in Table 3.1. The first set established the "standard" case. It consisted of an outer coflow of CH_4 at a constant 20 SLPM and air injected through an inner tube with a 12.7 mm OD. Since it was unclear what the most sensitive parameters were, it was deemed necessary to explore changes in the inner tube size, fuel type and flow rate, and assist configuration and composition. For each set the flow rate of air was incrementally increased from no flow until the flame CCE dropped to less than 10%. The flame was allowed to come to steady state at each incremental increase of air flow rate, and the combustion products were sampled using the diagnostic equipment described in Chapter 2 to determine the CCE and EIs.

Table 3.1: Test matrix of experimental sets performed on a lab-scale air-assisted flare.

Experimental set	Inner Tube OD (mm)	Fuel	Fuel Flow Rate (SLPM)	Assist Config.	Assist Composition
1	12.7	CH_4	20	Inner	100% Air
2	12.7	CH_4	**40**	Inner	100% Air
3	**6.35**	CH_4	20	Inner	100% Air
4	12.7	CH_4	20	Inner	**92% N_2/8% Ar**
5	12.7	CH_4	20	Inner	**85% N_2/10.5% O_2/4.5% Ar**
6	12.7	CH_4	20	Inner	**55% N_2/42% O_2/3% He**
7	12.7	**C_3H_8**	20	Inner	100% Air
8	12.7	CH_4	20	**Outer**	100% Air

The following sections provide an evaluation of the CCE and EI (*i.e.*, EI_{THC}, EI_{CO_2}, EI_{CO}, EI_{NO_x}, and EI_{BC}) results for each experiment and then consideration is given to potential hydrodynamic connection between the demonstrated characteristics. It is important to note that EI_{THC} will be substituted for EI_{CH_4} in all experimental sets except for set 7, in which case it will be denoted as $EI_{C_3H_8}$.

3.2 Characterization of Steady State Burner and Exit Conditions

Through the course of the experiments, temperature measurements of the fuel and assist streams were taken based on the thermocouple arrangement shown in Figure 2.2. The absolute temperature ranges of the fuel and assist streams are summarized in Table 3.2 over the range of air-to-fuel gas MFRs tested for each experiment. Interest in the temperature comes from fixing the mass flow for each experiment, but with changes in temperature comes change in density and velocity at the exit, and subsequently the momentum and buoyancy flux of the streams.

Table 3.2: Temperature range of fuel and assist streams assessed at various axial (*i.e.*, *z*-axis) positions along the burner.

Experimental set	Temperature (°C) [a]					
	Annular (fuel)					Center (assist)
	z = 0 mm	z = −5 mm	z = −10 mm	z = −20 mm	z = −40 mm	z = 0 mm
1	69.4 − 131.0	59.3 − 113.1	50.1 − 90.9	38.8 − 64.5	29.6 − 41.8	25.1 – 35.1
2	69.0 − 101.8	59.7 − 88.9	47.7 − 67.6	37.7 − 49.7	28.5 − 33.3	24.6 – 31.9
3	122.0 − 149.0	104.0 − 129.2	83.1 − 103.4	61.2 − 76.3	29.6 − 34.4	23.6 – 33.1
4	115.9 − 131.4	98.9 − 112.8	79.9 − 91.0	56.6 − 64.2	36.6 − 41.0	25.7 – 36.0
5	105.5 − 129.5	90.1 − 111.7	72.9 − 89.8	52.5 − 63.6	35.0 − 40.9	24.7 – 36.0
6	23.6 − 136.7	23.5 − 121.1	23.6 − 95.7	23.6 − 68.1	23.6 − 43.6	24.3 − 62.0
7	21.7 − 106.6	21.6 − 95.8	21.7 − 75.5	21.6 − 56.9	21.6 − 38.7	23.5 – 34.4
	Annular (assist)					Center (fuel)
8	24.5 – 46.8	24.4 – 40.3	24.3 – 39.0	24.2 – 36.6	24.1 – 32.6	23.2 − 31.5

[a] The lower temperature in each cell of the table for either stream is associated with the highest assist flow rate, and the highest temperature is associated with the no assist case.

The temperature measurements for experimental set 1 are plotted in Figure 3.1a and is representative of the trends exhibited in all the sets, except the

inverse flow configuration in experimental set 8, which is depicted in Figure 3.1b. The tops of the outer and inner tubes were observed to get hot due to their proximity to the diffusion flame as heat is transferred to them by radiation and convection. As demonstrated in Figure 3.1, the temperature rise experienced by a fluid as it approached the burner exit was less pronounced at increased air-to-fuel gas MFR. This can be attributed to convective cooling of the tube walls as the air flow rate was increased. Excessive amounts of assist eventually compromise the stability of the flame. Flame extinction was actually provoked for experimental sets 6, 7, and 8, which explains why the coldest fuel and assist temperatures in these cases were near room temperature (*i.e.*, about 23 °C) at the various axial positions along the burner.

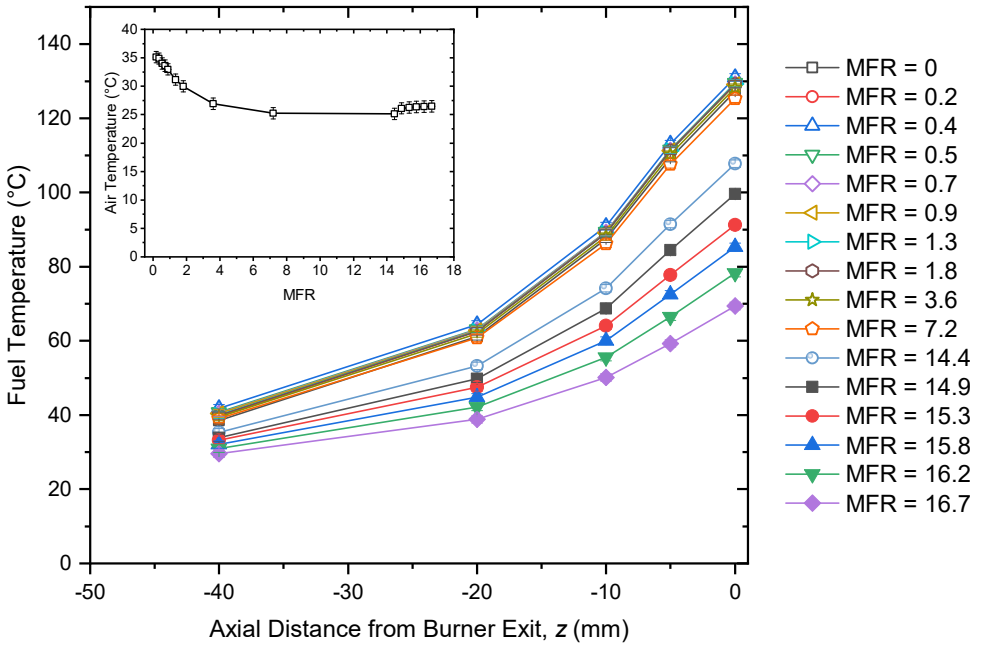

(a)

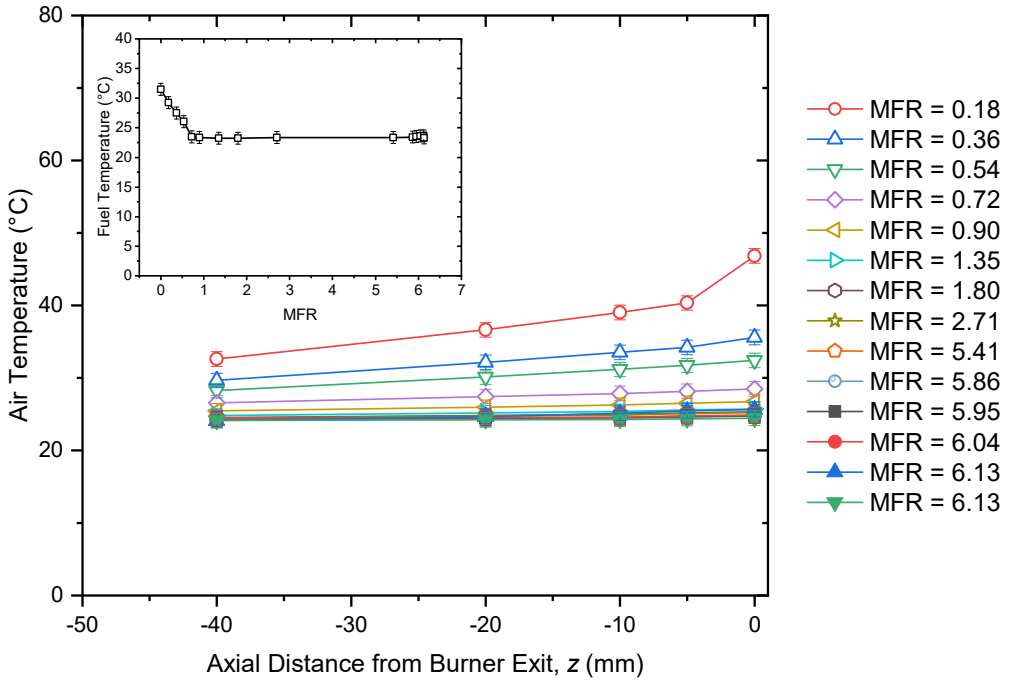

(b)

Figure 3.1: Temperature measurements within the annular flow stream from $z = -40$ mm to $z = 0$ mm with respect to the burner exit plane at increasing air-to-fuel gas MFRs for experimental sets (a) 1 and (b) 8. Each plot also has an inset figure showing the temperature of the internal coflow at the burner exit.

The temperature measurements at the burner exit plane ($z = 0$ mm), along with the pressure measured in the room, were used for determining the density and viscosity of the fuel and air, which in turn were used for calculating various hydrodynamic parameters of the flows, namely, velocity, momentum, and Reynolds number at the burner exit. Table 3.3 summarizes the operating range of each experimental set in terms of air-to-fuel gas MFR and the corresponding parameters. The exit fuel velocity, fuel momentum, and fuel Reynolds number were reported as an average value over the respective MFR range. The equivalence ratio was also evaluated for each experimental set to assess the relative quantity of oxidant available in the assist stream for stoichiometric combustion of the fuel gas.

A characteristic rate at which vertical momentum leaves a tube aligned to the vertical direction can be defined as

$$P_{zz} = \dot{m}_z v_z, \tag{3.1}$$

where $\dot{m}_z$ is the mass flow rate (kg/s) of the fluid and v_z (m/s) is the bulk flow velocity in the z-direction. The bulk flow velocity was calculated by dividing the mass flow rate of the fluid by its respective density and flow area. Note that the actual rate of vertical momentum leaving a circular tube is given by

$$P_{zz} = \int_{r_i}^{r_o} 2\pi r \rho v_z^2 \, dr, \tag{3.2}$$

where r is the radius and the subscripts i and o represent the inner and outer limits for the integration, but this cannot be calculated because the radial dependency of density and velocity is unknown. The Reynolds number and equivalence ratio were calculated as

$$Re = \frac{\rho v_z d_\mathrm{h}}{\mu}, \tag{3.3}$$

$$\phi = \frac{\left(\dot{m}_\mathrm{FG} / \dot{m}_\mathrm{oxygen}\right)_\mathrm{actual}}{\left(\dot{m}_\mathrm{FG} / \dot{m}_\mathrm{oxygen}\right)_\mathrm{stoich}}, \tag{3.4}$$

where ρ (kg/m^3) is density, d_h (m) is the hydraulic diameter, μ (Pa·s) is the dynamic viscosity, and g (m/s^2) is the acceleration due to gravity. It is important to note that $\phi = 1$ indicates there is exactly enough oxygen present in the assist stream for stoichiometric combustion of the fuel. A $1 < \phi < \infty$ indicates that the assist stream cannot supply enough oxygen to fully combust the fuel (*i.e.*, rich fuel-assist mixture), whereas a $0 < \phi < 1$ signifies an excess of oxygen in the assist stream (*i.e.*, lean fuel-assist mixture).

Table 3.3: Exit condition parameters for the corresponding air-to-fuel gas MFR defined for each experimental set. Calculated parameters for the no assist case were not included in the table.

Experimental set	Air-to-Fuel Gas MFR	Velocity (m/s)		Momentum × 10^{-4} (N)		*Re*		ϕ
		Fuel	Assist	Fuel	Assist	Fuel	Assist	
1	0.2 − 16.7	1.7	0.4 − 34.5	3.6	0.2 − 1 261	568	243 − 22 723	94 − 1.0
2	0.1 − 9.0	3.1	0.4 − 37.2	13.5	0.2 − 1 469	1 195	243 − 24 506	190 − 1.9
3	0.2 − 4.7	1.3	1.7 − 42.6	2.9	0.7 − 437	658	540 − 13 980	93 − 3.7
4	0.2 − 9.9	1.7	0.4 − 20.5	3.7	0.1 − 446	553	240 − 13 669	–
5	0.2 − 13.1	1.7	0.4 − 27.1	3.7	0.2 − 774	558	249 − 17 924	191 − 2.6
6	0.2 − 18.9	1.7	0.4 − 39.1	3.6	0.2 − 1 625	572	233 − 25 060	48 − 0.5
7	0.1 − 5.3	1.6	0.4 − 30.7	9.6	0.2 − 1 007	2 176	245 − 20 410	238 − 2.9
8	0.2 − 6.1	3.7	0.1 − 4.3	8.1	0.1 − 58	2 279	73 − 2 605	95 − 2.8

The adiabatic flame temperature was also calculated for each experimental set to provide insight into chemical reaction mechanisms. This was accomplished by using an online STANJAN calculator [48], which computed the equilibrium state of a stoichiometric combustion reaction assuming constant pressure and enthalpy. One of the inputs for the calculation was the starting temperature of the reactants. Since the temperature of the fuel and assist streams differed at the burner exit, an initial equilibrium temperature was calculated for the non-reacting mixture based on representative specific heat capacities, as in

$$T_{eq} = \frac{\sum_k \dot{m}_k \langle c_{p,k} \rangle T_k}{\sum_k \dot{m}_k \langle c_{p,k} \rangle}, \tag{3.5}$$

where $\dot{m}_k$ is the mass flow rate of each component of the mixture, namely, the fuel gas, assist stream and ambient air (just enough air for a stoichiometric flame when CCE = 100% and proportionally less for CCE < 100%), $\langle c_{p,k} \rangle$ (J/kg·K) is the representative specific heat capacity for the temperature of interest, and T_k (K) is the initial temperature of the component. The list of potential product species present at equilibrium were CH_4, CO_2, CO, H, NO, H_2, N, NO_2, O, OH, and H_2O. Ar or He were added to the list for the equivalent assist experiments, and C_2H_6 and C_3H_8 for experimental set 7. The adiabatic flame temperature was plotted for each experimental

set with respect to air-to-fuel gas MFR as shown in Figure 3.2. Refer to Appendix E for more details on the calculation.

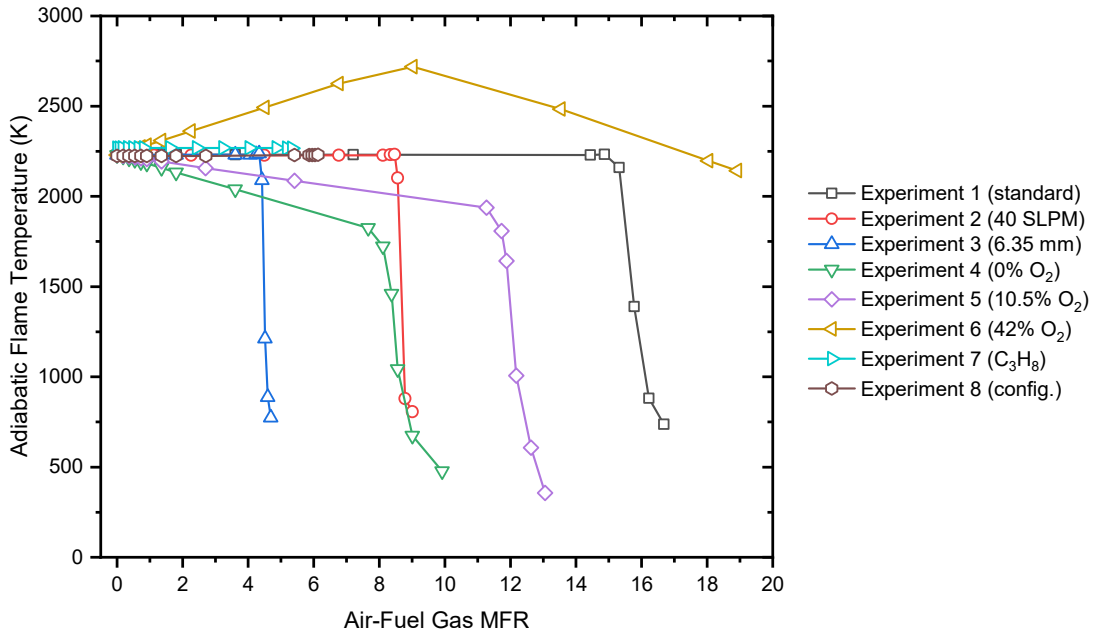

Figure 3.2: Adiabatic flame temperature trends for each experimental set based on STANJAN calculations.

3.3 Experimental Set 1: Combustion of 20 SLPM CH_4 Annular Flow with 100% Air Coflow through 12.7 mm OD Inner Tube

This set of experiment commenced with a 20 SLPM CH_4 jet diffusion flame with no air coflow. At this point, the CCE was essentially 100% as shown in Figure 3.3. Photos of the flame are depicted in Figure 3.4 to illustrate various moments in the experiment. A marginal increase in air-to-fuel gas MFR from zero to 0.2 resulted in a slight increase in EI_{BC} to a maximum of 0.088 g BC/kg fuel, and this was reflected by a highly luminous flame, where the yellow luminosity is associated with thermal radiation from soot particles. EI_{BC} dropped by two orders of magnitude at an air-to-fuel gas MFR of 1.4. At an MFR of 7.2, BC was no longer detected by the current instrument and the flame appeared far less luminous, as shown in Figure 3.4. This transition is attributed to the increased air flow rate giving rise to velocity gradients (*e.g.*, at MFR = 7.2 the bulk velocities of the fuel and assist streams were 1.7 and 14.8 m/s, respectively), thereby promoting a higher degree of fuel-air mixing such

that the oxygen avoids reaction pathways that form soot. EI_{CO_2} and EI_{NO_x} remained relatively constant near a maximum value of 2.7 kg CO_2/kg fuel and 1.21 g NO_x/kg fuel, respectively, although NO_x followed a slight downwards trend starting from an air-to-fuel gas MFR of 3.6.

The flame maintained a high CCE (*i.e.*, $\eta \geq 96.5\%$) until an air-to-fuel gas MFR of 14.9 was approached. With further increasing of air flow rate beyond the onset of collapse in CCE (*i.e.*, MFR > 14.9), the flame exhibited instabilities in what appeared to be localized extinctions, although a stable dome of flame remained fixed to the outer tube of the burner. The collapse in CCE was quite steep, occurring over the last 11% of the air-to-fuel gas MFR. The collapse was accompanied by a steady drop in EI_{CO_2} by 1.5 orders of magnitude and an abrupt drop in EI_{NO_x} by nearly two orders of magnitude. The decrease in NO_x emissions can be associated with reduced temperatures in the combustion zone due to cooling of the fuel stream at increasing MFRs, as demonstrated in Figure 3.1a. It is evident from Figure 3.3 that the EI_{CH_4} plot exhibited the opposite trend as the EI_{CO_2} plot. This is reasonable to expect since flame instabilities would result in less CH_4 oxidizing to CO_2 as the fuel is stripped away from the combustion zone. The fuel-stripping mechanism was instigated by the highly turbulent jet of air assist, which is analogous to a phenomena prevalent in industrial flaring known as over-aeration. EI_{CH_4} was shown to increase by two orders of magnitude to a maximum value of 960 g CH_4/kg fuel coinciding with an air-to-fuel gas MFR of 16.7. It is interesting to note that CO was detected during the collapse in the flame's CCE. A maximum EI_{CO} value of 116 g CO/kg fuel was measured at an air-to-fuel gas MFR of 15.8. The production of CO is a result of incomplete combustion, likely due to the excessively turbulent air stream inhibiting the combustion process. The final photograph in Figure 3.4 represents the last test point corresponding to a CCE of 4.0% and an air-to-fuel gas MFR of 16.7. Though difficult to detect in the photo, direct viewing revealed a dome of flame at the tip of the burner.

The CO_2 equivalent emissions ($EI_{CO_2,eq}$), which is a way of expressing the cumulative effect of the aforementioned emissions into a single metric, was calculated based on a 100-year GWP. The GWP of the individual emissions were taken from the

IPCC [6] and are listed in Table 3.4. $EI_{CO_2,eq}$ was dominated by CO_2 emissions and remained constant until the collapse in CCE, at which point $EI_{CO_2,eq}$ increased drastically to a maximum value of 27 kg CO_2/kg fuel. This is essentially venting of CH_4 which highlights the concern that over-aeration of flares has a direct impact on climate change.

Table 3.4: 100 year GWP of various pollutant emissions and associated uncertainties according to the IPCC.

Species	GWP (100 years)	Error (±)
CH_4	28	8.4
C_3H_8	3.3	3.3
CO_2	1	0
CO	1.8	0.6
NO_x	−8.2	10.3
BC	900	800

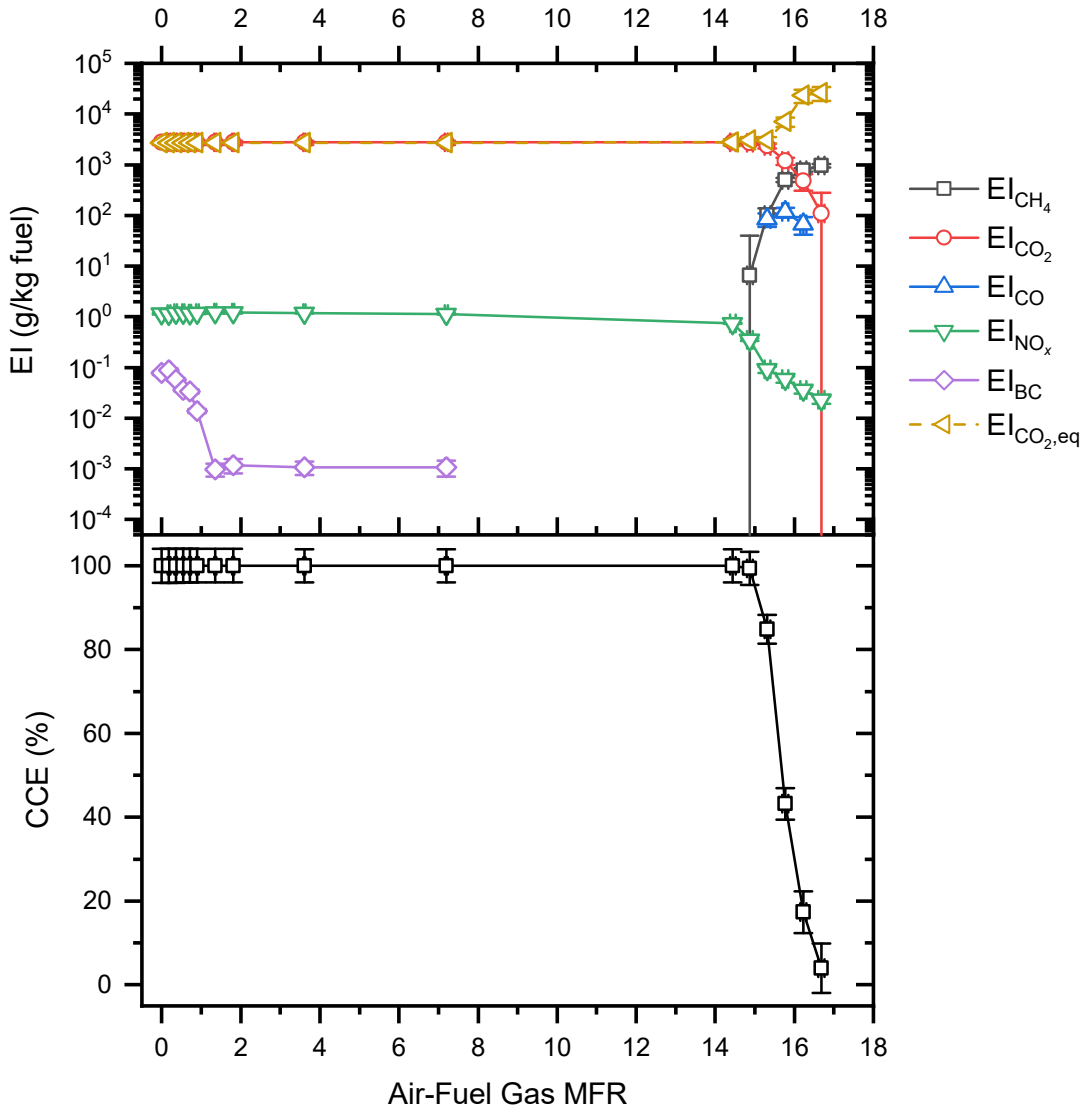

Figure 3.3: Results of experimental set 1 - CCE (bottom), EI (top).

MFR = 0	MFR = 7.2	MFR = 14.9	MFR = 15.8	MFR = 16.7
η = 100%	η = 100%	η = 99.3%	η = 43.2%	η = 4.0%

Figure 3.4: Photos of the flame taken during experimental set 1 at increasing air-to-fuel gas MFRs.

3.4 Experimental Set 2: Combustion of 40 SLPM CH_4 Annular Flow with 100% Air Coflow through 12.7 mm OD Inner Tube

Experimental set 2 replicated the test configuration used in experimental set 1, except that the flow rate of CH_4 was doubled from 20 SLPM to 40 SLPM (the mass flow rate also doubled since the flow controller is corrected to standard conditions). The trends in CCE and EIs are displayed in Figure 3.5. The flame was initially luminous with a maximum EI_{BC} of 0.005 g BC/kg fuel at zero air coflow. It is interesting to note that this value is about 1.5 orders of magnitude less than the BC generated in experimental set 1 at zero air coflow. A reasonable explanation for this difference is that the fuel exit Reynolds number in experimental set 2 doubled to 1 195 from 568 in experimental set 1, as outlined in Table 3.3, which suggests that the mixing of fuel with ambient air was occurring to a greater extent, thereby driving the combustion reaction towards completion. EI_{BC} dropped by 1.5 orders of magnitude at an air-to-fuel gas MFR of 0.5. EI_{CO_2} and EI_{NO_x} remained relatively constant near a maximum value of 2.74 kg CO_2/kg fuel and 0.90 g NO_x/kg fuel, respectively.

The flame sustained a CCE ≥ 96.5% up to an air-to-fuel gas MFR of 8.5, after which the CCE dropped steeply. The onset of collapse in CCE occurred at about half

the air-to-fuel gas MFR compared to experimental set 1. It was originally thought that an increased fuel flow rate would generate more robust combustion demanding of proportionately higher air assist to destabilize it. On further consideration, however, there is an argument that a high velocity fuel stream would induce greater entrainment of ambient air into the combustion zone through turbulent mixing. As such, comparatively less air assist would be required to trigger a collapse in CCE. The collapse was marked by flame instabilities similar to those observed in experimental set 1. A maximum EI_{CO} of 40 g CO/kg fuel was measured at an air-to-fuel gas MFR of 8.6. This is about one-third of the value measured in experimental set 1, likely resulting from a higher exit fuel velocity promoting better fuel-air mixing in the combustion zone. EI_{CH_4} was shown to increase by three orders of magnitude to a maximum value of 922 g CH_4/kg fuel coinciding with an air-to-fuel gas MFR of 9.0. The $EI_{CO_2,eq}$ plot in Figure 3.5 shows a similar trend to that from experimental set 1. A maximum value of 26 kg CO_2/kg fuel was calculated, which is the same as experimental set 1 since these both represent the venting of CH_4.

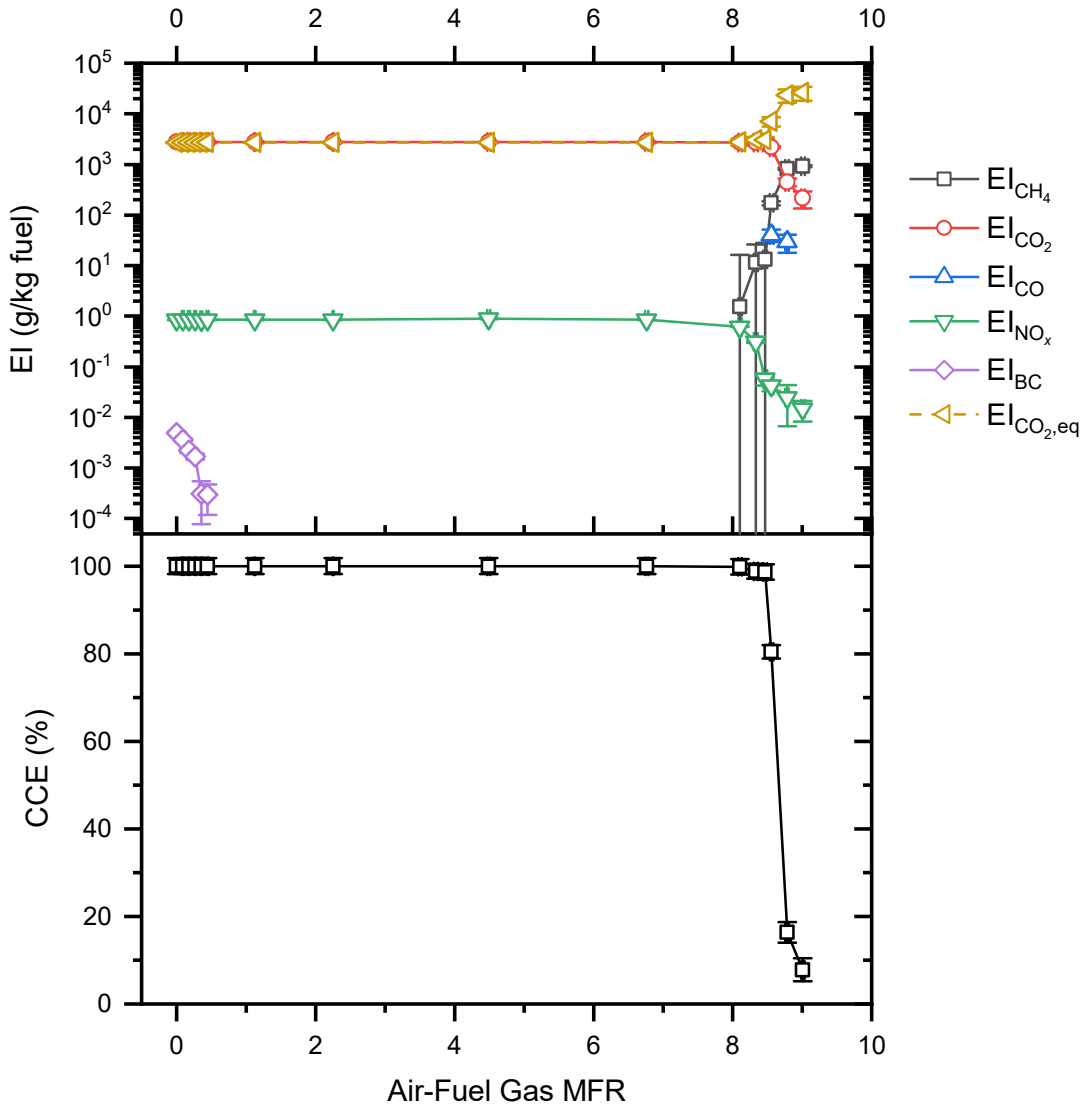

Figure 3.5: Results of experimental set 2 - CCE (bottom), EI (top).

3.5 Experimental Set 3: Combustion of 20 SLPM CH_4 Annular Flow with 100% Air Coflow through 6.35 mm OD Inner Tube

Experimental set 3 replicated the test configuration used in experimental set 1, except that the air coflow was injected through an inner tube with half the diameter. This allowed for investigating the impact of increasing the exit Reynolds number of the air coflow relative to the fuel. The trends in CCE and EIs are displayed in Figure 3.6. The maximum EI_{BC} was measured to be 0.152 g BC/kg fuel at zero air coflow, which is an increase by a factor of 1.7 compared to the corresponding point in experimental set 1. This change can be accounted for by a decrease in the exit fuel velocity and

momentum, which correlates to less entrainment of ambient air. EI_{BC} dropped by about two orders of magnitude at an air-to-fuel gas MFR of 0.5. EI_{NO_x} rose to a maximum of 1.38 g NO_x/kg fuel over the same MFR. This value is 14% higher than experimental set 1. A possible explanation is elevated temperatures in the combustion zone which would be conducive to thermal NO_x formation (high temperature oxidation of N_2). However, the adiabatic flame temperature plots in Figure 3.2 show that experimental sets 1 and 3 share a maximum temperature of about 2 230 K. It is therefore likely that better mixing in the present case is yielding higher NO_x formation rates.

The CCE plot shows that the flame maintained a CCE ≥ 96.5% up to an air-to-fuel gas MFR of 4.2. The collapse in CCE was triggered even earlier than experimental set 2. It can be argued that a smaller inner tube diameter resulted in a higher velocity and momentum gradient between the air and fuel streams (*e.g.*, at MFR = 4.7 the air-to-fuel gas velocity and momentum gradients were 34 and 157, respectively), prompting flame instability and initiating the fuel-stripping mechanism. Another consequence of the high velocity gradient is the absence of CO measurements in this experiment, in which the fuel was sufficiently mixed with combustion air, thereby eliminating incomplete products of combustion. Lastly, a maximum EI_{CH_4} of 944 g CH_4/kg fuel and an $EI_{CO_2,eq}$ of 27 kg CO_2/kg fuel indicated venting of CH_4 at an air-to-fuel gas MFR of 4.7.

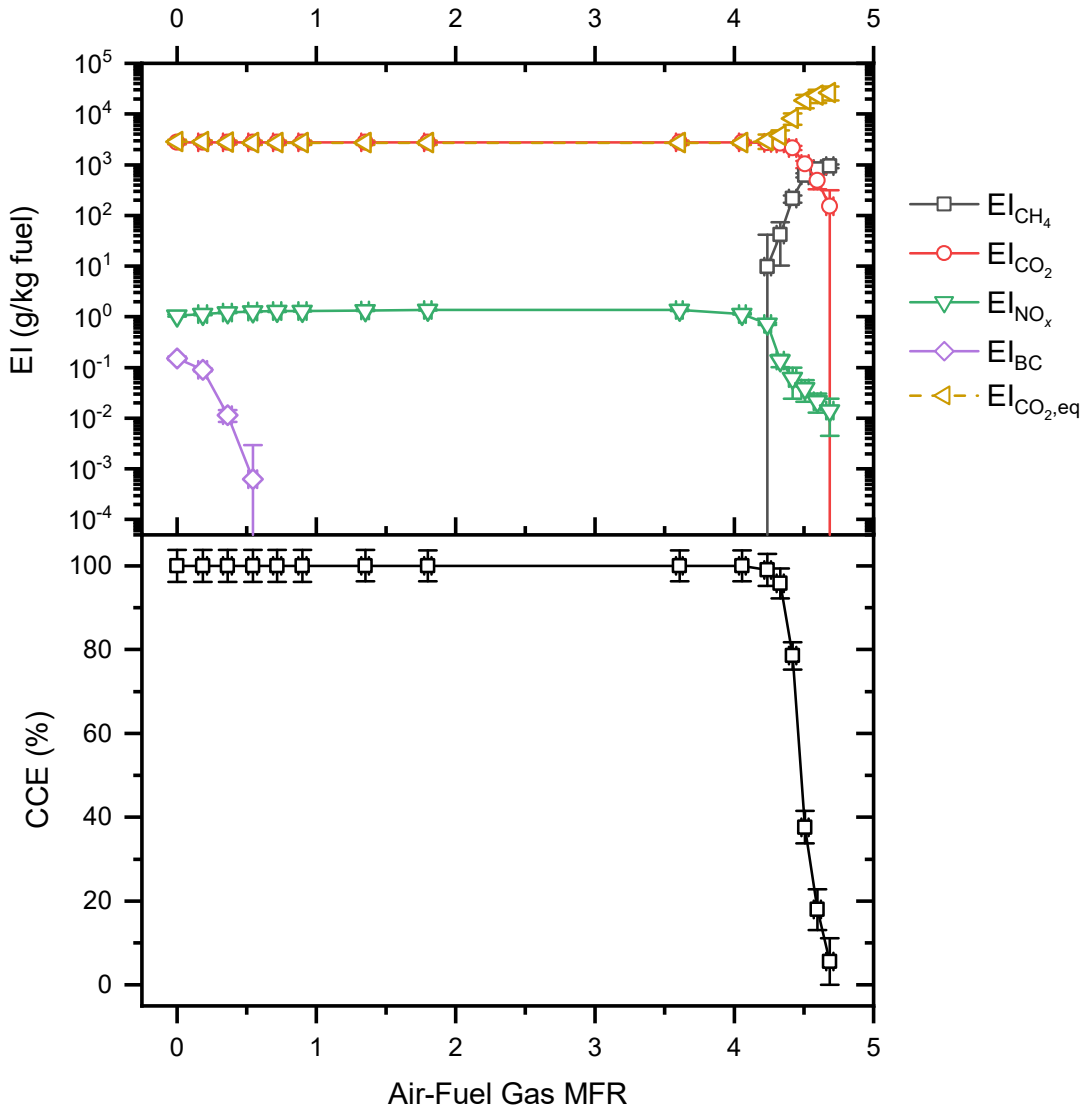

Figure 3.6: Results of experimental set 3 - CCE (bottom), EI (top).

3.6 Experimental Set 4: Combustion of 20 SLPM CH_4 Annular Flow with 92% N_2/8% Ar Coflow through 12.7 mm OD Inner Tube

Experimental set 4 is the first of three sets that replaced air assist with a so-called equivalent air assist meant to replicate the hydrodynamic characteristics of air. A mixture consisting of 92% N_2 and 8% Ar by volume was used as the assist media. Inert gases were deliberately used in this experiment to investigate the relative effect of O_2 on CCE and EI. The CCE and EI plots are displayed in Figure 3.7. The EI_{BC} trend behaved similarly to experimental set 1. A maximum of 0.120 g BC/kg fuel was measured at a marginal equivalent air-to-fuel gas MFR of 0.2. BC emissions were

effectively eliminated at an equivalent air-to-fuel gas MFR of 1.4, although trace amounts were observed to reappear. EI_{NO_x} was measured at a maximum value of 1.18 g NO_x/kg fuel corresponding to zero coflow. It was interesting to note, however, that NO_x emissions exhibited a steady decline starting from an equivalent air-to-fuel gas MFR of 1.8, as opposed to remaining constant until the collapse in CCE as was evident in experimental sets 1 to 3. The thermal NO_x mechanism relies on the presence of high temperatures, O_2, and N_2. Figure 3.2 shows the adiabatic flame temperatures dropping steadily, likely due to more diluents in the products, which corroborates the NO_x trend. Another factor is the reduced availability of O_2. N_2 is present everywhere and unchanging.

The flame sustained a CCE ≥ 96.5% up to an equivalent air-to-fuel gas MFR of 7.7. The flame appeared to be a dimmer shade of blue than the flame shown in Figure 3.4. The collapse in CCE was more gradual as compared to the previous experiments (occurring over the last 23% of the equivalent air-to-fuel gas MFR). Trace amounts of BC were detected at the onset of fuel-stripping, which was unique to this experimental set. It is likely a result of fuel-rich conditions in the combustion zone due to excessive dilution by the inert coflow stream. A maximum EI_{CO} of 142 g CO/kg fuel was measured at an equivalent air-to-fuel gas MFR of 8.6. This is 22% more than was measured in experimental set 1. The increase in CO can be accounted for by the absence of O_2 in the coflow stream resulting in reduced formation of complete products of combustion.

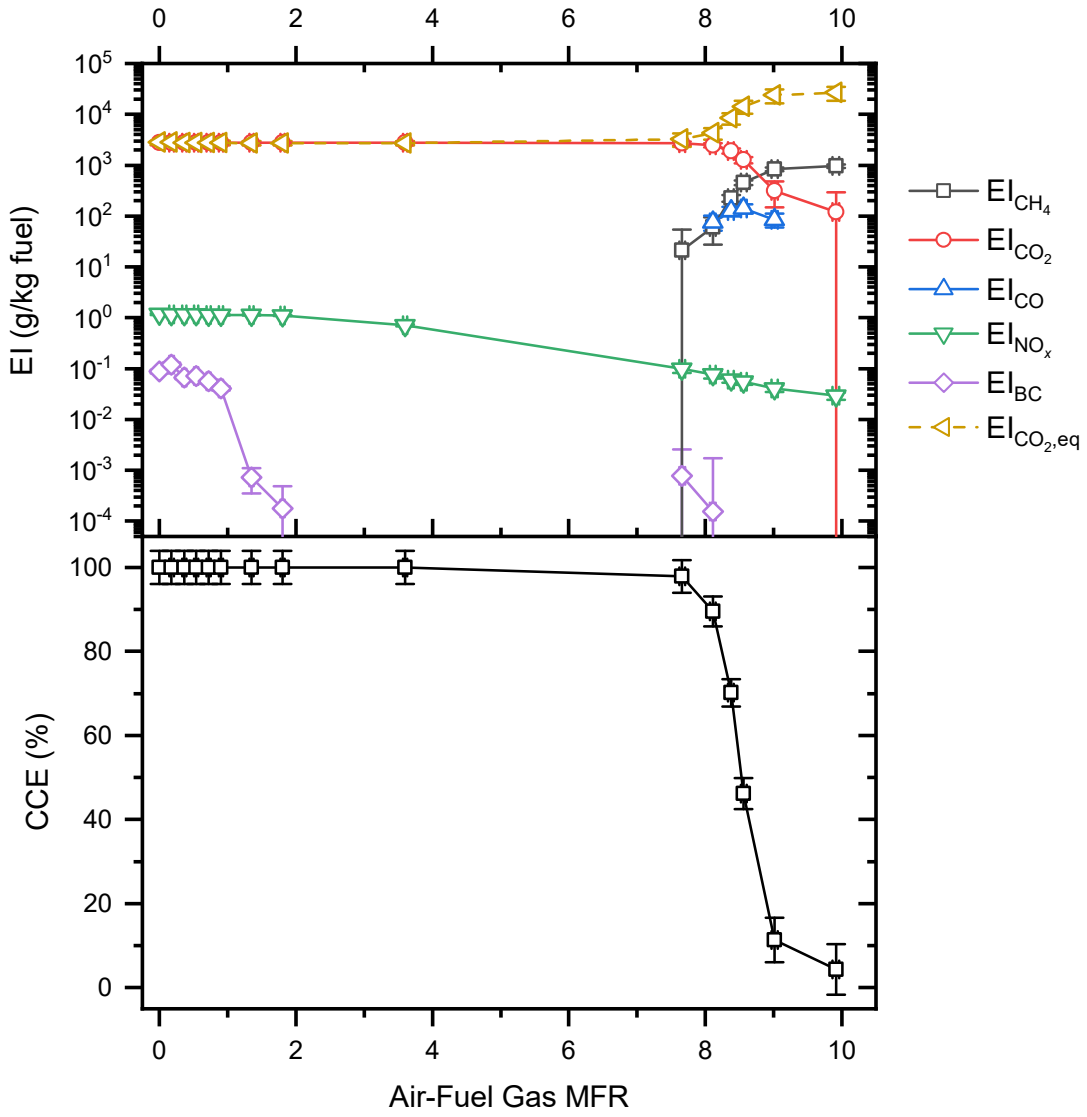

Figure 3.7: Results of experimental set 4 - CCE (bottom), EI (top).

3.7 Experimental Set 5: Combustion of 20 SLPM CH_4 Annual Flow with 85% N_2/10.5% O_2/4.5% Ar Coflow through 12.7 mm OD Inner Tube

In experimental set 5, the equivalent air assist mixture was modified to include 10.5% O_2 to study the effect of injecting assist fluid with half the oxidizing potential of air, but equal hydrodynamics. The CCE and EI plots are presented in Figure 3.8. A maximum EI_{BC} of 0.100 g BC/kg fuel was measured at an equivalent air-to-fuel gas MFR of 0.2, which is an average of the maximum EI_{BC} values reported for

experimental sets 1 and 4 at the same MFR. BC was no longer detected by the PAX at an MFR of 1.4. The EI_{NO_x} trend was reminiscent of experimental set 4, in that a steady decline was initiated relatively early, at an equivalent air-to-fuel gas MFR of 2.7. The onset of collapse in CCE was at an equivalent air-to-fuel gas MFR of 11.3, which is exactly the average of experimental sets 1 and 4, and spanned over the last 14% of the MFR range. A maximum EI_{CO} of 126 g CO/kg fuel was measured at an equivalent air-to-fuel gas MFR of 12.2, which is nearly the average of the maximum EI_{CO} recorded for experimental sets 1 and 4. This validates the notion that the collapse in CCE and the products of incomplete combustion (*i.e.*, BC and CO) responded linearly with respect to an increase in O_2 from 0% in experimental set 4, to 10.5%, and then to 21% in experimental set 1.

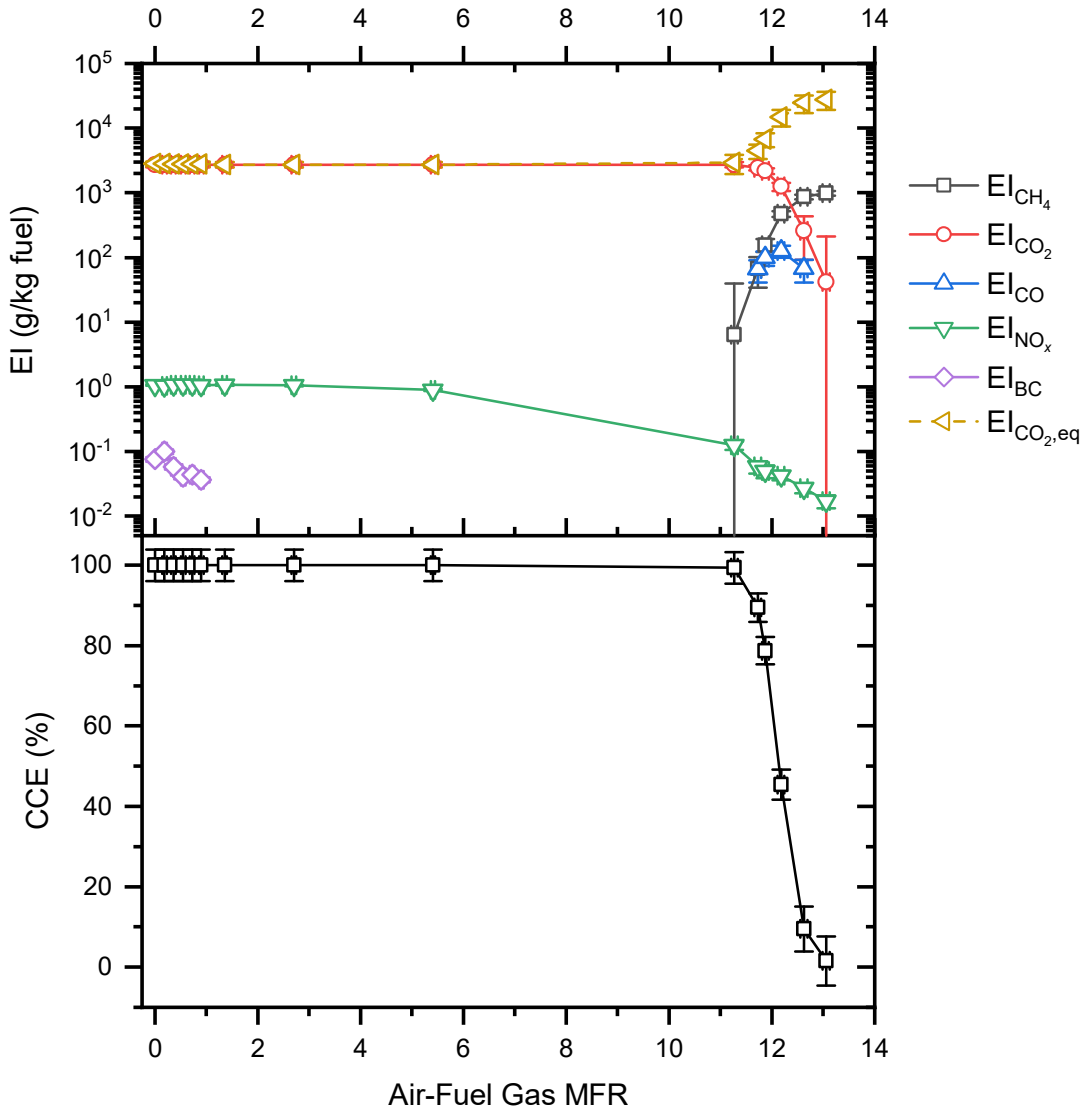

Figure 3.8: Results of experimental set 5 - CCE (bottom), EI (top).

3.8 Experimental Set 6: Combustion of 20 SLPM CH_4 Annular Flow with 55% N_2/42% O_2/3% He Coflow through 12.7 mm OD Inner Tube

The third equivalent air assist mixture consisted of 42% O_2 by volume, which is twice the O_2 content in ambient air. The objective of this experimental set was to assess the flame's response to the doubling of O_2. The CCE, EI, and $EI_{CO_2,eq}$ plots are presented in Figure 3.9. Photos of the flame were taken at specified test points as indicated in Figure 3.10. As observed in experimental sets 1, 4 and 5, a nominal increase in

equivalent air-to-fuel gas MFR from zero to 0.2 resulted in a slight increase in EI_{BC} to a maximum of 0.069 g BC/kg fuel. EI_{BC} dropped by nearly an order of magnitude corresponding to an equivalent air-to-fuel gas MFR of 0.5. This MFR coincided with the sudden ignition of an inner flame stabilized at the tip of the inner tube, as depicted in Figure 3.10. EI_{BC} rose to a new maximum of 0.046 g BC/kg fuel at an equivalent air-to-fuel gas MFR of 2.3, which corresponded to the highly luminous flame shown in Figure 3.10. A remarkable finding from this experiment was the unprecedented level of NO_x. Whereas EI_{NO_x} was measured at a maximum at the onset of the previous experimental sets, the initial EI_{NO_x} measurement in the present case was a minimum, which steadily rose by over two orders of magnitude to a maximum value of 290 g NO_x/kg fuel at an equivalent air-to-fuel gas MFR of 9.0. It is interesting to note that the adiabatic flame temperature also rose to a maximum of 2 719 K at the same MFR of 9.0, as shown in Figure 3.2. This confirms that the flame temperature plays a dominating role in the formation of NO_x. The abundance of O_2 in the assist stream is also a contributing factor. An MFR of 9.0 coincided with $\phi = 1$, which indicated that enough O_2 was present in the assist stream for stoichiometric combustion of the fuel. Further increase of assist flow rate yielded diminishing NO_x levels, which was reflected by the downward trend of the adiabatic flame temperature as well as $0 < \phi < 1$ (*i.e.*, lean fuel-assist mixture).

Another interesting result from this experimental set was the nature of the collapse in CCE. The flame sustained a CCE of 100% over an exceptionally high air-to-fuel gas MFR of 18.9 before extinguishing abruptly, resulting in a step drop in CCE to 0%. A photo of the flame immediately before extinguishing is shown in Figure 3.10. The exceedingly high momentum of the assist stream gave rise to instabilities in the form of localized extinction of the flame at its base, before eventually extinguishing the flame altogether. Trace amounts of unburned CH_4 was detected at an equivalent air-to-fuel gas MFR of 18.0, which marked the onset of fuel-stripping. No CO was detected in this experimental set, which is understandable given the high O_2 content of the assist stream promoting complete combustion. The final point of interest is the $EI_{CO_2,eq}$ plot, which differed considerably from the previous ones. As shown in Figure 3.9, $EI_{CO_2,eq}$ decreased in conjunction with an increase in NO_x. This

can be explained by the fact that NO_x has a GWP of −8.2, which brought the overall $EI_{CO_2,eq}$ down.

Results from the equivalent assist experiments revealed that the chemical aspect of the combustion was as much a factor in interpreting the trends in CCE and EIs as were the hydrodynamic characteristics of the fluids. This notion is demonstrated by the fact that a change in the O_2 content of the assist stream provoked a nearly linear response with respect to the characteristic point of collapse in CCE (*i.e.*, CCE = 96.5%). As shown in Figure 3.11, the O_2 content in the assist streams for experimental sets 1, 4, 5, and 6 (21%, 0%, 10.5%, and 42%, respectively) are plotted against their respective air-to-fuel gas MFRs marking the onset of CCE collapse. The utility of this plot is its potential to predict the collapse in CCE of a flare based on the O_2 mole fraction of the equivalent assist mixture.

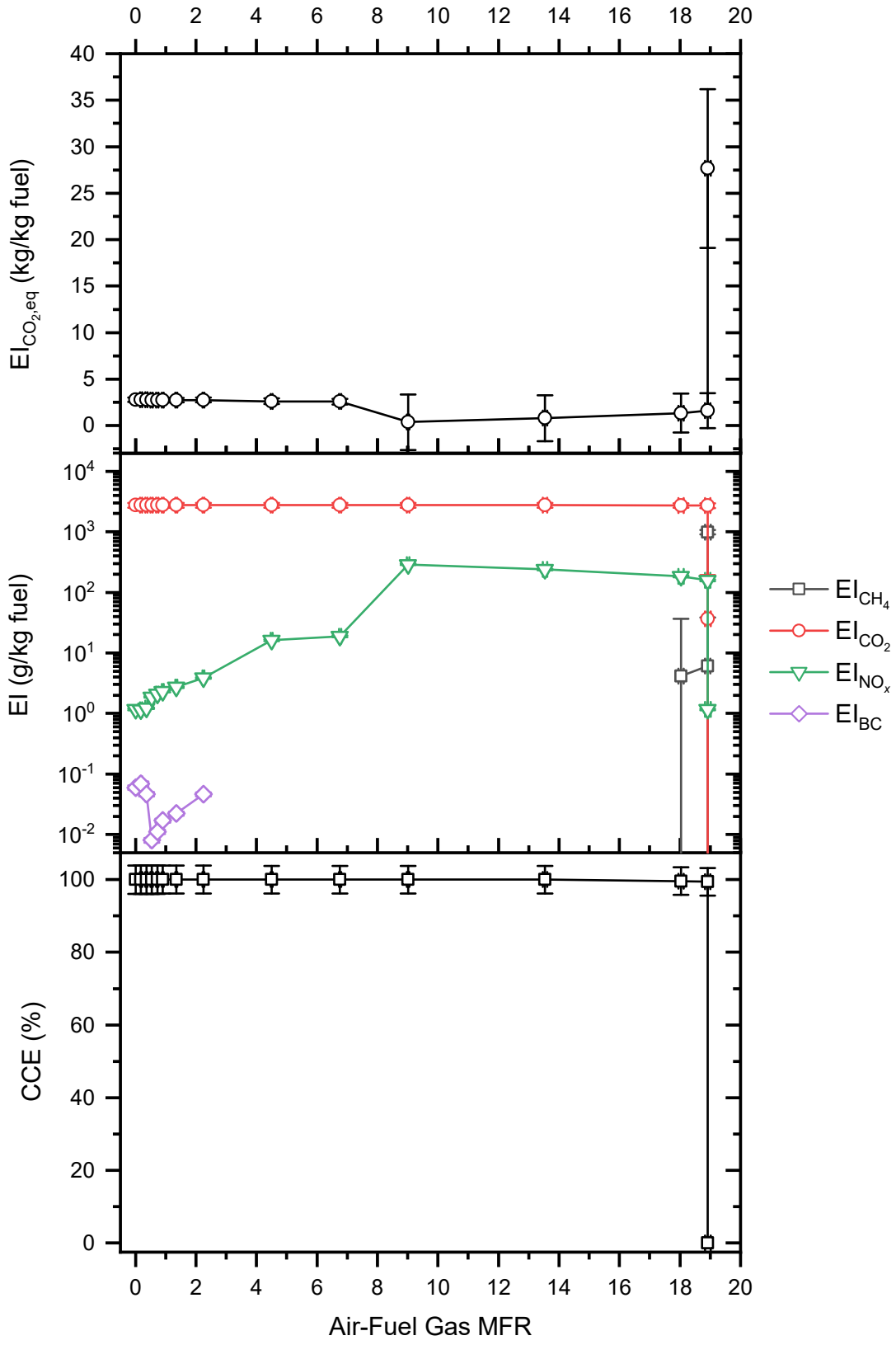

Figure 3.9: Results of experimental set 6 - CCE (bottom), EI (center), $EI_{CO2,eq}$ (top).

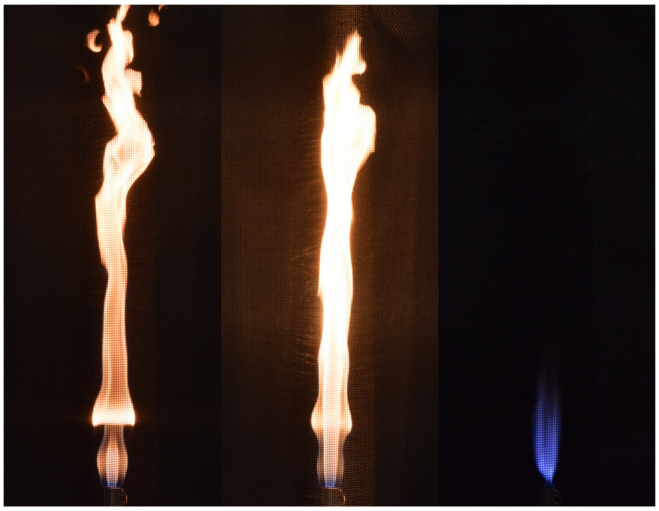

Figure 3.10: Photos of the flame taken during experimental set 6 at increasing equivalent air-to-fuel gas MFRs.

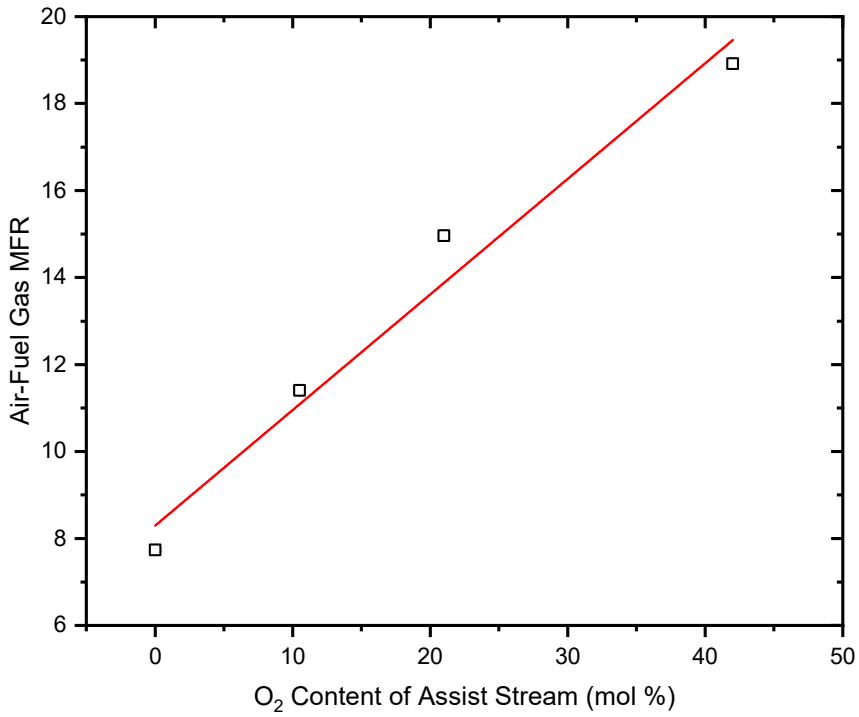

Figure 3.11: O_2 content in the assist stream for experimental sets 1, 4, 5, and 6 plotted as a function of the equivalent air-to-fuel gas MFR marking the onset of CCE collapse. The MFRs were interpolated at a CCE = 96.5%.

3.9 Experimental Set 7: Combustion of 20 SLPM C_3H_8 Annular Flow with 100% Air Coflow through 12.7 mm OD Inner Tube

Experimental set 7 replicated the test configuration used in experimental set 1, except that CH_4 was replaced with C_3H_8, but dispensed at the same flow rate of 20 SLPM. The objective was to investigate the effect of increasing the LHV of the fuel gas from 32.8 MJ/m^3 to 84.9 MJ/m^3, as well as the effects of having a fuel with a greater proportion of carbon. A C_3H_8 flame is considerably larger than a CH_4 flame since it requires 2.5 times more air per mole of fuel to fully react. The trends in CCE and EIs are displayed in Figure 3.12. Photos representative of critical stages in the experiment are depicted in Figure 3.13. At zero air coflow the flame was highly luminous, as shown in Figure 3.13, corresponding to a maximum EI_{BC} of 2.586 g BC/kg fuel (29 times greater than experimental set 1). EI_{BC} dropped steadily by about 1.5 orders of magnitude with increasing air flow. EI_{NO_x} rose gradually to a maximum of 0.97 g NO_x/kg fuel (20% less than experimental set 1) at an air-to-fuel gas MFR of 4.0. The corresponding photo of the flame is illustrated in Figure 3.13, which shows a far less luminous flame.

The flame developed localized extinction near the base of the flame as shown in Figure 3.13, before extinguishing abruptly at an air-to-fuel gas MFR of 5.3. This is represented in the CCE plot as a step drop in efficiency to 0%. It is interesting to note that the present case exhibited a collapse in CCE relatively early. In fact, the maximum air flow rate sustained by the C_3H_8 flame was only 195 g/min, whereas the CH_4 flame in experimental set 1 sustained 219 g/min (CCE = 4%). A differentiating factor, however, was that the C_3H_8 fuel jet had an exit Reynolds number of 2 166, nearly four times higher than CH_4 (with a Reynolds number of 567). As such, the C_3H_8 flame entrained greater volumes of ambient air for combustion and required comparatively less assist air to trigger flame instability. A consequence of this phenomena was that no CO was detected, since the collapse in CCE was abrupt and there was no opportunity for incomplete combustion to take place. $EI_{CO_2,eq}$ was measured at a maximum of 5.31 kg CO_2/kg fuel at zero coflow, and steadily declined in conjunction with BC emissions. The C_3H_8 GWP for a span of 100 years was reported as 3.3 by the IPCC [6], considerably less than CH_4. From an industrial flare

operating standpoint, an ideal range in air-to-fuel gas MFR is defined as one that yields a CCE ≥ 96.5% and minimum pollutant emissions. This range was identified for the present experimental set as starting from an air-to-fuel gas MFR of 1.6, which coincided with the minimum $EI_{CO_2,eq}$, up to the collapse in CCE.

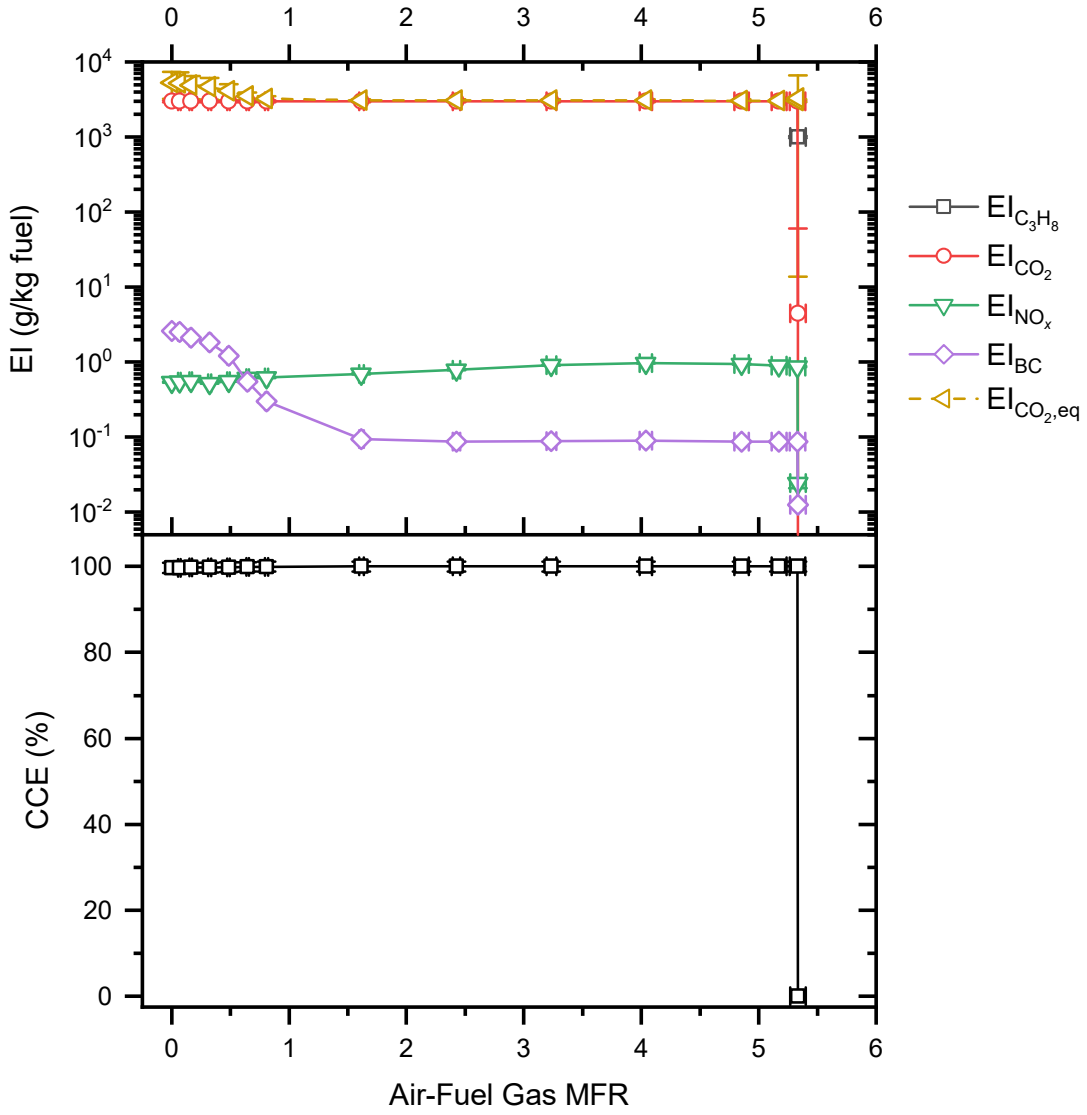

Figure 3.12: Results of experimental set 7 - CCE (bottom), EI (top).

Figure 3.13: Photos of the flame taken during experimental set 7 at increasing air-to-fuel gas MFRs.

3.10 Experimental Set 8: Combustion of 20 SLPM CH_4 Inner Flow through 12.7 mm OD Tube with 100% Air Annular Coflow

Experimental set 8 switched the flow configuration used in experimental set 1, in that 20 SLPM of CH_4 flowed through the inner tube while air coflow was injected through the annular space between the outer and inner tubes. The objective was to study the effect that an external jet of air would have on flame characteristics. The trends in CCE and EIs are displayed in Figure 3.14. Photos were taken at key stages in the experiment and are shown in Figure 3.15. The unassisted flame, as depicted in Figure 3.15, yielded 0.001 g BC/kg fuel which increased to a maximum of 0.002 g BC/kg fuel at an air-to-fuel gas MFR of 0.2. The maximum BC generated was the least of all experimental sets. The most likely explanation is that the fuel exit Reynolds number was the highest, at 2 278, which is four times the fuel Reynolds number in experimental set 1, as specified in Table 3.3. This amplified the entrainment of ambient air into the fuel stream, thereby driving the combustion reaction towards completion.

The most significant observation was flame lift-off, which was unique to this experimental set. At an air-to-fuel gas MFR of 0.7, the flame appeared to lift off the burner exit, its base stabilizing at a height of about 3.4 cm above the burner exit (or 1.3 diameters of the outer tube) as shown in Figure 3.15. A maximum EI_{NO_x} of 1.15 g NO_x/kg fuel was measured at an air-to-fuel gas MFR of 0.9, after which it exhibited a steady decline. Unburned CH_4 was first detected at an air-to-fuel gas MFR of 5.4, marking the onset of the fuel-stripping mechanism. As EI_{CH_4} increased, the CCE decreased to 95.8% at an MFR of 6.1 before abruptly dropping in a step-like fashion to 0%. Figure 3.15 shows the final photo taken of the flame before extinguishing. Its base was lifted to a height of about 18.3 cm above the burner exit (or 7.2 diameters of the outer tube). It can be concluded from this experimental set that the outer air coflow configuration was conducive to flame instability in the form of flame lift-off, which gave rise to an early collapse in CCE.

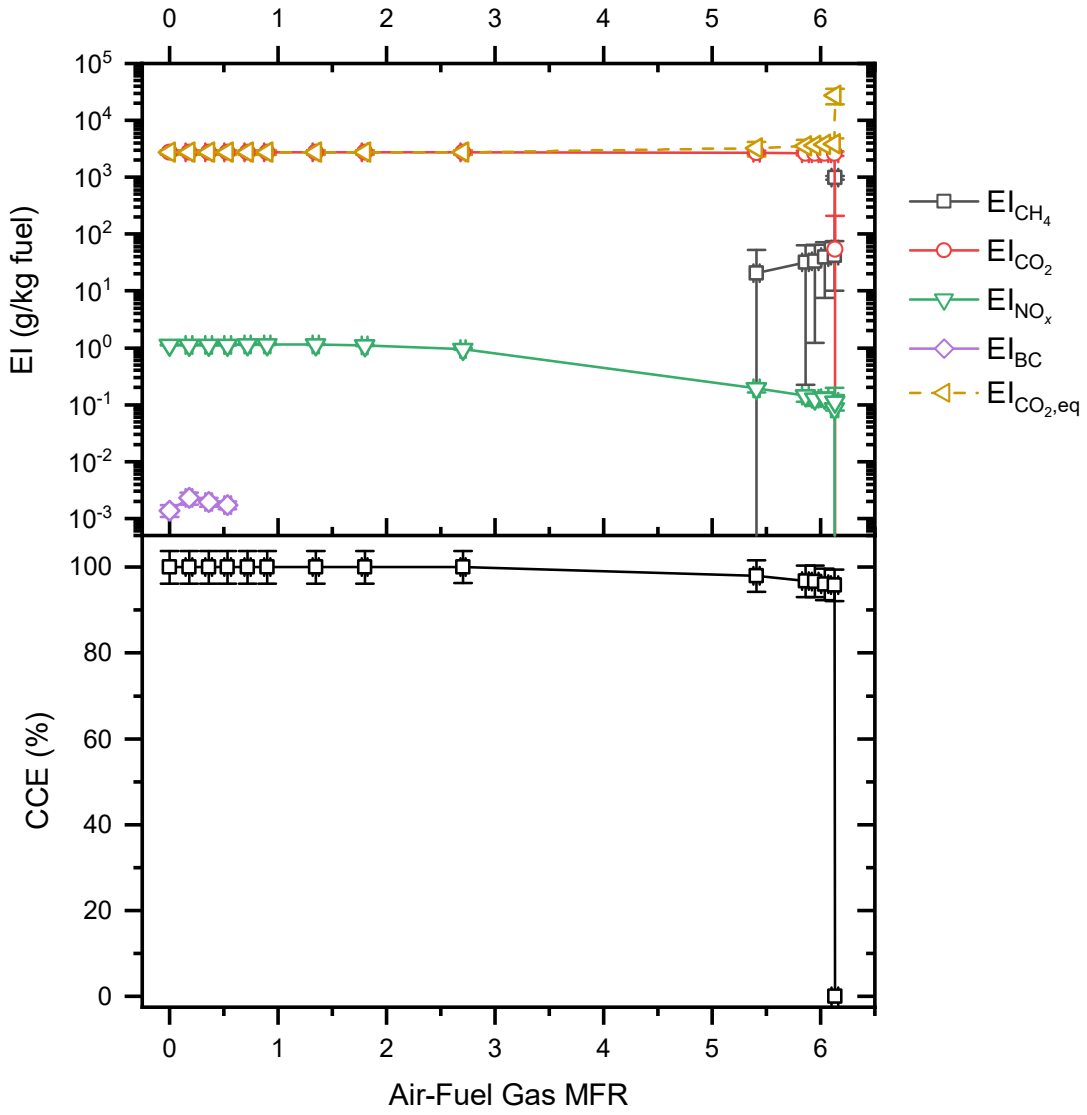

Figure 3.14: Results of experimental set 8 - CCE (bottom), EI (top).

Figure 3.15: Photos of the flame taken during experimental set 8 at increasing air-to-fuel gas MFRs.

3.11 Analysis of Results with Respect to Exit Hydrodynamics

An attempt was made to identify a unifying trend that described the experimental results based on non-dimensional hydrodynamic parameters. Besides the air-to-fuel gas MFR (which was selected as the standard metric by which to plot CCE and EIs because it was the mass flow rates that were controlled, and relevance to industrial-scale flare studies), the air-to-fuel gas velocity ratio (VR_{zz}) both in the z-direction and the air-to-fuel gas momentum ratio (MR_{zz}) both in the z-direction were considered in order to assess their potential for consolidating the data sets (*i.e.*, the CCE plots). The VR_{zz} was calculated using the vertical bulk flow velocity of air and fuel evaluated at the burner exit plane. The MR_{zz} was simply the product of MFR and VR_{zz}. Figure 3.16 shows the CCE trends of each experimental set with respect to the air-to-fuel gas MFR. The air-to-fuel gas VR and the air-to-fuel gas MR are presented in Figure 3.17 and Figure 3.18, respectively. Note that experimental set 8 was omitted from the analysis due to its distinct flow geometry.

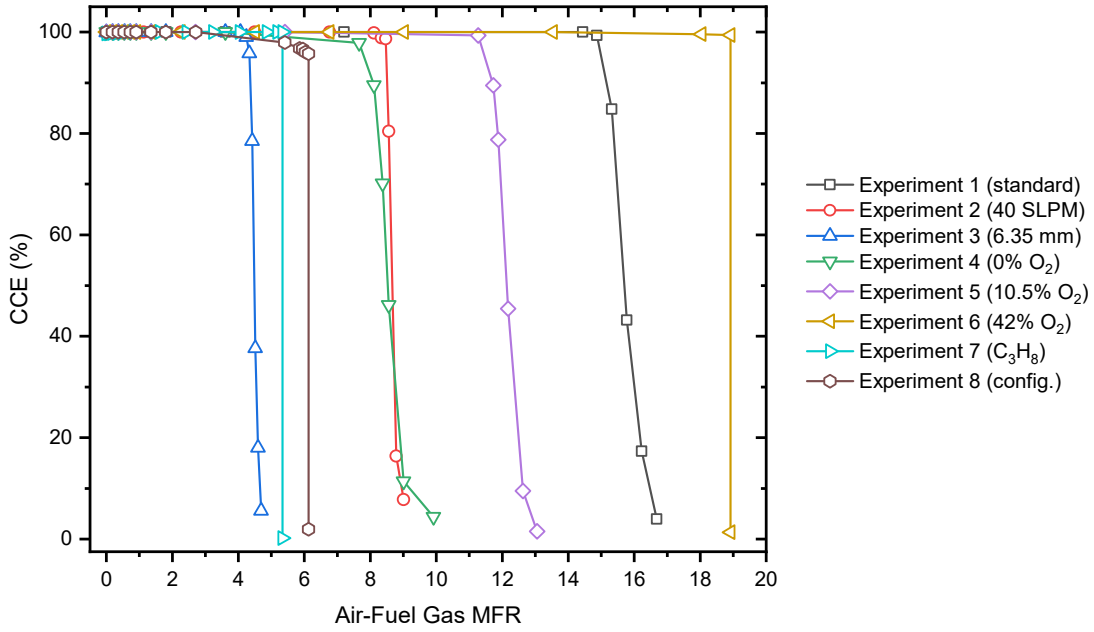

Figure 3.16: CCE plotted as a function of the air-to-fuel gas MFR.

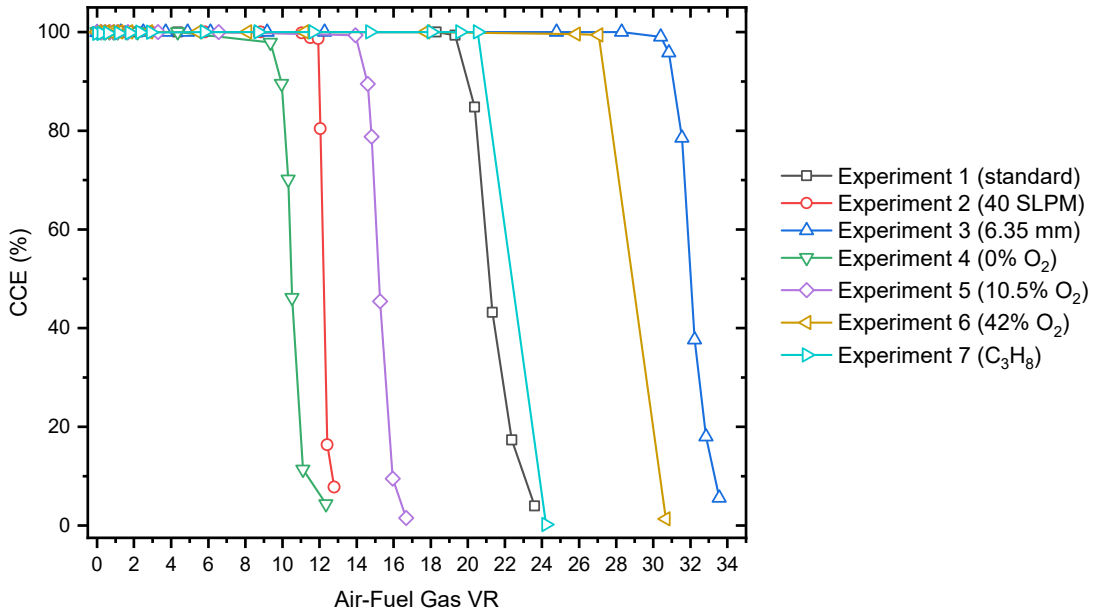

Figure 3.17: CCE plotted as a function of the air-to-fuel gas VR.

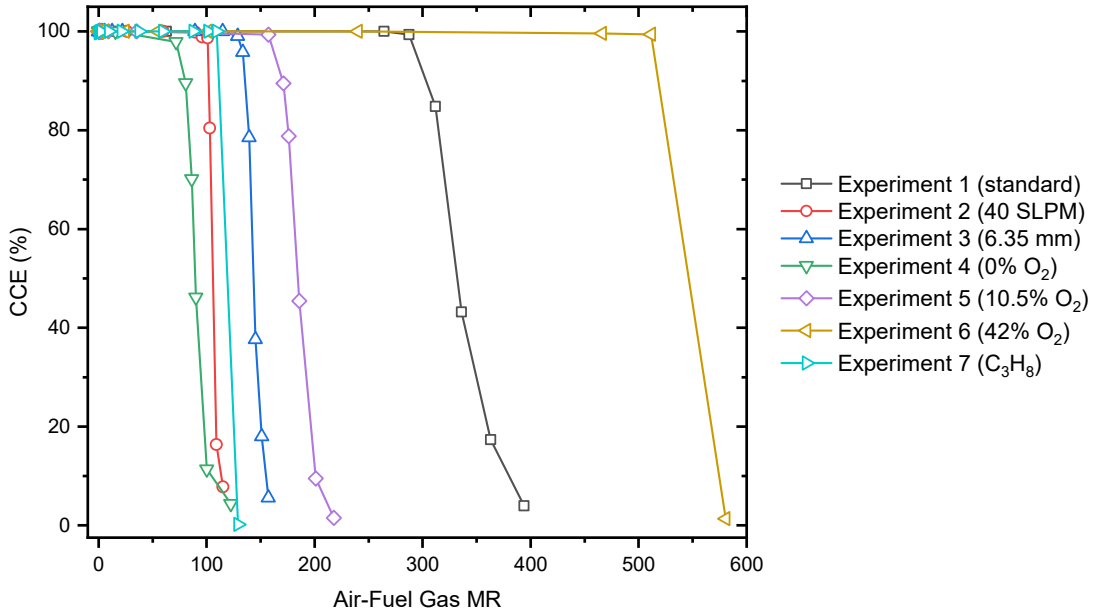

Figure 3.18: CCE plotted as a function of the air-to-fuel gas MR.

As is evident from the figures above, the VR and MR did not manage to consolidate the CCE plots into a single trend. This may suggest that the results are not exclusively dictated by the exit hydrodynamic characteristics of the fluids. Other factors may influence the trends exhibited in the figures. For instance, chemical effects in the form of mole fraction of O_2 in the assist fluid provoked a linear response in terms of the onset of CCE collapse for experimental sets 1, 4, 5, and 6, as demonstrated in Figure 3.11.

However, the figures are useful for demonstrating which experimental sets (and their respective burner configurations) are conducive to high or low gradients in mass, velocity, and momentum. For instance, experimental set 3 showed that a burner with an inner tube OD of 6.35 mm sustained a flame up to an air-to-fuel gas VR 1.6 times greater than the standard case. Conversely, the same experimental set compromised the flame's air-to-fuel gas MR by a factor of 2.2 relative to the standard case.

3.12 Comparison with Industrial-Scale Flare Studies

Results of the CCE and EI analysis are summarized in Table 3.5. The air-to-fuel gas MFRs marked the onset of collapse in CCE below 96.5%, which is the

threshold defined by US federal regulations for optimally operated flares. The maximum measured EIs were reported for a CCE ≥ 96.5% to establish the acceptable limit within the framework of industrial flare operations. A significant trend that was observed for each experimental set, with the exception of the sixth set, was that an increase in the air-to-fuel gas MFR from zero to two yielded a drop in BC emissions by at least one order of magnitude. From a flare operation standpoint, this would be equivalent to the minimum allowable set point.

Table 3.5: Maximum EIs of various pollutant emissions generated by a lab-scale air-assisted flare evaluated at a CCE ≥ 96.5%. The air-to-fuel gas MFRs were interpolated at a CCE = 96.5%.

Experimental set	Air-to-Fuel Gas MFR	Emission Indices (g/kg fuel)			
		THC	CO_2	NO_x	BC
1	15.0	6.65	2 743	1.21	0.088
2	8.5	13.16	2 743	0.90	0.005
3	4.3	9.72	2 743	1.38	0.152
4	7.7	21.09	2 743	1.18	0.120
5	11.4	6.46	2 743	1.08	0.100
6	18.9	6.03	2 743	290	0.069
7	5.3	–	2 994	0.97	2.586
8	6.0	33.24	2 743	1.15	0.002

The industrial-scale flare studies discussed in Chapter 1 can now be revisited to compare their findings with the results obtained in the present experimental study. Starting from the first major study, McDaniel [29] tested a pilot-scale air assisted flare with a 0.46 m ID air riser and a 0.10 m OD internal gas riser. The flare gas with an LHV of 81.3 MJ/m^3 was comparable to experimental set 7, which tested an LHV of 84.9 MJ/m^3. A maximum EI_{THC} of 2.48 g THC/kg flare gas at a CCE ≥ 96.5% was reported (as listed in Table 1.1). However, no THC was measured at a CCE ≥ 96.5% in experimental set 7 since the flame extinguished abruptly. An EI_{CO_2} of 3 103 g CO_2/kg flare gas was very close to the measured value of 2 994 g CO_2/kg flare. An EI_{CO} of 12.18 g CO/kg flare gas was reported, although no CO was detected in experimental set 7 since there was no opportunity for the flame to generate incomplete products of combustion. Lastly, an EI_{NO_x} of 4.11 g NO_x/kg flare

gas was over four times higher than the measured value of 0.97 g NO_x/kg fuel. McDaniel also tested a flare gas mixture with an LHV of 7.74 MJ/m^3. The EIs for this flare gas were considerably lower than any of the values listed in Table 3.5. This is likely because the lowest fuel LHV tested in the present study was 32.8 MJ/m^3, and so is not comparable. No comments can be made regarding the air-to-flare gas MFR from McDaniel's study since the air assist flow rates were not disclosed due to their proprietary nature.

Pohl and Soelberg [32] tested an air-assisted flare with an equivalent diameter of 3.81 cm, which is 1.5 times larger than the outer tube of the burner used in the present study. An average flare gas LHV of 38.9 MJ/m^3 was used in the study, which is comparable to CH_4. They reported a drop in CCE below 96.5% at an air-to-flare gas MFR of 3.3. This value is reasonably close to the corresponding air-to-fuel gas MFR of 4.3 in experimental set 3. The study also reported a maximum EI_{NO_x} of 1.28 g NO_x/kg flare gas at a CCE ≥ 96.5%, which is remarkably close to the tabulated EI_{NO_x} values, except for experimental set 6.

Allen and Torres [36] studied a full-scale industrial air-assisted flare with a nominal diameter of 61 cm. Flare gas mixtures were tested with an LHV of 13 MJ/m^3 and 22 MJ/m^3. A maximum EI_{THC} and EI_{NO_x} of 1.3 g THC/kg flare gas and 0.39 g NO_x/kg flare gas, respectively, were reported at a CCE ≥ 96.5%. These are lower than the experimentally determined values in Table 3.5. Allen and Torres observed that the 13 MJ/m^3 flare gas mixture dropped below CCE = 96.5% at an air-to-flare gas MFR of 22, whereas the 22 MJ/m^3 flare gas mixture exhibited the corresponding drop in CCE at an MFR of 44. These results contradict the present study since the higher LHV fuel (*i.e.*, C_3H_8) experienced a collapse in CCE at a significantly lower air-to-fuel gas MFR than the standard case. A cause for discrepancy is likely due to the sheer scale of the industrial study. This speaks to the caution that must be observed when attempting to project lab-scale results onto large-scale industrial operations. Pohl and Soelberg [32] corroborated this notion by observing that as the flare size decreased, the Reynolds number also decreased. The flare gas Reynolds number of commercial flare heads with a diameter of 61 cm was reported to range from 10^3 to 10^7, of which the present lab-scale study only captured

the very lowest conditions. Another cause for discrepancy is the unique flare head geometry employed in the industrial study. Although the specific design was kept proprietary, the flare head resembled the triangular slots depicted in Figure 1.3b. This would certainly impact fuel-air mixing (and therefore CCE and EIs), just as was demonstrated in the present experimental study, in which altering the burner geometry (*e.g.*, reducing the inner tube OD from 12.7 mm to 6.35 mm) had a significant effect on the results. It is also important to mention that the study by Allen and Torres took place at an outdoor flare test facility. Therefore, the flare was subject to ambient wind conditions which introduced a new hydrodynamic variable. The experiments in the present study were performed in a quiescent environment.

Chapter 4

4. Conclusions and Recommendations

4.1 Conclusions

The objective of the present study was to investigate the nature of industrial air-assisted flares as they relate to pollutant emissions by undertaking a systematic analysis of a lab-scale air-assisted flare. A generic coflow burner was constructed from two concentric stainless-steel tubes to capture the key physical elements of air-assisted flares. The fuel flowed through the annular space between the outer tube (25.4 mm OD and 22.9 mm ID) and different inner tubes with outer diameters of either 6.35 mm or 12.7 mm, which carried the air assist. The inverse flow scheme (*i.e.*, the fuel carried through the inner tube with outer air coflow) was also tested. Thermocouples were installed on the burner to measure the temperature of the fuel and air at the burner exit.

The burner was part of a larger effort to establish a flare testing facility that enabled the safe and controlled performance of combustion experiments. The flare facility was equipped with an array of compressed gas cylinders and gas metering equipment. The fuel gases tested in the study were high purity CH_4 and C_3H_8. Mass flow controllers were used for delivering the fuel gas and pressurized air to a water bath for regulating the temperature of the gases to about 23 °C, before transmitting them to the burner. The combustion products generated by the burner were captured by an exhaust hood situated above the burner. A sample of the combustion products was extracted from a probe installed downstream of the exhaust hood and was delivered to a suite of diagnostic equipment. A PAX was used for measuring aerosol optical properties and in particular was used to obtain the BC mass concentration of

the sample. A NO_x analyzer operated on the principle of chemiluminescence to measure the concentration of NO_x. A Tedlar bag was filled with the exhaust sample and subsequently injected into a GC to measure the mole concentration of O_2, N_2, C1 to C3 hydrocarbons, CO and CO_2.

Two important parameters that characterize air-assisted flare performance are CCE and EI. To quantify these parameters, a carbon mass balance was utilized based on a control volume enclosing the combustion process. The CCE is defined as the ratio of the mass of carbon in the form of CO_2 that was produced by combustion (not including the CO_2 already present in the incoming air or fuel streams), to the mass of carbon derived from the hydrocarbon component of the fuel gas. EI is the mass of pollutant species, namely, THC, CO_2, CO, and NO_x released per unit mass of fuel gas.

Eight unique experimental sets were conducted in the present study. The first set established the standard case and consisted of an outer coflow of CH_4 at a constant 20 SLPM and air injected through an inner tube with a 12.7 mm OD. A maximum EI_{BC} of 0.088 g BC/kg fuel was measured at an air-to-fuel gas MFR of 0.2 and thereafter dropped by two orders of magnitude. This reduction was ascribed to increased air flow promoting a higher degree of fuel-air mixing. EI_{CO_2} and EI_{NO_x} remained nearly constant at a maximum value of 2.7 kg CO_2/kg fuel and 1.21 g NO_x/kg fuel, respectively, with NO_x levels diminishing earlier. The flame maintained a CCE $\geq$ 96.5% up to an air-to-fuel gas MFR of 14.9, after which the flame exhibited localized extinctions, followed by a collapse in CCE. This drop occurred in conjunction with EI_{CO_2} by 1.5 orders of magnitude and EI_{NO_x} by almost two orders of magnitude. The decrease in NO_x can be associated with reduced temperatures in the combustion zone due to cooling of the fuel stream at increasing MFRs. Moreover, the fuel-stripping mechanism was instigated and EI_{CH_4} was found to increase by two orders of magnitude to a maximum of 960 g CH_4/kg fuel. A maximum EI_{CO} of 116 g CO/kg fuel was measured during the collapse. A product of incomplete combustion, CO was likely the result of an excessively turbulent air stream inhibiting the combustion process. $EI_{CO_2,eq}$ captured the total effect of the pollutant emissions and remained a constant value until the collapse in CCE, at which point it rose to a maximum value of 27 kg CO_2/kg fuel. This is essentially venting of CH_4.

Experimental set 2 investigated double the flow rate of CH_4. The maximum EI_{BC} was about 1.5 orders of magnitude less than experimental set 1. This difference was explained by an increase in the fuel exit Reynolds number to 1 193 from 567, suggesting that entrainment of ambient air is occurring to a greater extent and driving combustion towards completion. The onset of collapse in CCE occurred at about half the air-to-fuel gas MFR compared to the reference case. It was concluded that due to greater entrainment of ambient air into the combustion zone through turbulent mixing, less air assist would be required to trigger a collapse in CCE. A maximum EI_{CO} of 40 g CO/kg fuel was measured, which is a third of the reference case, likely resulting from better fuel-air mixing.

Experimental set 3 implemented an inner tube with half the diameter of the reference case. A maximum EI_{BC} of 0.152 g BC/kg fuel was an increase by a factor of 1.7 compared to experimental set 1. This was accounted for by a lower fuel stream momentum which suggested that less fuel-air mixing was occurring, preventing BC from fully oxidizing. The maximum EI_{NO_x} was 14% higher than the reference case. This can be tied to better mixing in the combustion zone which would be conducive to thermal NO_x formation. The early collapse in CCE at an air-to-fuel gas MFR of 4.2 was associated with a smaller inner tube diameter. This gave rise to a higher velocity and momentum gradient between the air and fuel streams, prompting flame instability and initiating the fuel-stripping mechanism. CO was not detected in this experimental set.

The next three sets of experiments replaced air assist with an equivalent air assist that attempted to replicate the hydrodynamic characteristics of air. Experimental set 4 employed a mixture consisting of 92% N_2 and 8% Ar by volume. The NOx emissions exhibited a steady decline as opposed to remaining constant until the collapse in CCE as was evident in experimental sets 1 to 3. This was a consequence of reductions in flame temperature due to more diluents in the products and availability of O_2. A maximum EI_{CO} of 142 g CO/kg fuel was measured which was 22% more than the reference case. Experimental set 5 introduced 10.5% O_2 in the assist mixture. The maximum EI_{BC} and EI_{CO} as well as the onset of collapse in CCE were found to be the average of experimental sets 1 and 4. The final equivalent air

assist mixture consisted of 42% O_2. A unique observation was the sudden ignition of an inner flame at an equivalent air-to-fuel gas MFR of 0.5. A maximum EI_{NO_x} of 290 g NO_x/kg fuel was measured and was associated with high flame temperatures and abundance of O_2 in the assist stream. The flame sustained a CCE of 100% up to an equivalent air-to-fuel gas MFR of 18.9 before exhibiting a step-like drop to 0%. The final point of interest was $EI_{CO_2,eq}$, which decreased in conjunction with an increase in NO_x.

Experimental set 7 replaced CH_4 fuel with C_3H_8. A maximum EI_{BC} of 2.586 g BC/kg fuel was 29 times greater than the reference case. The flame extinguishing abruptly at an air-to-fuel gas MFR of 5.3, represented as a step drop in CCE to 0%. It was believed that since the C_3H_8 fuel jet had an exit Reynolds number of 2 166, nearly four times higher than CH_4, comparatively less assist air was required to trigger flame instability. No CO was detected due to the abrupt collapse in CCE. $EI_{CO_2,eq}$ was measured at a maximum of 5.31 kg CO_2/kg fuel since C_3H_8 has a 100-year GWP of only 3.3.

The final set of experiments inverted the flow scheme such that CH_4 flowed through the inner tube and air assist through the annulus. A maximum EI_{BC} of 0.002 g BC/kg fuel was the least of all experimental sets. A probable explanation was that the fuel Reynolds number was 2 278, four times greater than the reference case, which increased entrainment of ambient air into the fuel stream. The most notable observation was flame lift-off. The flame extinguished at an air-to-fuel gas MFR of 6.1 with a step drop in CCE.

The industrial-scale flare studies were revisited to compare with the results obtained from the present study. Pohl and Soelberg tested an air-assisted flare with an equivalent diameter 1.5 times larger than the lab-scale burner. The reported drop in CCE below 96.5% and the maximum EI_{NO_x} at CCE $\geq$ 96.5% were found to be in close agreement with experimental set 3. However, the studies performed by McDaniel and Allen and Torres were not in conformance with any of the experimental sets, especially the latter study. This suggests that caution must be observed when attempting to draw parallels between lab-scale results and large-scale industrial operations. A leading cause of discrepancy is that industrial-scale flares operate at a

Reynolds number ranging from 10^3 to 10^7, such that the current lab-scale flares only capture the very lowest conditions. The flare head designs employed by the industrial studies also differ substantially from the present study. Lastly, the study by Allen and Torres took place at an outdoor flare test facility which is subject to ambient wind conditions, whereas the present study was performed in a quiescent environment.

4.2 Recommendations

Due to the lack of conformity between the lab-scale and industrial-scale results, the recommended course of action would be to design and test a larger scale burner. A reasonable burner size to consider would be based on an OD of 7.62 cm, which is three times the diameter of the burner used in the present study. Such a burner would be categorized as a full-scale flare (according to Allen and Torres) and the results would be more applicable to industrial flare operations. It could potentially shed light on how CCE and various pollutant emissions scale up with size, from a lab-scale flare, to a full-scale flare, and finally to an industrial-scale flare. Another recommendation would be to test flare head designs more representative of industrial-scale flares. This would further close the gap between the industrial and lab scale and yield significant findings with regards to CCE, EIs and hydrodynamics.

Different diagnostic techniques are also recommended for incorporating into the experimental setup to enhance the understanding of flame structure and chemical reaction mechanisms. The first technique is Particle Image Velocimetry (PIV) which is a laser diagnostic technique based on seeding the flow with tracer particles. By tracking the motion of the particles with a camera, it is possible to visualize the velocity field, flame front structure, reaction zones, and regions of fuel-air mixing. Another technique is measuring the flame temperature using thermocouples. The flame temperature can offer insight into species reaction rates, such as thermal NO_x formation.

Bibliography

[1] C.D. Elvidge, M.D. Bazilian, M. Zhizhin, T. Ghosh, K. Baugh, F.-C. Hsu, The potential role of natural gas flaring in meeting greenhouse gas mitigation targets, Energy Strategy Reviews. 20 (2018) 156–162. doi:10.1016/j.esr.2017.12.012.

[2] Zero Routine Flaring by 2030, World Bank. (n.d.). http://www.worldbank.org/en/programs/zero-routine-flaring-by-2030 (accessed November 26, 2018).

[3] G. Hartfield, J. Blunden, D.S. Arndt, A Look at 2017: Takeaway Points from the *State of the Climate* Supplement, Bulletin of the American Meteorological Society. 99 (2018) 1527–1539. doi:10.1175/BAMS-D-18-0173.1.

[4] FAQ 1.3 - AR4 WGI Chapter 1: Historical Overview of Climate Change Science, (n.d.). https://www.ipcc.ch/publications_and_data/ar4/wg1/en/faq-1-3.html (accessed December 1, 2018).

[5] National Research Council (U.S.), ed., Surface temperature reconstructions for the last 2,000 years, National Academies Press, Washington, D.C, 2006.

[6] G. Myhre, D. Shindell, F.-M. Bréon, W. Collins, J. Fuglestvedt, J. Huang, D. Koch, J.-F. Lamarque, D. Lee, B. Mendoza, T. Nakajima, A. Robock, G. Stephens, T. Takemura, H. Zhang, Anthropogenic and Natural Radiative Forcing, in: Climate Change 2013: The Physical Science Basis. Contribution of Working Group I to the Fifth Assessment Report of the Intergovernmental Panel on Climate Change, Cambridge University Press, 2013.

[7] Reducing methane emissions, (n.d.). https://www.alberta.ca/climate-methane-emissions.aspx (accessed November 26, 2018).

[8] D.K. Stone, S.K. Lynch, R.F. Pandullo, L.B. Evans, W.M. Vatavuk, Flares. Part I: Flaring Technologies for Controlling VOC-Containing Waste Streams, Journal of the Air & Waste Management Association. 42 (1992) 333–340. doi:10.1080/10473289.1992.10466996.

[9] T. Novakov, H. Rosen, The Black Carbon Story: Early History and New Perspectives, AMBIO. 42 (2013) 840–851. doi:10.1007/s13280-013-0392-8.

[10] T.C. Bond, S.J. Doherty, D.W. Fahey, P.M. Forster, T. Berntsen, B.J. DeAngelo, M.G. Flanner, S. Ghan, B. Kärcher, D. Koch, S. Kinne, Y. Kondo, P.K. Quinn, M.C. Sarofim, M.G. Schultz, M. Schulz, C. Venkataraman, H. Zhang, S. Zhang, N. Bellouin, S.K. Guttikunda, P.K. Hopke, M.Z. Jacobson, J.W. Kaiser, Z. Klimont, U. Lohmann, J.P. Schwarz, D. Shindell, T. Storelvmo, S.G. Warren, C.S. Zender, Bounding the role of black carbon in the climate system: A scientific assessment: BLACK CARBON IN THE CLIMATE SYSTEM, Journal of Geophysical Research: Atmospheres. 118 (2013) 5380–5552. doi:10.1002/jgrd.50171.

[11] A. Stohl, Z. Klimont, S. Eckhardt, K. Kupiainen, V.P. Shevchenko, V.M. Kopeikin, A.N. Novigatsky, Black carbon in the Arctic: the underestimated role of gas flaring and residential combustion emissions, Atmospheric Chemistry and Physics. 13 (2013) 8833–8855. doi:10.5194/acp-13-8833-2013.

[12] M. Sand, T.K. Berntsen, Ø. Seland, J.E. Kristjánsson, Arctic surface temperature change to emissions of black carbon within Arctic or midlatitudes: ARCTIC CLIMATE RESPONSE TO BLACK CARBON, Journal of

Geophysical Research: Atmospheres. 118 (2013) 7788–7798. doi:10.1002/jgrd.50613.
[13] D.T. Allen, Emissions from oil and gas operations in the United States and their air quality implications, Journal of the Air & Waste Management Association. 66 (2016) 549–575. doi:10.1080/10962247.2016.1171263.
[14] D.S. Stevenson, P.J. Young, V. Naik, J.-F. Lamarque, D.T. Shindell, A. Voulgarakis, R.B. Skeie, S.B. Dalsoren, G. Myhre, T.K. Berntsen, G.A. Folberth, S.T. Rumbold, W.J. Collins, I.A. MacKenzie, R.M. Doherty, G. Zeng, T.P.C. van Noije, A. Strunk, D. Bergmann, P. Cameron-Smith, D.A. Plummer, S.A. Strode, L. Horowitz, Y.H. Lee, S. Szopa, K. Sudo, T. Nagashima, B. Josse, I. Cionni, M. Righi, V. Eyring, A. Conley, K.W. Bowman, O. Wild, A. Archibald, Tropospheric ozone changes, radiative forcing and attribution to emissions in the Atmospheric Chemistry and Climate Model Intercomparison Project (ACCMIP), Atmospheric Chemistry and Physics. 13 (2013) 3063–3085. doi:10.5194/acp-13-3063-2013.
[15] M. Strosher, Investigations of Flare Gas Emissions in Alberta, 1996. https://ags.aer.ca/document/SPE/SPE_005.pdf.
[16] O. US EPA, Integrated Risk Information System, US EPA. (2013). https://www.epa.gov/iris (accessed November 30, 2018).
[17] M.R. Johnson, L.W. Kostiuk, J.L. Spangelo, A Characterization of Solution Gas Flaring in Alberta, Journal of the Air & Waste Management Association. 51 (2001) 1167–1177. doi:10.1080/10473289.2001.10464348.
[18] O. US EPA, Sulfur Dioxide Basics, US EPA. (2016). https://www.epa.gov/so2-pollution/sulfur-dioxide-basics (accessed December 2, 2018).
[19] G. Ottinger, Refining expertise: how responsible engineers subvert environmental justice challenges, New York University Press, New York, 2013.
[20] General control device and work practice requirements, 2008. https://www.ecfr.gov/cgi-bin/text-idx?SID=06fa3b7ca89e83104632002da198af87&node=se40.7.60_118&rgn=div8 (accessed December 4, 2018).
[21] API Standard 521: Pressure-relieving and Depressuring Systems, 6th Edition, American Petroleum Institute, 2014.
[22] API Standard 537: Flare Details for General Refinery and Petrochemical Service, 2nd Edition, American Petroleum Institute, 2008.
[23] N.P. Cheremisinoff, Industrial gas flaring practices, Wiley, Hoboken, New Jersey, 2013.
[24] S. Smith, G. Seefeldt, Use of Variable Frequency Drives for Better Destruction Efficiency of Air-Assisted Flares, AFRC 2013 Industrial Combustion Symposium, 2013. https://collections.lib.utah.edu/details?id=14357.
[25] 40 CFR 63.670 - Requirements for flare control devices., LII / Legal Information Institute. (n.d.). https://www.law.cornell.edu/cfr/text/40/63.670 (accessed January 19, 2019).
[26] D. Hasselle, Accused of Clean Air Act violations, Shell agrees to $10 million of pollution controls in Norco, The Advocate. (2018). https://www.theadvocate.com/new_orleans/news/courts/article_5540baa0-14ca-11e8-b535-fbe15824c085.html (accessed December 22, 2018).

[27] J. Siciliano, EPA fines Exxon $2.5 million for air quality violations, Washington Examiner. (2017). https://www.washingtonexaminer.com/epa-fines-exxon-25-million-for-air-quality-violations (accessed December 22, 2018).
[28] U.S. Environmental Protection Agency, EPA Enforcement Targets Flaring Efficiency Violations, Office of Enforcement and Compliance Assurance, 2012. https://www.epa.gov/sites/production/files/documents/flaringviolations.pdf (accessed December 22, 2018).
[29] M. McDaniel, Flare Efficiency Study, U.S. Environmental Protection Agency, Washington, D.C., 1983. https://www3.epa.gov/ttnchie1/old/ap42/ch13/s05/reference/ref_01c13s05_jan1995.pdf.
[30] U.S. Environmental Protection Agency, AP-42: Compilation of Air Emissions Factors, 2018. https://www3.epa.gov/ttn/chief/ap42/ch13/final/C13S05_02-05-18.pdf (accessed December 25, 2018).
[31] J.D.N. McEwen, M.R. Johnson, Black carbon particulate matter emission factors for buoyancy-driven associated gas flares, Journal of the Air & Waste Management Association. 62 (2012) 307–321. doi:10.1080/10473289.2011.650040.
[32] J.H. Pohl, N.R. Soelberg, Evaluation of the Efficiency of Industrial Flares: Flare Head Design and Gas Composition, U.S. Environmental Protection Agency, Washington, D.C., 1985.
[33] C. Shaddix, A. Molina, Ignition, flame stability, and char combustion in oxy-fuel combustion, in: Oxy-Fuel Combustion for Power Generation and Carbon Dioxide (CO2) Capture, Elsevier, 2011: pp. 101–124. doi:10.1533/9780857090980.2.101.
[34] Y. Wu, Flame Lift-Off and Blow-Out Stability Limits and Their Application in Gas Burners, in: M. Lackner, F. Winter, A.K. Agarwal (Eds.), Handbook of Combustion, Wiley-VCH Verlag GmbH & Co. KGaA, Weinheim, Germany, 2010. doi:10.1002/9783527628148.hoc044.
[35] E.R. Subbarao, B.J. Cantwell, Investigation of a co-flowing buoyant jet: experiments on the effect of Reynolds number and Richardson number, Journal of Fluid Mechanics. 245 (1992) 69. doi:10.1017/S0022112092000351.
[36] D.T. Allen, V.M. Torres, TCEQ 2010 Flare Study Final Report, The University of Texas at Austin, 2011. https://www.tceq.texas.gov/assets/public/implementation/air/rules/Flare/2010flarestudy/2010-flare-study-final-report.pdf.
[37] V.M. Torres, S. Herndon, E. Wood, F.M. Al-Fadhli, D.T. Allen, Emissions of Nitrogen Oxides from Flares Operating at Low Flow Conditions, Industrial & Engineering Chemistry Research. 51 (2012) 12600–12605. doi:10.1021/ie300179x.
[38] E.C. Fortner, W.A. Brooks, T.B. Onasch, M.R. Canagaratna, P. Massoli, J.T. Jayne, J.P. Franklin, W.B. Knighton, J. Wormhoudt, D.R. Worsnop, C.E. Kolb, S.C. Herndon, Particulate Emissions Measured During the TCEQ Comprehensive Flare Emission Study, Industrial & Engineering Chemistry Research. 51 (2012) 12586–12592. doi:10.1021/ie202692y.

[39] J.M. Wallace, P.V. Hobbs, Atmospheric Chemistry, in: Atmospheric Science, Elsevier, 2006: pp. 153–207. doi:10.1016/B978-0-12-732951-2.50010-7.
[40] Droplet Measurement Technologies, Inc., Photoacoustic Extinctiometer (PAX) Operator Manual, Boulder, CO, n.d. http://www.dropletmeasurement.com/sites/default/files/ManualsGuides/Hardware%20Manuals/PAX%20Manual.pdf.
[41] T.A. Cool, J.E.M. Goldsmith, Laser-enhanced flame ionization detector, Applied Optics. 26 (1987) 3542–3551. doi:10.1364/AO.26.003542.
[42] K. Schofield, The enigmatic mechanism of the flame ionization detector: Its overlooked implications for fossil fuel combustion modeling, Progress in Energy and Combustion Science. 34 (2008) 330–350. doi:10.1016/j.pecs.2007.08.001.
[43] T. Holm, Aspects of the mechanism of the flame ionization detector, Journal of Chromatography A. 842 (1999) 221–227. doi:10.1016/S0021-9673(98)00706-7.
[44] C.F. Poole, Ionization-based detectors for gas chromatography, Journal of Chromatography A. 1421 (2015) 137–153. doi:10.1016/j.chroma.2015.02.061.
[45] L.A. Colón, L.J. Baird, Detectors in Modern Gas Chromatography, in: R.L. Grob, E.F. Barry (Eds.), Modern Practice of Gas Chromatography, 4th ed., Wiley-Interscience, Hoboken, N.J, 2004: pp. 277–337.
[46] M.S. Klee, Detectors, in: Gas Chromatography, 1st ed., Elsevier, 2012: pp. 307–347. doi:10.1016/B978-0-12-385540-4.00012-2.
[47] D.J. Corbin, M.R. Johnson, Detailed Expressions and Methodologies for Measuring Flare Combustion Efficiency, Species Emission Rates, and Associated Uncertainties, Industrial & Engineering Chemistry Research. 53 (2014) 19359–19369. doi:10.1021/ie502914k.
[48] Chemical Equilibrium Calculator, (n.d.). http://navier.engr.colostate.edu/code/code-4/index.html (accessed March 2, 2019).
[49] W.C. Baker, J.F. Pouchot, The Measurement of Gas Flow Part II, Journal of the Air Pollution Control Association. 33 (1983) 156–162. doi:10.1080/00022470.1983.10465559.

Appendix A Uncertainty Analysis Methodology

This section presents the methodology for estimating the uncertainties associated with the various instruments used in the experimental study. The uncertainty analysis is based on two types of measurement errors: bias error (B_x) and precision error (P_x). Bias error (also called systematic error) is an inherent error of a device that is present with every measurement. It is typically communicated by the manufacturer as part of the technical specifications or is estimated from a calibration curve. Precision error (also called random error) arises when a measurement is repeated and can be estimated using concepts from statistics and probability. Since the number of measurements taken with any given instrument typically exceeded 30, the standard normal distribution was used to estimate the precision uncertainty associated with the measured value. This was defined as

$$P_x = z\frac{\sigma}{\sqrt{n}}, \tag{A.1}$$

where z is the z-score evaluated at 1.96 for a confidence interval of 95%, σ is the standard deviation, and n is the number of measurements taken. The standard deviation is defined as

$$\sigma = \sqrt{\frac{\sum(x_i - \bar{x})^2}{n}}, \tag{A.2}$$

where x_i is the measured value and $\bar{x}$ is the mean of the measured values. The total uncertainty combines bias and precision uncertainty, assuming they are both evaluated at the same confidence interval (typically 95%), and can be calculated as

$$U_x = \Delta x = \sqrt{{B_x}^2 + {P_x}^2}. \tag{A.3}$$

Another important concept is propagation of uncertainty. This combines the effects of uncertainties from multiple variables on a function. If y is a function of N independent variables evaluated at the same confidence interval (*i.e.*, $y = f(x_1, x_2, \ldots, x_N)$), the uncertainty in y can be approximated as

$$\Delta y = \sqrt{\left(\frac{\partial f}{\partial x_1}\Delta x_1\right)^2 + \left(\frac{\partial f}{\partial x_2}\Delta x_2\right)^2 + \cdots + \left(\frac{\partial f}{\partial x_N}\Delta x_N\right)^2}. \quad \text{(A.4)}$$

Appendix B Mass Flow Controller Calibration

Each mass flow controller (MFC) was calibrated for various gases using a drum-type gas meter (Ritter, TG-50) based on the setup shown in Figure B.1. The gas was dispensed from the compressed cylinder to the circulating water bath which was set to 35 °C to regulate the temperature of the gas to about room temperature (23 °C). The MFC controls the flow rate of gas into the meter in standard liters per minute (SLPM). Drum-type gas meters operate on the principle of displacement [49]. The meter consists of an internal drum partitioned into four chambers that is free to rotate within an outer drum half filled with water. The internal drum is caused to rotate as the gas fills and is displaced from the chambers in sequence. When the gas exits the meter it flows through plastic tubing to the exhaust hood.

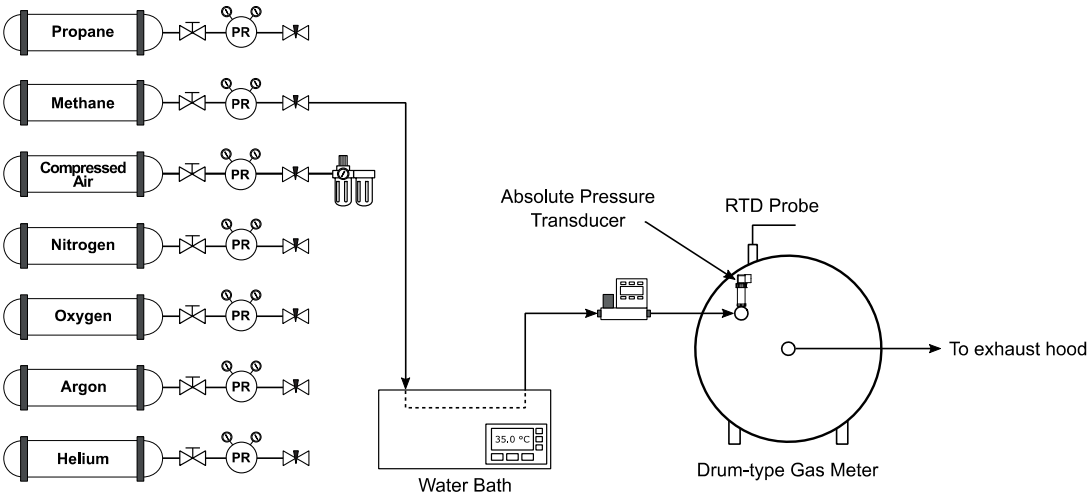

Figure B.1: MFC calibration setup.

The meter calculates the volumetric flow rate of the gas which is a product of the known volume of the chambers, the number of chambers, and the number of revolutions of the drum per unit time. The volumetric flow rate is transmitted via RS-232 to the computer and is recorded using a LabVIEW program. Temperature and pressure were measured at the gas meter inlet to enable correction of the volumetric flow rate using an RTD probe (Omega Engineering, P-L Series) and an absolute

pressure transducer (Omega Engineering, PX409-USBH Series), respectively. The volumetric flow rate was corrected to SLPM based on the ideal gas law as

$$\dot{V}_s = \dot{V}_g \frac{pT_o}{p_o T} \tag{B.1}$$

where $\dot{V}_g$ (LPM) is the volumetric flow rate at pressure p (kPa) and temperature T (K) in liters per minute calculated by the gas meter, and p_o and T_o are standard pressure and temperature (*i.e.*, 101.3 kPa and 25 °C, respectively). This allowed for direct comparison with the flow rate set by the MFC.

A sample calibration curve for a 50 SLPM MFC dispensing methane is shown in Figure B.2. A total of 10 calibration points were tested starting from 5 SLPM and increasing by increments of five. The plot demonstrated a very good linear fit. A maximum bias uncertainty of 0.1 SLPM was calculated based on a 95% confidence interval. This is smaller than the measurement uncertainty communicated in the MFC manual, which is ± (0.8% of reading + 0.1 SLPM).

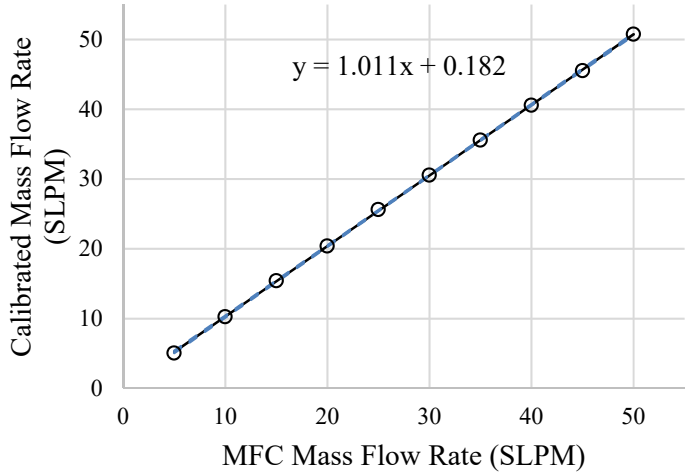

Figure B.2: 50 SLPM MFC calibration curve for methane.

Appendix C Gas Chromatograph Calibration Standards and Uncertainties

The gas chromatograph (GC) was calibrated using the calibration standards listed in Table C.1.

Table C.1: GC calibration standards.

Standard	Gas species (mol %)									
	H_2	CO	CO_2	CH_4	C_2H_6	C_3H_8	C_4H_{10}	N_2	He	O_2
1		0.0998	5.01					93.88		1.01
2	0.4018	19.95		0.1002	0.09975	0.09937		79.449		
3		0.01						99.889		0.1005
5	4.005			0.9947	1.013	1.008		92.979		
6	19.93			4.971	4.994	5.07		65.035		
9		3.005	19.95					57.055		19.99
10		0.6016	10.01					85.396		3.992
11	0.04	9.983		0.0105	0.0101	0.0102		89.946		
12			0.8108	94.96	2.4	0.0589	0.0103	1.76		
13			0.01	49.97			0.1	49.9	0.02	
14			0.09969					99.79971	0.1006	
15			0.0402	0.001	0.001	0.001	0.001	99.905802	0.05	

To quantify CCE and EIs for the carbon based species (*i.e.*, THC, CO_2, and CO), the calibration curves for these species were used. A sample calibration curve for CH_4 is shown in Figure C.1.

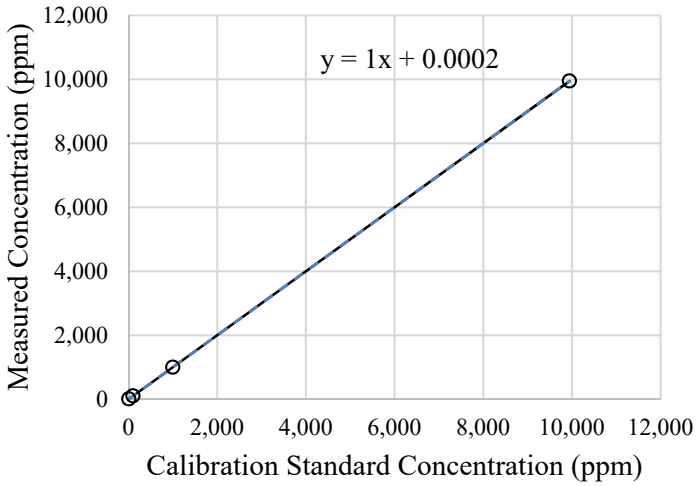

Figure C.1: GC calibration curve for CH_4.

A linear regression was applied to each calibration curve to generate a linear equation. The bias uncertainties were defined as the largest deviation from a 95% confidence interval and are listed in Table C.2. The precision uncertainty was calculated based on repeated measurements from the GC. This was accomplished by filling a 100 L Tedlar bag with a sample of the exhaust products representative of an actual experiment. The sample was injected and analyzed by the GC five consecutive times to obtain five concentrations for each carbon based species. The precision uncertainty for each species was then calculated using the student t distribution. This procedure was performed three times. The largest uncertainty for each species was selected as the characteristic precision uncertainty and are shown in Table C.2. The total uncertainty for each species was also calculated and is summarized in Table C.2.

Table C.2: Uncertainties associated with each carbon based species.

Species	Uncertainty (ppm)		
	Bias, B_x	Precision, P_x	Total, U_x
CH_4	0.02	38.2	38.2
C_2H_6	0.001	22.8	22.8
C_3H_8	0.015	2.1	2.1
CO_2	0.009	67.9	67.9
CO	0.014	11.8	11.8

Appendix D Uncertainty Analysis of CCE and EI

This section will outline expressions for calculating the uncertainty in CCE and EI evaluated using propagation of uncertainty. The CCE was expressed in Eq. 2.6 and the uncertainty is defined as

$$(\Delta\eta)^2 = \left(\frac{\partial\eta}{\partial\dot{n}_{\mathrm{CO_2,produced}}}\Delta\dot{n}_{\mathrm{CO_2,produced}}\right)^2 + \left(\frac{\partial\eta}{\partial\dot{n}_{\mathrm{FG}}}\Delta\dot{n}_{\mathrm{FG}}\right)^2. \tag{D.1}$$

The molar flow rate of produced CO_2, $\dot{n}_{\mathrm{CO_2,produced}}$, was expressed in Eq. 2.5, and the error is defined as

$$\begin{aligned}\left(\Delta\dot{n}_{\mathrm{CO_2,produced}}\right)^2 &= \left(\frac{\partial\dot{n}_{\mathrm{CO_2,produced}}}{\partial X_{\mathrm{CO_2,plume}}}\Delta X_{\mathrm{CO_2,plume}}\right)^2 + \\ &\left(\frac{\partial\dot{n}_{\mathrm{CO_2,produced}}}{\partial\dot{n}_{\mathrm{plume}}}\Delta\dot{n}_{\mathrm{plume}}\right)^2 + \left(\frac{\partial\dot{n}_{\mathrm{CO_2,produced}}}{\partial X_{\mathrm{CO_2},\infty}}\Delta X_{\mathrm{CO_2},\infty}\right)^2 + \\ &\left(\frac{\partial\dot{n}_{\mathrm{CO_2,produced}}}{\partial\dot{n}_{\infty}}\Delta\dot{n}_{\infty}\right)^2 + \left(\frac{\partial\dot{n}_{\mathrm{CO_2,produced}}}{\partial X_{\mathrm{CO_2,FG}}}\Delta X_{\mathrm{CO_2,FG}}\right)^2 + \left(\frac{\partial\dot{n}_{\mathrm{CO_2,produced}}}{\partial\dot{n}_{\mathrm{FG}}}\Delta\dot{n}_{\mathrm{FG}}\right)^2.\end{aligned} \tag{D.2}$$

It was assumed that no CO_2 was present in the fuel gas since high purity fuels were used. Then Eq. D.2 can be simplified to

$$\begin{aligned}\left(\Delta\dot{n}_{\mathrm{CO_2,produced}}\right)^2 &= \left(\frac{\partial\dot{n}_{\mathrm{CO_2,produced}}}{\partial X_{\mathrm{CO_2,plume}}}\Delta X_{\mathrm{CO_2,plume}}\right)^2 + \\ &\left(\frac{\partial\dot{n}_{\mathrm{CO_2,produced}}}{\partial\dot{n}_{\mathrm{plume}}}\Delta\dot{n}_{\mathrm{plume}}\right)^2 + \left(\frac{\partial\dot{n}_{\mathrm{CO_2,produced}}}{\partial X_{\mathrm{CO_2},\infty}}\Delta X_{\mathrm{CO_2},\infty}\right)^2 + \left(\frac{\partial\dot{n}_{\mathrm{CO_2,produced}}}{\partial\dot{n}_{\infty}}\Delta\dot{n}_{\infty}\right)^2.\end{aligned} \tag{D.3}$$

Eq. 2.6 was manipulated to isolate for the molar flow rate of the plume, $\dot{n}_{\mathrm{plume}}$. Then the error in $\dot{n}_{\mathrm{plume}}$ is defined as

$$\left(\Delta\dot{n}_{\text{plume}}\right)^2 = \left(\frac{\partial\dot{n}_{\text{plume}}}{\partial\dot{n}_{\text{FG}}}\Delta\dot{n}_{\text{FG}}\right)^2 + \sum_k\left(\frac{\partial\dot{n}_{\text{plume}}}{\partial X_{k,\infty}}\Delta X_{k,\infty}\right)^2 + \left(\frac{\partial\dot{n}_{\text{plume}}}{\partial X_{\text{CO}_2,\text{FG}}}\Delta X_{\text{CO}_2,\text{FG}}\right)^2 + \sum_k\left(\frac{\partial\dot{n}_{\text{plume}}}{\partial X_{k,\text{plume}}}\Delta X_{k,\text{plume}}\right)^2. \quad \text{(D.4)}$$

As mentioned earlier, CO_2 is assumed not to be present in the fuel gas. Eq. D.4 can then be simplified to

$$\left(\Delta\dot{n}_{\text{plume}}\right)^2 = \left(\frac{\partial\dot{n}_{\text{plume}}}{\partial\dot{n}_{\text{FG}}}\Delta\dot{n}_{\text{FG}}\right)^2 + \sum_k\left(\frac{\partial\dot{n}_{\text{plume}}}{\partial X_{k,\infty}}\Delta X_{k,\infty}\right)^2 + \sum_k\left(\frac{\partial\dot{n}_{\text{plume}}}{\partial X_{k,\text{plume}}}\Delta X_{k,\text{plume}}\right)^2. \quad \text{(D.5)}$$

The error in the molar flow rate of the fuel gas, $\dot{n}_{\text{FG}}$, is based on the mass flow rate of the fuel and is defined as

$$\Delta\dot{n}_{\text{FG}} = \frac{\partial\dot{n}_{\text{FG}}}{\partial\dot{m}_{\text{FG}}}\Delta\dot{m}_{\text{FG}} = \frac{\Delta\dot{m}_{\text{FG}}}{M_{FG}}. \quad \text{(D.6)}$$

The molar flow rate of ambient air is defined based on the control volume illustrated in Figure 2.5. It is expressed as

$$\dot{n}_{\infty} = \frac{M_{\text{plume}}}{M_{\infty}}\dot{n}_{\text{plume}} - \frac{M_{\text{FG}}}{M_{\infty}}\dot{n}_{\text{FG}}. \quad \text{(D.7)}$$

Then the error in $\dot{n}_{\infty}$ can be defined as

$$(\Delta\dot{n}_{\infty})^2 = \left(\frac{\partial\dot{n}_{\infty}}{\partial\dot{n}_{\text{plume}}}\Delta\dot{n}_{\text{plume}}\right)^2 + \left(\frac{\partial\dot{n}_{\infty}}{\partial\dot{n}_{\text{FG}}}\Delta\dot{n}_{\text{FG}}\right)^2. \quad \text{(D.8)}$$

Finally, the error in CCE can be simplified to

$$(\Delta\eta)^2 = \left(\frac{\partial\eta}{\partial\dot{n}_{\mathrm{CO_2,produced}}}\right)^2 \left\{\left(\frac{\partial\dot{n}_{\mathrm{CO_2,produced}}}{\partial X_{\mathrm{CO_2,plume}}}\Delta X_{\mathrm{CO_2,plume}}\right)^2 + \left(\frac{\partial\dot{n}_{\mathrm{CO_2,produced}}}{\partial\dot{n}_{\mathrm{plume}}}\right)^2 \left[\left(\frac{\partial\dot{n}_{\mathrm{plume}}}{\partial\dot{n}_{\mathrm{FG}}}\frac{\Delta\dot{m}_{\mathrm{FG}}}{M_{FG}}\right)^2 + \sum_k\left(\frac{\partial\dot{n}_{\mathrm{plume}}}{\partial X_{k,\infty}}\Delta X_{k,\infty}\right)^2 + \sum_k\left(\frac{\partial\dot{n}_{\mathrm{plume}}}{\partial X_{k,\mathrm{plume}}}\Delta X_{k,\mathrm{plume}}\right)^2\right] + \left(\frac{\partial\dot{n}_{\mathrm{CO_2,produced}}}{\partial X_{\mathrm{CO_2},\infty}}\Delta X_{\mathrm{CO_2},\infty}\right)^2 + \left(\frac{\partial\dot{n}_{\mathrm{CO_2,produced}}}{\partial\dot{n}_{\infty}}\right)^2 \left[\left(\frac{\partial\dot{n}_{\infty}}{\partial\dot{n}_{\mathrm{plume}}}\right)^2 \left(\left(\frac{\partial\dot{n}_{\mathrm{plume}}}{\partial\dot{n}_{\mathrm{FG}}}\frac{\Delta\dot{m}_{\mathrm{FG}}}{M_{FG}}\right)^2 + \sum_k\left(\frac{\partial\dot{n}_{\mathrm{plume}}}{\partial X_{k,\infty}}\Delta X_{k,\infty}\right)^2 + \sum_k\left(\frac{\partial\dot{n}_{\mathrm{plume}}}{\partial X_{k,\mathrm{plume}}}\Delta X_{k,\mathrm{plume}}\right)^2\right) + \left(\frac{\partial\dot{n}_{\infty}}{\partial\dot{n}_{\mathrm{FG}}}\frac{\Delta\dot{m}_{\mathrm{FG}}}{M_{FG}}\right)^2\right]\right\} + \left(\frac{\partial\eta}{\partial\dot{n}_{\mathrm{FG}}}\frac{\Delta\dot{m}_{\mathrm{FG}}}{M_{FG}}\right)^2. \quad \text{(D.9)}$$

The uncertainties associated with the species mole fractions $X_{k,\infty}$ and $X_{k,\mathrm{plume}}$ are listed in Table C.2 of Appendix C. The error in mass flow rate of the fuel gas, $\dot{m}_{\mathrm{FG}}$, is based on the uncertainty of the mass flow controller. The EI of gas-phase species was expressed in Eq. 2.9 and the uncertainty is defined as

$$(\Delta EI_j)^2 = \left(\frac{\partial EI_j}{\partial X_{j,\mathrm{plume}}}\Delta X_{j,\mathrm{plume}}\right)^2 + \left(\frac{\partial EI_j}{\partial X_{j,\infty}}\Delta X_{j,\infty}\right)^2 + \left(\frac{\partial EI_j}{\partial\dot{n}_{\mathrm{plume}}}\Delta\dot{n}_{\mathrm{plume}}\right)^2 + \left(\frac{\partial EI_j}{\partial\dot{m}_{\mathrm{FG}}}\Delta\dot{m}_{\mathrm{FG}}\right)^2. \quad \text{(D.10)}$$

The above expression can be simplified to

$$(\Delta EI_j)^2 = \left(\frac{\partial EI_j}{\partial X_{j,\mathrm{plume}}}\Delta X_{j,\mathrm{plume}}\right)^2 + \left(\frac{\partial EI_j}{\partial X_{j,\infty}}\Delta X_{j,\infty}\right)^2 + \left(\frac{\partial EI_j}{\partial\dot{n}_{\mathrm{plume}}}\right)^2 \left[\left(\frac{\partial\dot{n}_{\mathrm{plume}}}{\partial\dot{n}_{\mathrm{FG}}}\frac{\Delta\dot{m}_{\mathrm{FG}}}{M_{FG}}\right)^2 + \sum_k\left(\frac{\partial\dot{n}_{\mathrm{plume}}}{\partial X_{k,\infty}}\Delta X_{k,\infty}\right)^2 + \sum_k\left(\frac{\partial\dot{n}_{\mathrm{plume}}}{\partial X_{k,\mathrm{plume}}}\Delta X_{k,\mathrm{plume}}\right)^2\right] + \left(\frac{\partial EI_j}{\partial\dot{m}_{\mathrm{FG}}}\Delta\dot{m}_{\mathrm{FG}}\right)^2. \quad \text{(D.11)}$$

The error in BC emissions is defined as

$$(\Delta EI_{BC})^2 = \left(\frac{\partial EI_{BC}}{\partial f_{m,\text{measured}}}\Delta f_{m,\text{measured}}\right)^2 + \left(\frac{\partial EI_{BC}}{\partial T_{\text{cell}}}\Delta T_{\text{cell}}\right)^2 + \left(\frac{\partial EI_{BC}}{\partial P_{\text{plume}}}\Delta P_{\text{plume}}\right)^2 + \left(\frac{\partial EI_{BC}}{\partial \dot{n}_{\text{plume}}}\right)^2 \left[\left(\frac{\partial \dot{n}_{\text{plume}}}{\partial \dot{n}_{\text{FG}}}\frac{\Delta \dot{m}_{\text{FG}}}{M_{FG}}\right)^2 + \sum_k \left(\frac{\partial \dot{n}_{\text{plume}}}{\partial X_{k,\infty}}\Delta X_{k,\infty}\right)^2 + \sum_k \left(\frac{\partial \dot{n}_{\text{plume}}}{\partial X_{k,\text{plume}}}\Delta X_{k,\text{plume}}\right)^2\right], \quad \text{(D.12)}$$

where the soot mas fraction, $f_{m,\text{measured}}$, is defined in Eq. 2.1 and the error is defined as

$$\Delta f_{m,\text{measured}} = \frac{\partial f_{m,\text{measured}}}{\partial B_{\text{abs}}}\Delta B_{\text{abs}} = \frac{\Delta B_{\text{abs}}}{\text{MAC}}. \quad \text{(D.13)}$$

Appendix E Adiabatic Flame Temperature

The adiabatic flame temperature is the temperature of the products of a combustion reaction when no heat is lost to the surroundings and no work is extracted from the flow. It can be solved by applying an energy balance to a chemically reacting steady-flow system and assuming an isoenthalpic process (*i.e.*, $\Delta H = 0$), which is expressed as

$$\sum n_r\left(\bar{h}_f^\circ + \bar{h}(T) - \bar{h}^\circ\right)_r = \sum n_p\left(\bar{h}_f^\circ + \bar{h}(T_{\text{ad}}) - \bar{h}^\circ\right)_p, \tag{E.1}$$

where the terms on the left represent the enthalpy of the reactants and the terms on the right represent the enthalpy of the products. A schematic of the combustion system used in the present study is shown in Figure E.1.

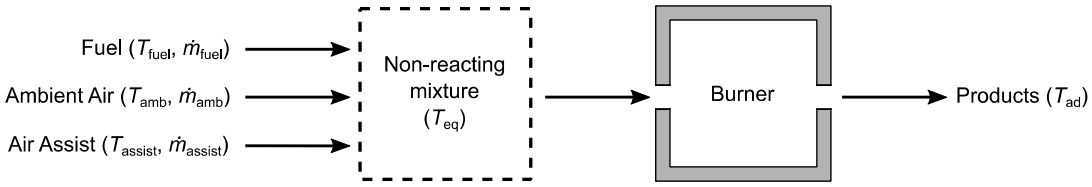

Figure E.1: Combustion system for analyzing adiabatic flame temperature.

The adiabatic flame temperature was calculated for each experimental set using an online STANJAN calculator. A required input was the initial equilibrium temperature of the non-reacting mixture based on

$$\sum_k \dot{m}_k \langle c_{p,k} \rangle T_k = \sum_k \dot{m}_k \langle c_{p,k} \rangle T_{eq}, \tag{E.2}$$

where $\dot{m}_k$ is the mass flow rate of each component of the mixture, namely, the fuel gas, assist stream and ambient air, $\langle c_{p,k} \rangle$ (J/kg·K) is the representative specific heat capacity for the temperature of interest, and T_k (K) is the initial temperature of the component. The equilibrium temperature, T_{eq}, can be isolated as

$$T_{eq} = \frac{\sum_k \dot{m}_k \langle c_{p,k} \rangle T_k}{\sum_k \dot{m}_k \langle c_{p,k} \rangle}. \quad \text{(E.3)}$$

The mass flow rate of each component of the mixture, namely, the fuel gas, assist stream and ambient air constituted stoichiometric combustion when CCE = 100%. For a CCE < 100%, proportionally less air participated in the reaction.